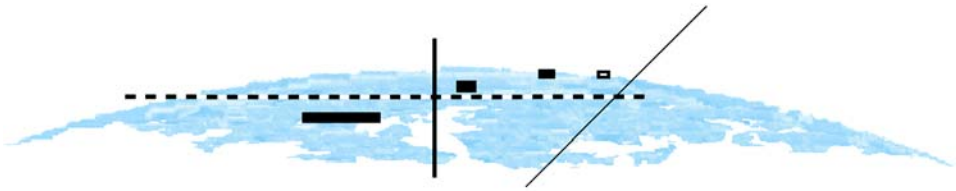

GeoForschungsZentrum Potsdam

STIFTUNG DES ÖFFENTLICHEN RECHTS

Scientific Technical Report

ISSN 1610-0956

Modelling the Earth's magnetic field of magnetospheric origin from CHAMP data

Von der Gemeinsamen Naturwissenschaftlichen Fakultät
der Technischen Universität Carolo-Wilhelmina
zu Braunschweig
zur Erlangung des Grades einer
Doktorin der Naturwissenschaften
(Dr. rer. nat.)
genehmigte
D i s s e r t a t i o n

von Judith Schwarte
aus Hiltrup (jetzt Münster)

1. Referent: Prof. Dr. Hermann Lühr
2. Referent: Prof. Dr. Karl-Heinz Glaßmeier
eingereicht am: 08.01.2004
mündliche Prüfung (Disputation) am: 03.03.2004

2004
(Druckjahr)

Veröffentlichungen von Teilen der Arbeit

Teilergebnisse aus dieser Arbeit wurden mit Genehmigung der Gemeinsamen Naturwissenschaftlichen Fakultät, vertreten durch den Mentor der Arbeit, in folgenden Beiträgen vorab veröffentlicht:

Publikationen

- Schwarte, J., Lühr, H. & Holme, R.: Secular Variation from CHAMP Magnetic Field Measurements, DFG project report, Potsdam (2001).
- Schwarte, J., Lühr, H. & Holme, R.: Improved parametrisation of external magnetic fields from CHAMP measurements, in: First CHAMP Mission Results for Gravity, Magnetic and Atmospheric Studies, Editors: Chr. Reigber, H. Lühr, P. Schwintzer, Springer Verlag Berlin (2003).
- Schwarte, J., Chambodut, A., Lühr, H. & Mandea, M.: Parametrisation of external magnetic fields from CHAMP vector data, Proceedings of the 4th Ørsted International Science Team Conference, Narayana Press, Danish Meteorological Institute Copenhagen (2003)

Tagungsbeiträge

- Schwarte, J., Lühr, H. & Holme, R.: Improved parametrisation of external magnetic fields from CHAMP measurements. (Poster) 1st CHAMP science meeting, Potsdam (2002).
- Schwarte, J., Lühr, H. & Holme, R.: Verbesserte Parametrisierung des externen magnetischen Feldes anhand von CHAMP Messungen. (Vortrag) 62. Jahrestagung der Deutschen Geophysikalischen Gesellschaft, Hannover (2002).
- Schwarte, J., Lühr, H. & Holme, R.: Improved parametrisation of external magnetic fields from CHAMP measurements. (Vortrag) Kolloquium des DFG Schwerpunktprogramms 1097, München (2002).
- Schwarte, J., Chambodut, A., Lühr, H. & Mandea, M.: Parametrisation of external magnetic fields from CHAMP vector data. (Vortrag) 4th Ørsted International Science Team Conference, Copenhagen (2002).

- Schwarte, J., Chambodut, A., Lühr, H. & Mandea, M.: Parametrisation of external magnetic fields from CHAMP data. (Institutsvortrag) Institute de Physique du Globe de Paris, Paris (2002).

- Schwarte, J., Chambodut, A., Lühr, H. & Mandea, M.: Parametrisierung des externen magnetischen Feldes anhand von CHAMP Vektordaten. (Vortrag) 63. Jahrestagung der Deutschen Geophysikalischen Gesellschaft, Jena (2003).

- Schwarte, J., Chambodut, A., Lühr, H. & Mandea, M.: Magnetic signature of magnetospheric sources in CHAMP data. (Vortrag) IUGG, Sapporo, Japan (2003).

- Schwarte, J., Chambodut, A., Lühr, H., Mandea, M. & Holme, R.: Modelling the Earth's magnetic field of magnetospheric origin from CHAMP vector data. (Poster) 2nd CHAMP Science Meeting, Potsdam (2003).

- Schwarte, J., Chambodut, A., Lühr, H., Mandea, M. & Holme, R.: Modelling the Earth's magnetic field of magnetospheric origin from CHAMP vector data. (Poster) Kolloquium des DFG Schwerpunktprogramms 1097, Potsdam (2003).

Contents

List of Figures

List of Tables

Chapter 1

Introduction

Ninety percent of the Earth's magnetic field are consistent with a magnetic field that would be generated from a dipolar magnetic source located at the centre of the Earth, aligned with the Earth's rotational axis. This first order description of the Earth's magnetic field was initially given by William Gilbert in 1600. Such a simple description is not sufficient for analysis of the Earth's magnetic field, since the remaining ten percent of the magnetic field cannot be explained well.

As observed on the Earth's surface, the magnetic field can be separated into three components:
The **Main Field** is the major component of the magnetic field and is believed to be caused by electrical currents in the Earth's fluid outer core. The temporal variation of this part of the magnetic field is known as secular variation.
The **Crustal Field** is the portion of the magnetic field associated with the magnetism of crustal rocks. This part of the field contains both, magnetism caused by induction and from remanent magnetisation.
The **External Magnetic Field** is a relatively small portion of the observed magnetic field. It is generated from magnetic sources external to the Earth. This field is believed to be mainly produced by currents in the Earth's ionosphere and magnetosphere and their interactions with the solar wind (charged, high energetic particles). Hence, temporal variations associated with the external magnetic field are coupled to solar activity.

If the Earth had neither a global magnetic field nor a magnetosphere, the solar wind would directly penetrate our atmosphere which would have severe consequences for

life on Earth. Instead, the solar wind interacts with the Earth's magnetosphere. This generates impacts which deform the Earth's magnetosphere. And the solar wind is diverted around our planet. The changes in the magnetosphere are more intense during magnetic storms, when explosive events on the Sun give the solar wind an unusually high velocity or density. Although the magnetosphere efficiently averts off the solar wind, an influence on the Earth is noted. Since the solar wind plasma comprises of electrically charged particles that are moving rapidly past the Earth's magnetic field, electric currents are generated, which flow along the Earth's magnetic field lines into the ionosphere. Especially above the polar regions, this causes aurora. Very large magnetic storms, as on October 29/30, 2003 and the associated aurora represent a clear signature of these kinds of field variations.

Spherical harmonic analysis (SHA) is commonly used to describe the magnetic field. In SHA it is possible to distinguish between internal and external contributions to the Earth's magnetic field. The spherical harmonic coefficients describe dipolar, quadrupolar and higher parts in spherical coordinates. Differences between two series of models are interpreted as secular variation. Such an approach requires highly reliable models. Care must be taken that spurious effects like instrumental drifts or unmodelled field contributions do not cause artificial changes. A still not very well known part of the Earth's magnetic field is the external field caused by electric currents in the ionosphere and magnetosphere. This work concentrates on the magnetospheric current systems, in order to correct the effect of large-scale magnetospheric current systems. Their exact knowledge is vital to improve the main field and secular variation models.

Until 1980 geomagnetic measurements were only undertaken using observatories. Since then, additional magnetic vector data are provided by satellites. The era of satellites was the beginning of an advanced understanding about the very complex magnetosphere. After series of satellite missions, as Magsat or Ørsted, CHAMP (CHAllenging Minisatellite Payload) was launched in 2000. It is the basis for improved main field modelling and a better determination of secular variation. On board the satellite are gravity, atmospheric, and magnetic field instruments which are of most interest for this study. Due to the inclination CHAMP is changing the orbit in local time. From time to time CHAMP is flying in resonance with the

Earth's rotation, i.e. the satellite is flying over the same ground track after a couple of days. To model changes during a period of a few days (in main field modelling usually 2-5 quiet days) these so called ***repeat tracks*** are very helpful for an improved main field/external field model. For example, in October 2000 they covered three days. This is also a commonly used period in main field models.

On the Earth's surface the magnetic effect of magnetospheric currents is characterised by several indices. One possibility, used in main field modelling, is the D_{ST}-index. In main field modelling, the external magnetic effect in the equatorial plane has been parametrised in terms of a linear dependence on the D_{ST}-index. For an improved main field model it is necessary to have a precise description of the effect of magnetospheric currents during the covered period at satellite altitude. One possibility is given by this study.

In a first order model, called **'model 1'**, scalar data from the Overhauser Magnetometer on board CHAMP are used. A model using solely the total field intensities needs several assumptions of the properties and the behaviour of the magnetosphere. It is assumed that the external field is produced by a symmetric ring current which is located in the equatorial plane of the geomagnetic dipole. A correction function for external currents is found which shows a local time dependence of the spherical harmonic coefficients.

For further improvements, the method using vector data from the Fluxgate Magnetometer on board CHAMP is introduced. The model from vector data, called **'model 2'**, can be yield through a direct inversion for each component of the magnetic field. Obtained are SHA coefficients which describe the effect of external currents at satellite altitude. As expected, the results are very similar to **'model 1'**. The resulting correction function shows a clear local time dependence.

Finally, it will be explained how a possible constitution of the external sources of the geomagnetic field can look like and how the effect of these magnetospheric currents can be corrected in main field modelling.

Chapter 2

The Earth's magnetic field

The geomagnetic field is enclosing the Earth completely. It is a very complex system which is a combination of fields of different origin and it changes in space and time. The sources are the Earth's interior and currents in the ionosphere and magnetosphere.
A first way to visualise the direction of the Earth's magnetic field was possible with the help of a magnetised needle. A very well known version is the compass. Since centuries the geomagnetic field has been used for navigation. But, the compass is showing us only the direction of this vector field, not its magnitude. Magnetic observations over the last 200 years and several satellite missions in the past decades have been very useful for a better understanding of the structure of the geomagnetic field [Stern, 2002], [Jonkers et al., 2003].

2.1 The internal field

2.1.1 The main field

The dominant part of the Earth's magnetic field originates in the Earth's core. The **core field** generates ninety percent of the magnetic field at the Earth's surface. Currently, its intensity at the Earth's surface ranges from about 30000 nT at the equator to 60000 nT at the poles. This field, often called **main field**, has its origin in the Earth outer core below the core mantle boundary at a depth of about 2900 km [Campbell, 1997]. In a first approximation it is a dipole field at the Earth's

surface.
It is not possible that the Earth is a permanent magnet, because the Curie temperature is already reached at a depth of about 20 km. One mechanism which can produce this dipolar field is a geodynamo [Merrill et al., 1998].

The Earth's magnetic field varies significantly in space and time. Spatial variations are the movement of the geomagnetic poles over the last centuries [Mandea & Dormy, 2003] and the increase or decrease of its intensity in some areas [Maus et al., 2002].

The time scales of temporal variations range from seconds to millions of years [Cain et al., 2003]. Usually, although it is not very distinct, variations with periods of a few tens of years or longer are of internal origin while variations with periods of less than a year are of external origin. The slower, internal change in the magnetic field over time scales of decades to centuries (Fig. 2.1) are referred to as secular variation [Bloxham & Gubbins, 1985]. The three historically measured components (H, Z, D) are shown. The report of the declination, D, already starts in the early nineteenth century. The nearly linear increase from about -19° to about 1.5° is continuously measured, first in Freiberg and thereafter in Potsdam, Seddin and Niemegk. Due to more disturbed surroundings the observatories were moved. It also can be seen, that the Z-component increased from about 43000 nT to about 45000 nT from 1890 to 2000. The third component is the horizontal component, H, which varies between 18400 nT and 18800 nT.

It also has been shown that a reversal of the Earth's magnetic field is possible. A record that the direction and intensity as it reverses can be obtained from a Miocene volcanic sequence. During a reversal the field is decreased to about 20% of its normal intensity at the surface and it is loosing its typical axisymmetry. The polarity of the magnetic field is not turning over for 180° at once. A reversal needs several thousands years during which its formation is more or less chaotic. During that time period, e.g., cosmic radiations might have been increased drastically and life on Earth might have been affected [Pervot, 1985].

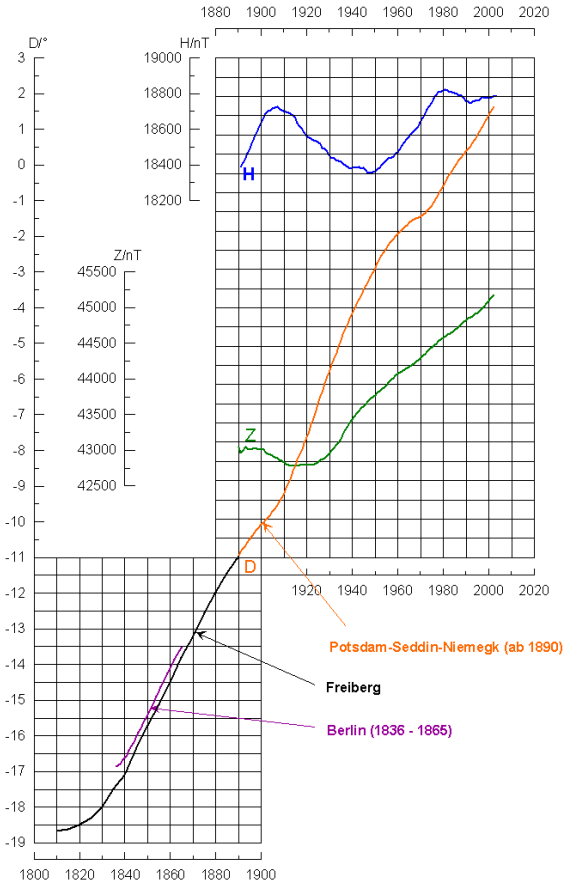

Figure 2.1: Secular variation (Z, D and H component) from 1800 to 2000 at the observatories Freiberg, Berlin and Potsdam-Seddin-Niemegk (from M. Korte, pers. corr.).

2.1.2 The lithospheric field

One other, small part of the internal magnetic field is the **crustal** or **lithospheric field**. Here, the lithosphere is meant to be the Earth's crust and its upper mantle. In ground magnetic measurements its magnitude varies from fractions of nT to several thousands of nT. Compared to the distance of external sources of several Earth radii ($1R_E = 6371.2$ km) the thickness of the crust (up to about 100 km) is very small. Because of these comparably small source dimensions the spatial gradients are larger. This part of the Earth's magnetic field is also called 'anomaly field'. The variations are associated with different geological properties of the crust. An example is shown in Fig. 2.2 (light colours indicate weak magnetisation). The contrast between a

weakly magnetised oceanic and a stronger magnetised continental crust and upper mantle can be seen. For a better description of these small-scale features, a good external field model is necessary.

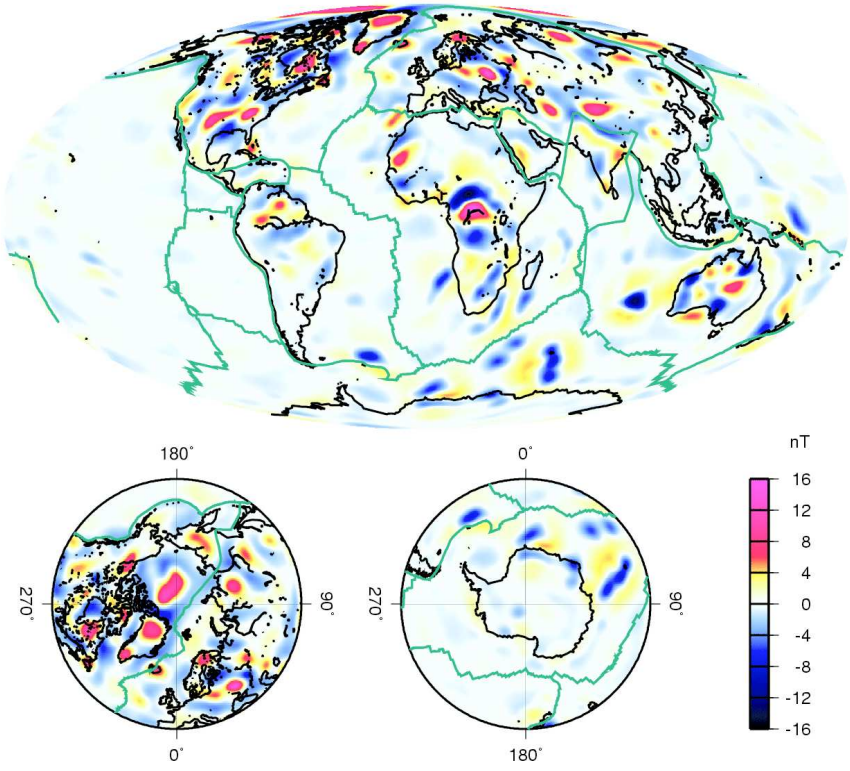

Figure 2.2: Predicted vertical field anomaly maps for spherical harmonic degrees 16-80 at an altitude of 400 km, from [Hemant, 2003]. The bootom panels show the polar view of the North pole (left panel) and the South pole (right panel).

2.2 The external field

2.2.1 The ionospheric field

The region between the neutral atmosphere and the magnetosphere is a partially ionised plasma, which expands from about 70 km altitude up to about 1500 km and is referred to as the ionosphere. It is divided into three layers, the D-, E- and

F-region. The plasma density ranges from 10^6 to 10^{13} m^{-3}.

The ionospheric current systems, e.g., the equatorial [Ivers et al., 2003] and polar electrojets [Akasofu et al., 1965], are quite difficult to describe. They change rapidly in time and space. For example, the magnetic effect of the equatorial electrojet, due to higher plasma density, is only prominent on the dayside. Other currents, which are not described in detail, are the field aligned, Region 1 and Region 2 currents (Fig. 2.3). They are the connection between the ionosphere and the magnetosphere. Figure 2.3 also shows the magnetospheric currents which will be explained in more detail in the following section.

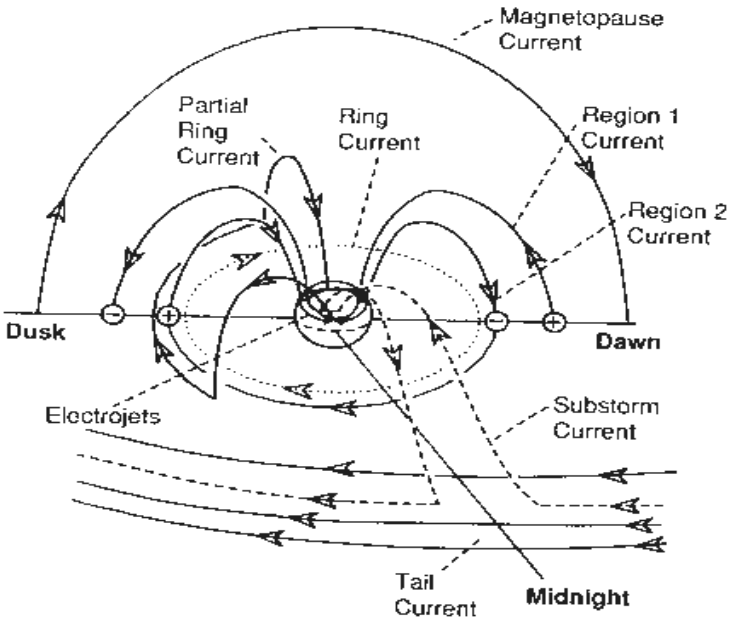

Figure 2.3: Currents in the Earth's ionosphere, and magnetosphere, from [Kivelson & Russell, 1995].

2.2.2 The magnetospheric field

In this study the most interesting part of the Earth's magnetic field has its origin in the magnetosphere. This external, magnetospheric field is caused by currents on the magnetopause on the sunward side, in the magnetotail (tail current) on the

anti-sunward side and by the (partial) ring current which is surrounding the Earth in the equatorial region at a distance of several Earth radii (Fig. 2.3). At the Earth's surface the measured effect has an amplitude of a few tens of nT during quiet times (e.g., Sept. 16-26, 2002, B.1) and up to a few hundreds of nT during disturbed periods (e.g., Sept. 4-11, 2002, B.1).
The magnetic effect caused by the ring current is usually parametrised by the D_{ST}-index. This index describes the variations of the equatorial ring current monitored by observatories close to the geomagnetic equator (Fig. 2.4 and Appendix B).

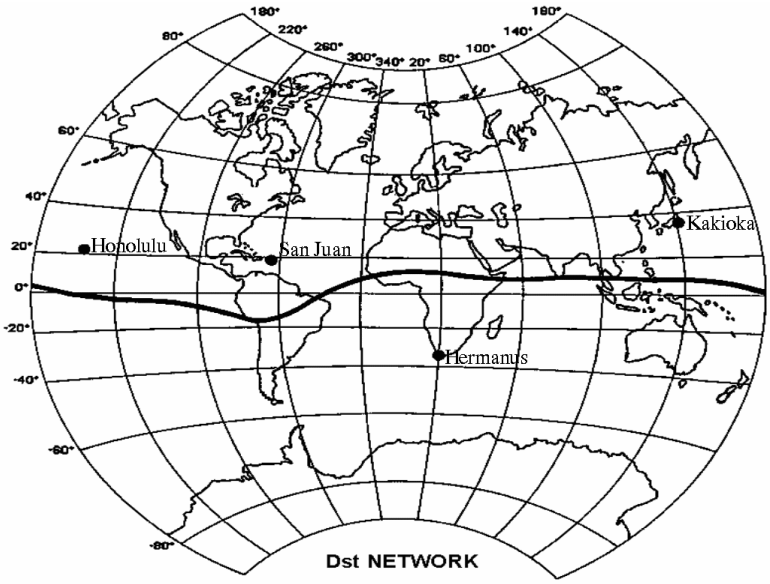

Figure 2.4: Network of D_{ST}-Observatories. The D_{ST} index is calculated from these four observatories around the geomagnetic equator (black line), from [WDC-Kyoto, 2003].

The network of these observatories computes the difference to their baseline and hourly mean values are provided as D_{ST}-index [WDC-Kyoto, 2003] by each of these four observatories. The intensity of the magnetic effect depends strongly on the solar activity. During a magnetic storm (high solar activity) the dayside magnetosphere is compressed. This affects the currents in the ionosphere and magnetosphere and can be noticed as an increase of the magnetic field. In addition, the ring current intensities during active periods cause a decrease of the Earth's magnetic field.
Around the Earth is a plasma environment whose dynamics are dominated by the

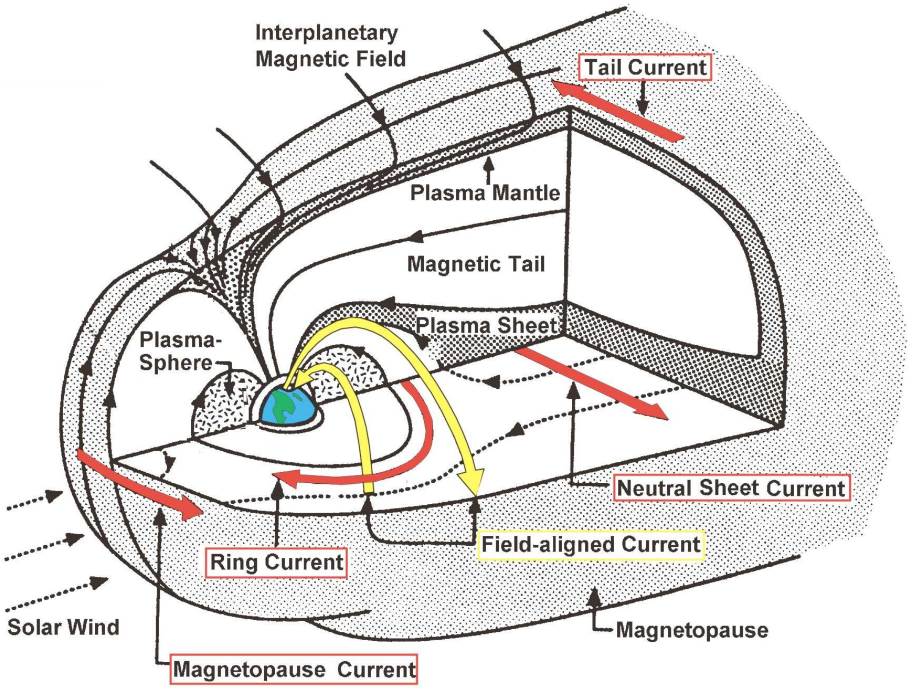

Figure 2.5: The Earth's magnetosphere: Currents in the magnetosphere whose magnetic effect will be modelled are coloured in red. The FACs (yellow) are the connection between the ionosphere and the magnetosphere. Their effect is quite difficult to model, from [Kivelson & Russell, 1995].

magnetic field of the Earth. Figure 2.5 illustrates the magnetosphere and its currents whose magnetic effect will be modelled. The shape of this volume is much influenced by the interplanetary magnetic field (IMF) and the solar wind (SW). The solar wind - outside - is a highly conductive plasma streaming away from the Sun with a typical velocity of about 400 km s^{-1}. The average electron and ion density is 5000 m^{-3} and the strength of its magnetic field is less than 10 nT.
The more charged particles are erupted by the sun and the higher their velocity the stronger is the pressure of the solar wind against the magnetopause (MP) and the closer it is pressed to the Earth on the sunward side.

On the anti-sunward side the solar wind flow stretches the magnetic field lines which

form a geomagnetic tail (about a few hundred R_E long). The magnetosphere (MS) solar wind interaction consists of several coupling mechanisms. Under 'optimal' conditions no SW-particles should enter the magnetosphere. But, especially at the poles the penetration with SW-particles is stronger.

2.3 Common main field models

Up to now there is no model of the effect of all external currents which are flowing in the magnetosphere. A common opinion about the magnetic field of external origin is, that it is produced by a ring current which is caused by trapped particles. These solar wind particles entered the magnetosphere and caused an electric current which flows westward around the Earth at a distance of 2 to 9 R_E [Daglis et al., 1999]. The particle drift of electrons is eastward and that of ions is westward. This results in a westward ring current. The theory about a stream of charged particles from the sun which enter the magnetosphere was first found by Chapman & Ferraro [1930]. This is still very close to the description today. The models of magnetospheric currents were improved more and more. During the 1960s the large-scale structure of the magnetosphere already contained the magnetopause current and the tail current as illustrated in Figure 2.5. The progress in understanding the magnetosphere occurred during several satellite missions. An overview of magnetospheric studies is given in [Stern, 1996]. In this thesis it is concentrated on the integral effect of all known magnetospheric currents.

In main field modelling today, the effect of magnetospheric currents is modelled by a linear dependence on D_{ST}. A list of several main field models is given here:

- Magsat model: The main field of the Earth is modelled up to degree 13 for internal contributions and up to degree 1 for external contributions. The external contributions are parameterised by the D_{ST}-index. The model is produced using Magsat data, done by Langel et al. [1996].

- OIFM model: The Ørsted initial field model of Olsen et al. [2000a] is a main field model of degree 19 for the internal field and of degree 2 for the external field. Again, the ring current is parameterised by the D_{ST} index.

- CM3: The '**C**omprehensive **M**odel Phase **3**' [Sabak et al., 2002] is a field model which first tried to coestimate all contributions to the Earth's magnetic field. The internal field is modelled up to degree 65 and the secular variation up to degree 13[1]. The ionospheric field is approximated by a sheet current at an altitude of 110 km. The major contributions of the magnetospheric field are caused by currents on the magnetopause, in the magnetotail and by the ring current. The effect of magnetospheric fields is parameterised by the D_{ST}-index as given by Langel & Estes [1985]. Another external field is caused by coupling currents between the ionosphere and the magnetosphere. The induction effect of the contributions of these external fields is modelled as well. In this model data from observatories, Magsat and POGO satellites from 1960-1985 are used.

- CO2 model: Model of the magnetic field of the Earth, especially to use with CHAMP data. This model of Holme et al. [2003] is obtained from CHAMP data, data from observatories and both Ørsted experiments. It contains the main field, linear secular variation and external contributions. The internal field is calculated up to degree 29, the secular variation of the main field up to degree 13 and the large-scale external field up to degree 2. The ring current is parameterised by the D_{ST} index.

- POMME: The '**PO**tsdam **M**agnetic **M**odel of the **E**arth' (POMME) [Maus et al., submitted 2003] is a main field model from the upper mantle up to an altitude of several kilometres above the Earth's surface. It includes contributions from a time varying core field, a ring current field which is modulated by D_{ST} and a time averaged magnetospheric field. The internal field and the secular variaton are modelled up to degree 15 and secular acceleration up to degree 10. The ring current is D_{ST} dependent with $q_1^0 = 0.76 \cdot D_{ST}$ and $g_1^0 = 0.32 \cdot q_1^0$. The input data are from the Ørsted and CHAMP satellites till September 2002.

[1] The secular variation is parameterised with 13 cubic B-splines, Eq. (5) and (6) in [Sabak et al., 2002]

2.4 Mathematical Description

2.4.1 Coordinate systems

Because there are so many coordinate systems, as combined in [Russell, 1971], the used coordinate systems and their corresponding transformations are described briefly. Figure 2.6 illustrates the different coordinate systems on board CHAMP. The components of the Earth's magnetic field are measured in an instrument-related coordinate system. The two coordinate systems of the Fluxgate Magnetometers are called FGM1 and FGM2. The magnetic vector data, available at the CHAMP data centre, are from the Fluxgate Magnetometer No. 1 (FGM1 in Fig. 2.6, further on it is called FGM).

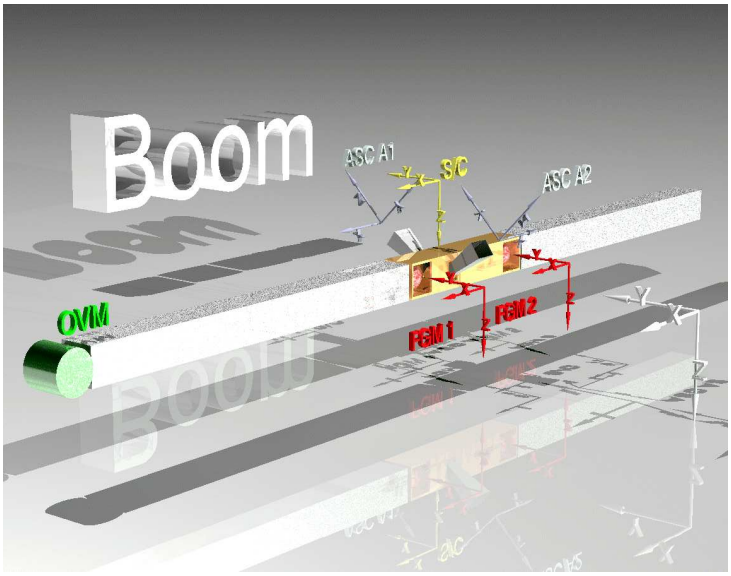

Figure 2.6: Coordinate systems on board CHAMP. The measurements of the Fluxgate Magnetometer are in an instrument related coordinates system which have to be transformed into an Earth fixed system (from M. Rother, pers. comm.).

In this system the X-component points into the flight direction of the satellite, the Z-component points down to the centre of the Earth and the Y-component completes the system. E.g., the Y-component points to the East if CHAMP is flying

exactly to the North, what means X is the North component. If this is not the case the components have to be transformed into the **N**orth-**E**ast-**C**entre (NEC) system. Therefore, the precise attitude is necessary which is obtained from the Advanced Stellar Compass (ASC). At the CHAMP data centre the magnetic field data are available in both coordinate systems, the instrument-related FGM and the Earth-fixed NEC system.

The transformation between these two systems is rather sophisticated taking into account the attitude, the orbit and the Earth's rotation. In this work only NEC data are downloaded from the data centre. Only for the correction around the poles (Sec. 5.2.2) the coordinates are going to be transformed back into the spacecraft system (SC = FGM).

Other difficulties occur because of the different Earth fixed coordinate systems. At observatories the geodetic coordinate system is used. That means, the Earth is not approximated by a sphere but by a reference ellipsoid [EUROCONTROL, 1997].

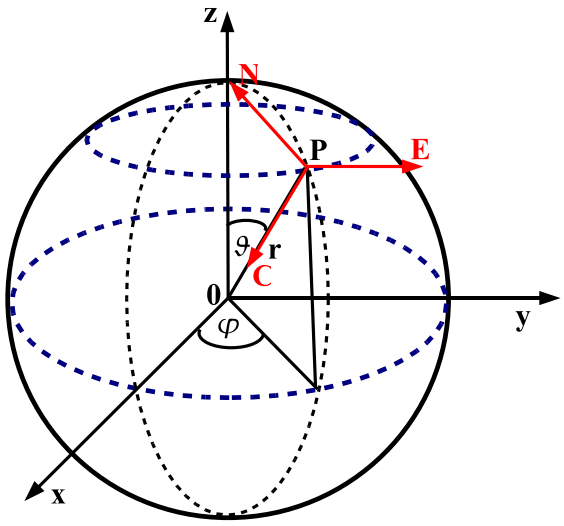

Figure 2.7: Earth-fixed coordinate systems: Illustrated are the Cartesian NEC system and spherical coordintes, after [Bronstein & Semendjajew, 1989].

Using CHAMP satellite data the coordinates are in the geocentric NEC system. In Figure 2.7 the Cartesian, geocentric coordinates, x, y and z, are visualised in

comparison to spherical coordinates depending on r, θ and ϕ. The NEC system is illustrated by red arrows. It contains the Northward component, N, which points to the North pole, along $\mathbf{e}_\theta$, the Eastward component, E, which is aligned with $\mathbf{e}_\phi$ and the centre component, C, which points down to the centre, along $\mathbf{e_r}$.

Commonly, most measurements are not done in a spherical coordinate system but in a local topocentric system (Fig. 2.8). There are several components that can be monitored. Historically, declination, D, inclination, I and the horizontal component, H, are measured.

Actually, at observatories, other components, X, Y and Z, and the total field intensity B or F are measured. At the location of the measurement the X component is pointing to the North, the Y component to the East and the Z component vertically down.

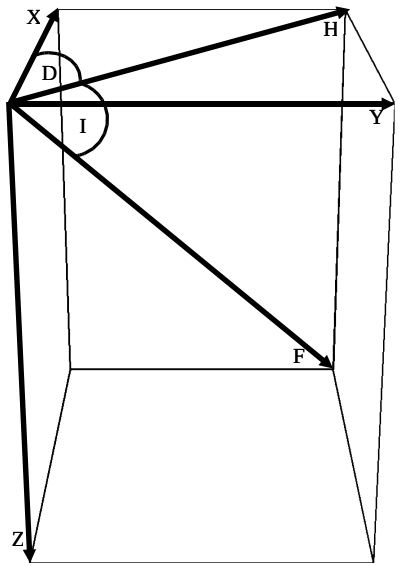

X = geographic North
Y = East
Z = vertically down
H = geomagnetic North
F = total field intensity, F = $|\mathbf{B}|$
I = inclination, I = $arctan(\frac{Z}{H})$
D = declination, D = $arctan(\frac{Y}{X})$

Figure 2.8: Orientation of typical components of the Earth's magnetic field measured at observatories, after [Jacobs, 1987].

As already explained, using satellite data the meaning of X, Y and Z is slightly different. The coordinate system is now in geocentric coordinates, i.e. the Earth is replaced by a reference sphere and Z is pointing to the centre of the Earth. Then, the three components X=N, Y=E and Z=C in the Cartesian, geocentric system are

connected to the spherical field components as follows:

$$X = -B_\theta, Y = B_\phi \quad \text{and} \quad Z = -B_r. \tag{2.1}$$

2.4.2 Spherical harmonic analysis

One description of the magnetic field can be obtained by using spherical harmonic functions. Spherical harmonic analysis (SHA) is nowadays a common method to describe the behaviour of physical phenomena in spherical coordinates. This technique was introduced - in geophysical questions - by C. F. Gauss in 1839 [Gauss, 1839]. Using this method the magnetic field is separated into fields of internal and external origin (see Eq. 2.7 and following).

If measurements are made at the Earth's surface, the core and crustal fields are of internal origin, and the fields caused by ionospheric and magnetospheric currents count as external fields. In case of satellites the effect of ionospheric currents is added to the fields of internal origin. The satellite altitude, especially of CHAMP, defines the separation border between internal and external sources and the origin of ionospheric currents is below the altitude of the satellite.

A starting point for describing the field components by spherical harmonic functions are Maxwell's equations [Jacobs, 1987]:

$$\nabla \times \mathbf{B} = \mu_0 J \tag{2.2}$$

$$\nabla \cdot \mathbf{B} = 0 \tag{2.3}$$

with the permeability of free space, μ_0 and current density, J. Assuming the geomagnetic field to be curl-free (J is negligible between the Earth surface and ionosphere) the field $\mathbf{B}$ can be represented as the gradient of a scalar potential V

$$\mathbf{B} = -\nabla V. \tag{2.4}$$

The potential V then must satisfy Laplace's equation

$$\nabla^2 V = 0. \tag{2.5}$$

In spherical coordinates (θ =colatitude, ϕ =longitude, r = radius) Equation 2.5 thus is transformed to

$$\frac{1}{r}\frac{\partial^2(rV)}{\partial r^2} + \frac{1}{r^2\sin\theta}\frac{\partial}{\partial\theta}\left(\sin\theta\frac{\partial V}{\partial\theta}\right) + \frac{1}{r^2\sin^2\theta}\frac{\partial^2 V}{\partial\phi^2} = 0. \tag{2.6}$$

A solution for V is found by separation of variables. Its general form is:

$$\begin{aligned} V &= a\sum_{n=1}^{\infty}\sum_{m=0}^{n}\left\{[g_n^m\cos(m\phi) + h_n^m\sin(m\phi)]\left(\frac{a}{r}\right)^{n+1}\right. \\ &\qquad \left. + [q_n^m\cos(m\phi) + s_n^m\sin(m\phi)]\left(\frac{r}{a}\right)^{n}\right\} P_n^m(cos\theta) \end{aligned} \tag{2.7}$$

where $a = 6371.2$ km is the radius of the reference sphere[2] (Earth's surface) and r, θ and ϕ are the radius, colatitude and longitude of the measurement point. $P_n^m(\cos\theta)$ are the associated Schmidt quasi-normalised Legendre Functions. The factors g_n^m, h_n^m, q_n^m and s_n^m are called Gauss coefficients of degree n and order m. They represent fields from internal sources (g_n^m, h_n^m) and external sources (q_n^m, s_n^m). For $m = 0$ they are called zonal harmonics and for $m = n$ sectorial harmonics. Since no magnetic monopoles exist, g_0^0 is always zero. Coefficients of internal degree 1 describe geocentric dipoles which are oriented along the z-axis ($m = 0$) or along the x-axis (g_1^1) and y-axis (h_1^1). Higher degree coefficients then represent geocentric quadrupoles ($n = 2$), octupoles ($n = 3$) and so on. Thus, the g_1^0 term is meant to describe an internal dipole situated in the Earth's centre and oriented in the direction of the rotation axis of the Earth.

[2] As this value is used in data preprocessing and most geomagnetic studies not the WGS84 (World Geodetic System 1984) committed value of 6371.0 km is chosen.

The components of the magnetic field can be computed from Equation 2.7 (using Eq. 2.4). Calculating the gradient of this potential gives the three components in spherical coordinates as follows [Jacobs, 1987].

$$B_r = \frac{-\partial V}{\partial r} = \sum_{n=1}^{\infty}\sum_{m=0}^{n}\left\{(n+1)[g_n^m\cos m\phi + h_n^m \sin m\phi]\left(\frac{a}{r}\right)^{n+2} - n[q_n^m\cos m\phi + s_n^m \sin m\phi]\left(\frac{r}{a}\right)^{n-1}\right\} P_n^m(\cos\theta), \quad (2.8)$$

$$B_\theta = \frac{-\partial V}{r\partial\theta} = -\sum_{n=1}^{\infty}\sum_{m=0}^{n}\left\{[g_n^m\cos m\phi + h_n^m \sin m\phi]\left(\frac{a}{r}\right)^{n+2} + [q_n^m\cos m\phi + s_n^m \sin m\phi]\left(\frac{r}{a}\right)^{n-1}\right\}\frac{dP_n^m(\cos\theta)}{d\theta}, \quad (2.9)$$

$$B_\phi = \frac{-1}{r\sin\theta}\frac{-\partial V}{\partial\phi} = \frac{1}{\sin\theta}\sum_{n=1}^{\infty}\sum_{m=0}^{n} m\left\{[g_n^m\sin m\phi - h_n^m\cos m\phi]\left(\frac{a}{r}\right)^{n+2} + [q_n^m\sin m\phi - s_n^m\cos m\phi]\left(\frac{r}{a}\right)^{n-1}\right\} P_n^m(\cos\theta). \quad (2.10)$$

In principal the radial intensity, i.e. B_r, and one horizontal intensity, e.g., B_θ, has to be known to separate internal from external fields. To simplify these equations, different assumptions are made for scalar and vector data. These will be explained in Sections 4.2 and 5.1.

2.4.3 Other magnetic field descriptions

Some other modelling methods exist, such as harmonic spline modelling [Shure et al., 1982] or wavelet techniques [Holschneider et al., 2003], [Mayer & Maier, 2003]. Using splines to model the Earth's magnetic field the model is smoothed according to objective criteria which are nevertheless consistent with the data. These criteria can be chosen to minimise the complexity of well-defined parameters of the field, like the energy outside the core or the mean square radial field component at the core-mantle boundary. Short-wavelength fields originating in both, core and crust, are suppressed [Shure et al., 1982], [Parker & Shure, 1982].

Recently, a new representation of the magnetic field on the sphere has been sought, the chosen approach making a direct relation between the spherical harmonics and wavelets. Holschneider et al. [2003] present the theoretical description of the wavelets on the sphere in order to use them in field modelling. The first comparisons between the spherical harmonic basis and wavelet basis show how well the wavelets are able to reproduce the spherical harmonics, and the potential of wavelets has been shown.

Any kind of geomagnetic field modelling can be described when optimising the cost function "*error + smoothness*". In general, the smoothness part can be associated with some (physically motivated) norms. It is in general implemented through an *a priori* damping of the basis functions in the inversion. The function that gives the optimal solution is sometimes referred to as a spline solution. As it stands, it does not appeal to any family of basis functions in which the actual numerical computations are carried out. Therefore in the limit of infinitely many functions and without any numerical errors, it is possible to get the same models, if spherical harmonics, wavelets, or any other complete family of functions are used. However, given finite resources it does matter, since for a fixed number of basis functions, wavelets have sometimes better approximation properties than spherical harmonics. Moreover, wavelets may play an additional role in modelling of strongly heterogeneous fields, such as from external currents [Mandea, 2003].

Chapter 3

CHAMP

The age of geomagnetic vector measurements from space started in 1979 with Magsat (Fig. 3.1 (left panel), [MAGSAT, 2003]). This American satellite of the National Aeronautics and Space Administration (NASA) and the United States Geological Survey (USGS), had a lifetime of 6 months and an orbit fixed in local time (dawn/dusk (6:00/18:00 LT) orbit). Magsat collected scalar and vector magnetic data in a low, near-polar orbit at an altitude of 350 to 570 km and an inclination of 96.8°.
Twenty years later, in 1999, Ørsted (Fig. 3.1 (centre), [Ørsted, 2003]) was launched. In 2003 this Danish satellite is still measuring the total field and the three vector components (X, Y, Z) of the geomagnetic field. Its orbit is elliptical at altitudes of 650 - 860 km. Because of the inclination of 96.5°, the orbit plane drifts through all local times in about 470 days.

One year later, in 2000, two further missions were launched. SAC-C, the Argentinien satellite, is flying in a sun-synchronous circular orbit with an inclination of 98.2° and an altitude of about 700 km (Fig. 3.1 (right panel), [SAC-C, 2003]). The magnetic experiments are often called 'Ørsted 2' because of the same set of instruments as the one on the Ørsted satellite. The third satellite for magnetic field measurements is CHAMP. It will be described in the following section in more detail. Because of the special orbit constellation (sometimes CHAMP is flying over the same ground track after a couple of days) in this study mainly CHAMP data are used.

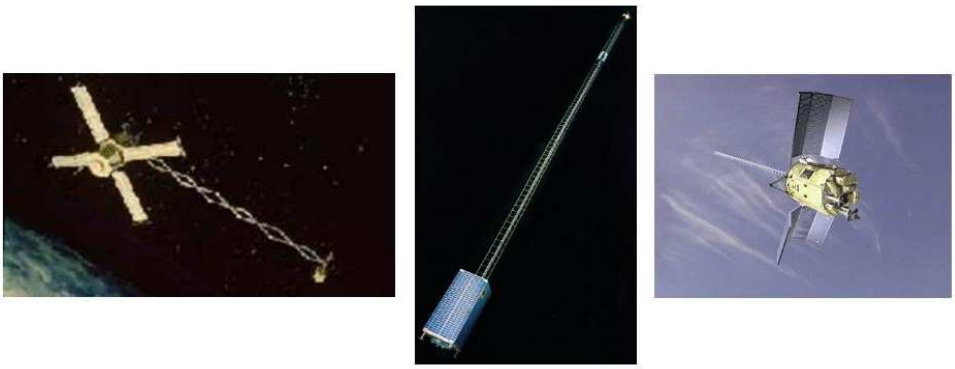

Figure 3.1: Images of magnetic satellites, on the left: MAGSAT [MAGSAT, 2003], in the middle: Ørsted [Ørsted, 2003] and on the right: SAC-C [SAC-C, 2003].

3.1 Satellite

CHAMP (**CHA**llenging **M**inisatellite **P**ayload, Fig. 3.2) is a georesearch satellite of the GeoForschungsZentrum (GFZ) Potsdam, Germany and the German Space Agency (DLR). The motivation was the better understanding of geoscience, the gravity and the magnetic field, and atmospheric questions.

On July 15, 2000 at 11:59:59.628 Universal Time Coordinated (UTC) the mini satellite CHAMP was launched from the Russian cosmodrome Plesetsk aboard a Russian COSMOS launch vehicle.
The satellite consists of two parts, the boom and the body. When CHAMP was launched the boom was stowed on top of the body. After the satellite was set into its orbit at an initial height of 454 km the boom was unfolded.
The complete length is 8333 mm including the boom with a length of 4044 mm. It is a quite large satellite because of the width of about 1600 mm, the height of 750 mm and a total mass of 522.5 kg. The dimension of the boom is 224 mm by 224 mm and its mass is 20 kg.

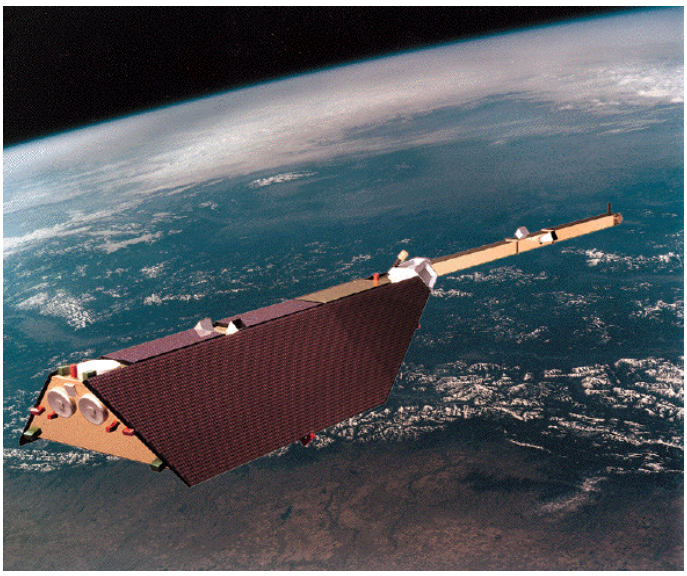

Figure 3.2: Image of the magnetic satellite CHAMP, from CHAMP webpage [CHAMP, 2003].

3.2 Magnetic instruments

Several instruments for gravity, magnetic field and atmospheric measurements are on board CHAMP. The instruments for magnetic measurements (explained in more detail later on in this section) are on the boom to reduce magnetic disturbances from the spacecraft (see Fig. 3.3). Thus, the magnetic instruments are at a certain distance from the satellite body and all its currents and residual magnetic fields. The boom is mounted at the front end of the satellite. One Overhauser Magnetometer (OVM) is carried at the tip of the boom, in the middle segment on an optical bench, two Star Sensors (ASC) and two Fluxgate Magnetometers (FGM) are placed. The OVM is used to calibrate the two vector magnetometers. In this work scalar data were also used for an initial study of the magnetic field caused by external current systems.

Because there are only web-publications (on the CHAMP webpage [CHAMP, 2003] or on the webpages of the relevant institutions, Appendix C) about the instrumentation on board CHAMP, the magnetic instruments are described briefly:

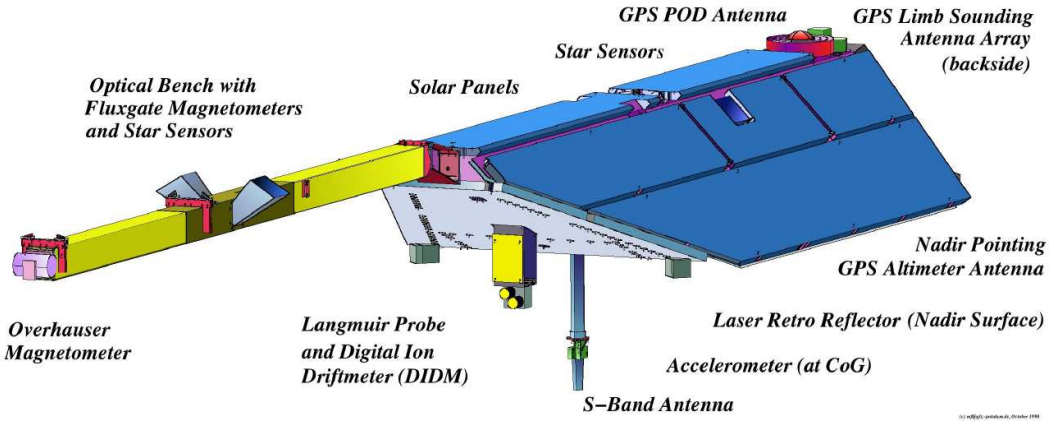

Figure 3.3: Instruments on board CHAMP, from CHAMP webpage.

- Global positioning system

  The GPS receiver is, in combination with the STAR accelerometer, the main instrument for obtaining the exact position of the satellite. From these two instruments the orbit can be determined with very high precision. The GPS was provided by National Aeronautics and Space Administration (NASA) and built at their Jet Propulsion Laboratories (JPL). Another important task of the GPS receiver is the precise timing possibility due to a synchronisation pulse. It is also used for atmospheric studies, e.g., atmospheric sounding.

- Electrostatic STAR Accelerometer

  The ACC was provided by the Centre National d'Etudes Spatiales (CNES) and was manufactured by the Office National d'Etudes et de Recherches Aerospatials (ONERA), France. It uses the basic principle of an electrostatic micro-accelerometer. The electrostatic forces are measured which effect the freely floating test body in a cage. The detected acceleration is proportional to the forces which are needed to keep the proof-mass in the centre of the cage.

- Advanced Stellar Compass

  The ASC was developed and fabricated by the Technical University of Denmark (DTU), Lyngby. On board CHAMP are two pairs of these star sensors. One is fixed to the accelerometer which is mounted exactly in the centre of mass of the satellite on the body. The other one is situated on the optical bench close to the FGM. That makes precise measurements of the attitude of

CHAMP possible which is necessary to use the magnetic vector readings.

- Fluxgate Magnetometer
  The FGM was developed and manufactured by the Technical University of Denmark (DTU). The design is based on a spherical coil sensor, which was newly developed for the Ørsted mission. It measures the three vector components of the magnetic field (full range of ± 65000 nT). The measurements are taken with a 50 Hz (nominal) sample rate. The deviation from linearity is ± 100 pT and the overall noise level is less than 100 pT (rms). The magnetometer is installed close to the star sensors on the optical bench because the knowledge of exact sensor attitude and time of measurement is necessary for the interpretation of vector data. The three measured components are relative to a satellite related coordinate system and have to be rotated into an Earth fixed coordinate system. A second FGM sensor is installed 600 mm away from the primary sensor for redundancy reasons.

- Overhauser Magnetometer
  The OVM was developed and manufactured by the Laboratoire d'Electronique de Technologie d'Information (LETI), France. This scalar magnetometer provides an absolute measurement of the field magnitude. The total field intensity ranges from 18000 to 65000 nT, which is needed for the in-flight calibration of the FGMs. The measurements are taken at a sample rate of 1 Hz and an absolute accuracy better than 0.5 nT. Its working principle is based on proton precession magnetic resonance.

- Digital Ion Drift Meter
  The DIDM was donated by the US Air Force Research Laboratory (AFRL), Hanscom. Its purpose is the measurement of the ion distribution and its moments in the ionosphere. From these measurements the ion density and temperature, the drift velocity and the electric field can be determined. This additional instrument can be useful to estimate ionospheric current systems. For interpretation a Planar Langmuir Probe (PLP) is necessary which is operating in combination with the DIDM.

3.3 Orbit

After the launch CHAMP was placed into a nearly circular orbit. The near polar orbit has an inclination of 87.3°. At the beginning of the mission CHAMP had an orbit height of 454 km which is decreasing to 300 km during five years (Fig. 3.4).

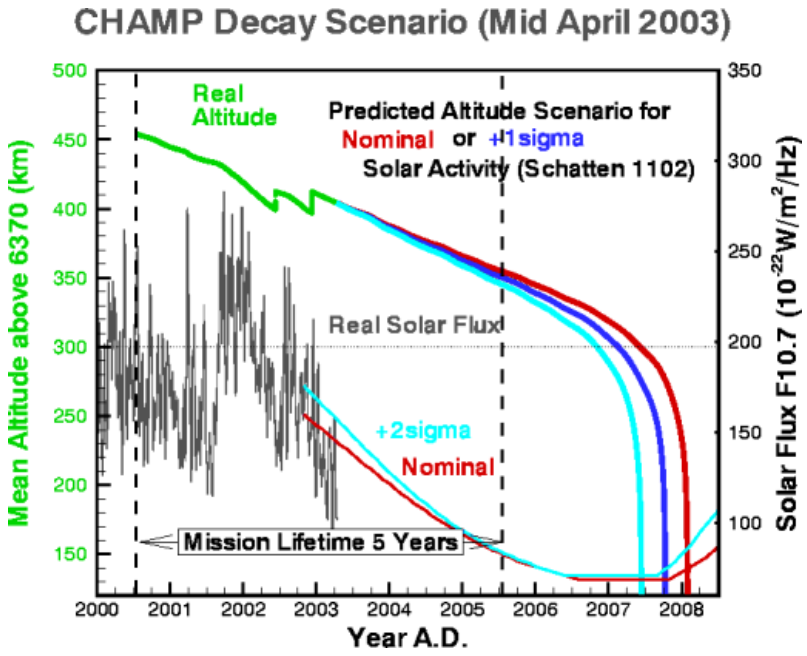

Figure 3.4: Prediction of satellite altitude above the Earth's surface (from H. Lühr, pers. comm.).

Fig. 3.4 shows the actual altitude of the last 3 years and the prediction until the end of the mission (July 2007).

The satellite lifetime depends on several conditions. In terms of size and geometry the satellite is constructed to survive these five years. But especially the solar activity may change the lifetime. A nominal solar activity is assumed and a higher or lower activity changes the end point which is set at an altitude of 300 km. If the solar activity is higher the end point is reached earlier. At the end-altitude of 300 km the friction is too big for a longer lifetime and the satellite will come down to the Earth quite fast.

Due to two orbit manoeuvres in June and December 2002 the satellite was lifted by about 20 km to reach the scheduled lifetime with some margin.

Because of the high inclination (87.3°) the orbit plane moves through all local times (LT) in only four months. The resulting homogeneous and complete global coverage over the Earth is very advantageous for good magnetic field models. This provides a very dense set of data. Figure 3.5 illustrates the global coverage of June, 19, 2002 (black lines) and the repeat tracks two days later (red lines).

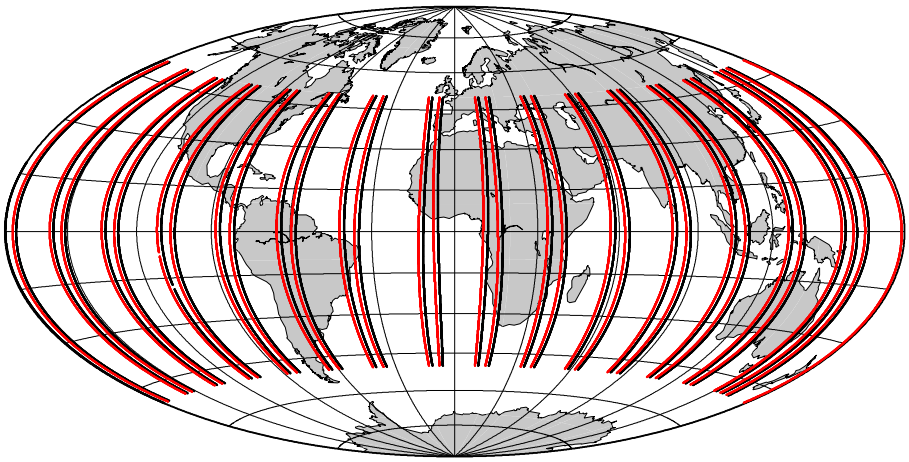

Figure 3.5: 'Two-day' repeat tracks over ±50° geographic latitude of day 900/902. The difference between ground tracks is about 1.7°. Black lines show ground tracks of day 900, red lines illustrate the repeat track on day 902.

3.4 Data

Figure 3.7 (top) shows an example of one day of data measured by the CHAMP vector magnetometer. The three vector components, X,Y, and Z of the Earth magnetic field are in the NEC system, i.e. X=N, Y=E and Z=C (Sec. 2.4.1).

At the Earth's surface the strength of the total field varies between approximately 30000 nT at the equator and about 60000 nT at the poles. At the geomagnetic poles the total field is dominated by the Z-component (downward component). The strongest contribution at the equator is the X-component (Northward component) while the Y-component (Eastward component) is quite small, but most affected by

disturbances from, e. g., field-aligned currents (FAC).

For an application in main field modelling usually a restriction to quiet times has to be done. Typical selection criteria are the indices D_{ST} and K_P[1] or the selection is done on local times [Chambodut et al., 2003]. The CO2 main field model [Holme et al., 2003], for example, selects data for $K_p \leq 1+$ for the time of observation and $K_p \leq 2o$ for the previous three hours and $|D_{ST}| \leq 10$nT and $|d(D_{ST})/dt| \leq 3$nT. In this study no data selections on D_{ST}, K_P or local time criteria are done. All data are used which gives a good global coverage. Because of an enormous effect of field-aligned currents in the polar region, for calculations using scalar measurements, only data between $\pm 50°$ geomagnetic latitude are included (Chapter 4). When modelling whole orbits using vector data first a 'pole correction' has to be applied (Chapter 5).

For the investigation in this study differences of residuals of two repeat tracks are used. What are repeat tracks and how to get these differences?

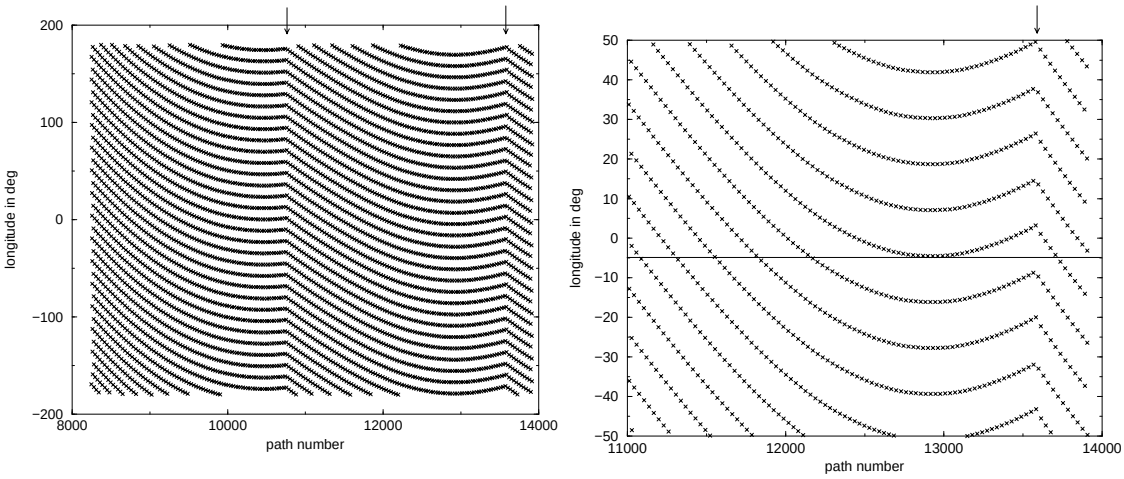

Figure 3.6: Longitude of equator crossings of CHAMP for the year 2002 (left panel) and for July to December 2002 (right panel). Discontinuities indicated by arrows are related to 2 orbit manoeuvres during 2002. Around path number 13000 the accuracy of the ***repeat tracks*** is best (indicated by the horizontal line).

[1] The global K_p index is obtained as the mean value of the disturbance levels in the two horizontal field components, observed at 13 selected, subauroral stations [Jacobs, 1989].

Figure 3.6 shows the longitude of each ascending equator crossing of CHAMP in 2002. A clear 2-days pattern with 31 distinct equator crossings emerges. The minima of the parabolic shaped curves (emphasised by the horizontal line) give the best periods for ***repeat tracks***. In an optimal case the difference in longitude is less than 0.1°.

Usually the periods, when repeat tracks are available, last about two months. Because of two orbit manoeuvres in 2002 (two discontinuities - indicated by arrows - seen in Fig. 3.6) the repeat cycle of two days lasts nearly the whole year.
Around path number 13000 (November 2002) the difference in longitude between such two repeat tracks was only 0.1°. While the agreement in colatitude is much more important a difference in longitude of 2.0° is still reasonable. For this work repeat measurements with differences in colatitude less than 0.2° and less than 2.0° in longitude are chosen.

The first step is the computation of the residuals between the measured data and the CO2 main field model [Holme et al., 2003] (Sec. 2.3). For this purpose the correction for external currents (up to degree 2) is excluded in the CO2 model. In principle the removal of the main field from the measurements is not necessary for our purpose, but this would require an extremely precise repeat track which is in practise not achieved.

In case of scalar data the residuals of the total field, and in case of vector data the residuals of each component with respect to the CO2 model are calculated. An example for residuals calculated from vector data is shown in the bottom panel of Fig. 3.7.

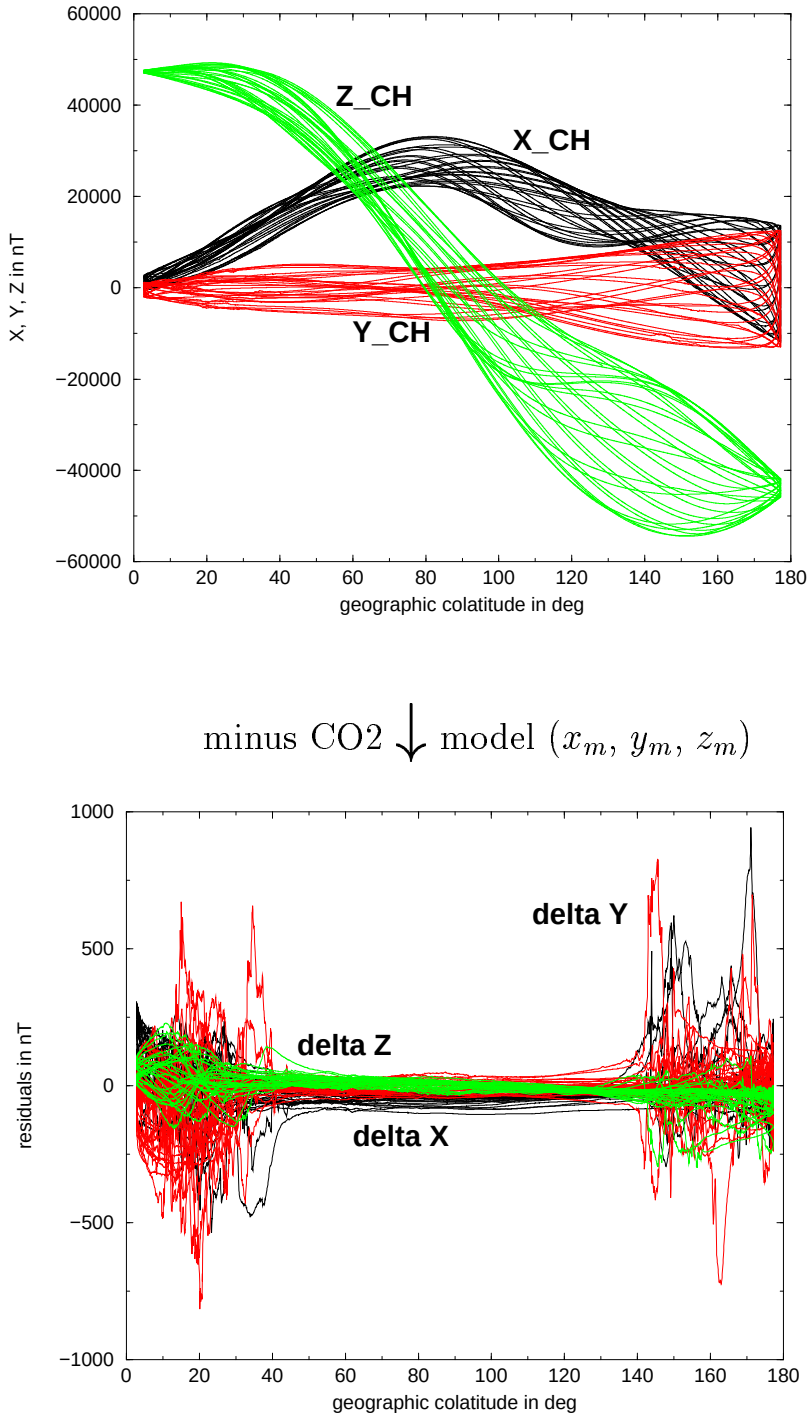

Figure 3.7: Example of the measured North component, x_{CH}, the East component, y_{CH} and component down to the centre, z_{CH}, for day 945 in August 2002 (top panel). The bottom panel shows the residuals of each component and the CO2 model (δx (black line), δy (red line) and δz (green line)).

From these residuals the differences between two repeat tracks (the residual for the first measured point and the one of the repeat track, e. g., two days later in 2002) are calculated and used in the model. The resulting model is describing the changes which occur during the corresponding repeat intervals.

This means for vector data: x_{CH}, y_{CH} and z_{CH} are the measured components in the Earth-fixed coordinate system and x_m, y_m and z_m are the corresponding components obtained from the CO2 main field model. From these two sets of magnetic field components the residuals are calculated for the first day ($\delta x_i = x_{CH,i} - x_{m,i}$, $\delta y_i = y_{CH,i} - y_{m,i}$ and $\delta z_i = z_{CH,i} - z_{m,i}$) and the second day - in 2002 two days later - ($\delta x_{i+2} = x_{CH,i+2} - x_{m,i+2}$, $\delta y_{i+2} = y_{CH,i+2} - y_{m,i+2}$ and $\delta z_{i+2} = z_{CH,i+2} - z_{m,i+2}$) are computed. Thereafter, the difference between two repeat tracks ($rcx = \delta x_i - \delta x_{i+2}$, $rcy = \delta y_i - \delta y_{i+2}$ and $rcz = \delta z_i - \delta z_{i+2}$) are used as model input.

Chapter 4

Modelling external currents from scalar data

In principle vector data are always best for any kind of magnetic field modelling. To obtain good quality vector data the precise position and attitude of the satellite has to be known. Because of all these difficulties a first study based on scalar data is done. Scalar data are obtained in a straight forward manner and less complicate, e. g., it is less likely that observed features are due to instrument artifacts. For a first model scalar data alone are used over tracks from 40° to 140° geographic colatitude. This method is called **'model 1'**.

4.1 'Model 1'

One justification for using only the total field intensity is the fact that - because of the large distance - large-scale magnetospheric currents generate a fairly homogeneous field in the near-Earth space which is approximately aligned with the geomagnetic dipole. At low latitudes the external fields are almost parallel to the main field at the Earth's surface. Figure 4.1 shows the resulting magnetic field of a symmetric ring current in the equatorial plane. Assuming a simple dipole field close to the Earth, the effect of this ring current is thus only little attenuated in the total field at low latitudes.

The first step in data processing is to remove the main field. The CO2 main field model [Holme et al., 2003], including secular variation, is used to estimate the

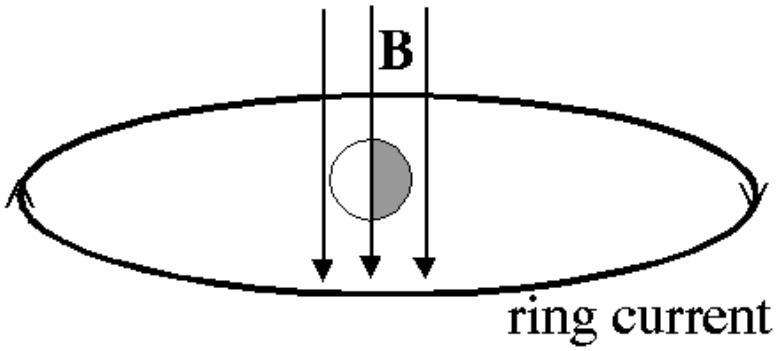

Figure 4.1: A ring current around the Earth in a distance of several Earth radii produces a homogeneous field at the surface. In SHA this resulting field is described by the q_1^0 term.

appropriate main field for a given location and epoch. The residuals contain contributions from lithospheric magnetisation, external current systems and deficiencies of the field model.

During the first months of the CHAMP mission the repeat cycle was three days. Two data sets in October and December 2000 are analysed. By computing the difference of the residuals between such two successive repeat tracks all constant parts (with respect to a three day period) are cancelled while the variable contributions are emphasised. They are generated by external currents and they are an indication of the shape and amplitude of external signals.
For the first example, measurements of the scalar magnetic field are chosen along an orbital arc, the $-10°$-meridian, over a latitude range of $\pm 50°$. The readings have been taken on 24 and 27 October 2000, when CHAMP was flying in a dawn-dusk orbit, i.e. on 24 October 2000 the satellite was crossing the equator at 0517 local time, respectively 1817 LT. First the residuals between measured field and the CO2 model field are calculated for the first and second day (Fig. 4.2). The third curve in Figure 4.2 represents the difference between these two residuals.
Undulations present on both curves are indications of lithospheric magnetic signatures. Ionospheric currents are expected to be negligible at this local time. When

calculating the difference between the two sets of readings the small-scale wiggles disappear and a smoother large-scale variation results which is attributed to the ring current effect.

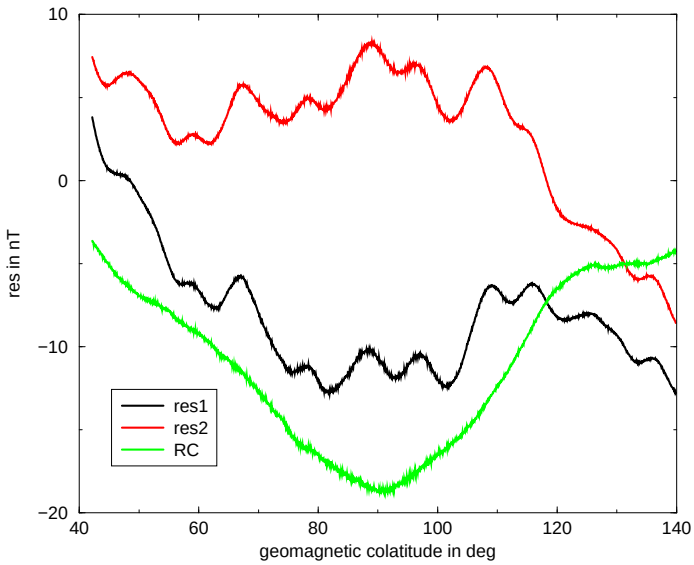

Figure 4.2: Repeat track on 24 and 27 Oct. 2000, dawn side at 0517 LT: Calculated residuals of the first (black) and second (red) day and the difference of these residuals ($b_{first} - b_{second}$, green) are shown. The corresponding D_{ST} values are: -28 nT for the hour of the track on the first day and -17 nT for the track of the second day. This results in -11 nT for the difference.

Figure 4.3 shows a similar situation two month later in December 2000, when the satellite was flying in a noon-midnight orbit (1200 - 2400 LT). This measurement is taken when the satellite path is crossing the equator, flying North, on the day side at 1146 LT. The track is along the orbital arc from ±50° latitude at the 21° E meridian. Here another prominent feature can be seen: small to medium-scale undulations which are caused dominantly by ionospheric currents (equatorial electrojet, Sq currents). When calculating the difference between the two tracks the small-scale features do not disappear, since they are not stationary in time. The residuals of the ionospheric currents are added to the ring current effect. In Chapter 5 it will be shown that noon-time estimates exhibit the largest scatter.

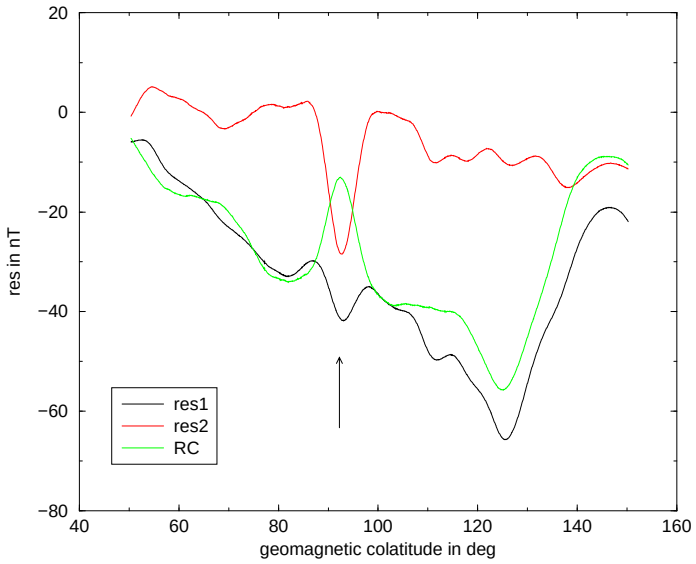

Figure 4.3: Repeat track on 24 and 27 Dec. 2000, day side at 1146 LT: Calculated residuals of the first (black) and second (red) day and the difference of these residuals (green) are presented. The arrow points out the equatorial electrojet

4.2 SHA description of the ring current signal using scalar data

An introduction in using SHA in modelling the Earth's magnetic field has already been presented in Section 2.4. For determining a main field model typically an interval of 3 to 5 quiet days is used. The external field resulting from the modelling is the average over the interval considered. The magnetospheric currents are known to be rather variable on all time scales. Changes taking place within the corresponding interval have to be corrected before the inversion.

For simplicity two assumptions are made:

- only the ring current is the main part of the external field
- the ring current is axially symmetric around the dipole axis of the Earth, which only takes into account terms with order $m = 0$.

For the external part, this simplifies Eq. 2.8 to 2.10 in the following way:

$$b_r = \sum_{n=1}^{2} \left\{ (n+1) g_n^0 \left(\frac{a}{r}\right)^{n+2} - n q_n^0 \left(\frac{r}{a}\right)^{n-1} \right\} P_n^0(\cos\theta), \tag{4.1}$$

$$b_\theta = -\sum_{n=1}^{2} \left\{ g_n^0 \left(\frac{a}{r}\right)^{n+2} + q_n^0 \left(\frac{r}{a}\right)^{n-1} \right\} \frac{dP_n^0(\cos\theta)}{d\theta}, \tag{4.2}$$

$$b_\phi = 0. \tag{4.3}$$

For an absolutely symmetric ring current which is only allowed to move up and down along the rotation axis the use of **geomagnetic** coordinates is appropriate. Therefore, the position, usually given in geocentric coordinates, has to be transformed into this geomagnetic coordinate system.

A comfortable description of the geomagnetic field can be obtained by a magnetic dipole in the Earth's centre. The horizontal direction in the dipole system is shown by the angle ψ against the true North direction. The transformation from geocentric to geomagnetic dipole coordinates (indicated by a star, *) is obtained by application of a rotation matrix:

$$\mathbf{B}^*(r,\theta,\phi) = \begin{pmatrix} B_r^* \\ B_\theta^* \\ B_\phi^* \end{pmatrix} = \begin{pmatrix} 1 & 0 & 0 \\ 0 & \cos\psi & \sin\psi \\ 0 & -\sin\psi & \cos\psi \end{pmatrix} \begin{pmatrix} B_r \\ B_\theta \\ B_\phi \end{pmatrix}, \tag{4.4}$$

where ψ is the angle between the geographic and geomagnetic meridian [Kertz, 1989]. The poles of this dipole are changing in time (Tab. 4.2).
For the transformation the pole (latitude β_B and longitude ϕ_B) of this dipole has to be known. In this work the latitude and the longitude are calculated from the 'International Geomagnetic Reference Field 2000' [Olsen et al., 2000b] (IGRF2000: $g_1^0 = -29615.0$ nT, $g_1^1 = -1728.0$ nT, $h_1^1 = 5186.0$ nT). With

$$H = \sqrt{(g_1^0)^2 + (g_1^1)^2 + (h_1^1)^2} \tag{4.5}$$

Coordinates of the magnetic poles:			
		latitude	longitude
arctic	1984	77°00′ N	102° 18′ W
	1994	78° 18′ N	104° 00′ W
	2001	81° 18′ N	110° 48′ W
antarctic	1962	67° 30′ S	140° 00′ W
	1986	65° 20′ S	139° 10′ W
	2000	64° 40′ S	138° 20′ W

Table 4.1: Geographic coordinates of the arctic and antarctic magnetic pole. Values from Mandea & Dormy [2003].

the horizontal component results in $H = 30115.3$ nT. And from the two following equations:

$$\cos\theta_B = \frac{-g_1^0}{H} \tag{4.6}$$

$$\tan\phi_B = \frac{h_1^1}{g_1^1} \tag{4.7}$$

the obtained colatitude and longitude of the geomagnetic pole are $\theta_B = 10.46°$ and $\phi_B = 288.43°$, respectively. From the position of the geomagnetic pole and the actual position of the satellite (geocentric latitude, β and longitude, ϕ), the geomagnetic latitude ($\beta^\star$), the geomagnetic longitude ($\phi^\star$) and the shown angle (ψ) can be computed:

$$\sin\beta^\star = \sin\beta_B \cdot \sin\beta + \cos\beta_B \cdot \cos\beta \cdot \cos(\phi - \phi_B) \tag{4.8}$$

$$\sin\phi^\star = \frac{\cos\beta \cdot \sin(\phi - \phi_B)}{\cos\beta^\star} \tag{4.9}$$

$$\sin\psi = -\frac{\cos\beta_B \cdot \sin(\phi - \phi_B)}{\cos\beta^\star}. \tag{4.10}$$

ψ will then be used in the transformation matrix of Equation 4.4.

In this first model only latitudes of $\pm 50°$ around the geomagnetic equator are used

because at higher latitudes the field is more influenced by other currents, e. g., currents at polar latitudes may cause problems.

The difference of the total field residuals (ΔRC) between two adjacent repeat tracks is treated as the signal to be investigated in subsequent calculations. The underlying assumption is that all varying magnetic fields are generated by linear processes. In that case ΔRC can be treated as the residuals themselves which represent the effect of an additional field on top of the main field.

In spherical harmonics (simplifying Eq. 2.8 and 2.9) the additional axisymmetric field can be expressed as:

$$b_r = 2\tilde{g}_1^0 \left(\frac{a}{r}\right)^3 \cos\theta^\star - \tilde{q}_1^0 \cos\theta^\star - \tilde{q}_2^0 \left(\frac{r}{a}\right) (3\cos^2\theta^\star - 1) \tag{4.11}$$

$$b_\theta = \tilde{g}_1^0 \left(\frac{a}{r}\right)^3 \sin\theta^\star + \tilde{q}_1^0 \sin\theta^\star + 3\tilde{q}_2^0 \left(\frac{r}{a}\right) \sin\theta^\star \cos\theta^\star \tag{4.12}$$

$$b_\phi = 0 \tag{4.13}$$

with a = 6371.2 km (the radius of the reference sphere), r is the radius and $\theta^\star$ the colatitude of the satellite position in geomagnetic coordinates. Because of the limitation to $m = 0$ there is no longer a dependence on the longitude $\phi^\star$.

The observed difference ΔRC can be equated to the sum of the internal field (B_r, B_θ, B_ϕ from main field model) and the components of the additional field (unknown field, b_r, b_θ, b_ϕ):

$$\Delta RC = \sqrt{(B_r + b_r)^2 + (B_\theta + b_\theta)^2 + (B_\phi + b_\phi)^2} - |B|. \tag{4.14}$$

The effect of the ring current has the order of 0.2% of the main field intensity at the Earth's surface. That justifies the linearisation of equation (4.14) and

$$\Delta RC = \frac{B_r b_r + B_\theta b_\theta + B_\phi b_\phi}{|B|}. \tag{4.15}$$

A linear relation between the 'measured' difference (ΔRC) and the SHA coefficients is obtained:

$$\Delta RC = c_1\tilde{g}_1^0 + c_2\tilde{q}_1^0 + c_3\tilde{q}_2^0. \tag{4.16}$$

The factors c_1,c_2,c_3 only depend on known variables and can be calculated for each position:

$$c_1 = \frac{1}{|B|}(2B_r\left(\frac{a}{r}\right)^3\cos\theta^\star + B_\theta\left(\frac{a}{r}\right)^3\sin\theta^\star) \tag{4.17}$$

$$c_2 = \frac{1}{|B|}(-B_r\cos\theta^\star + B_\theta\sin\theta^\star) \tag{4.18}$$

$$c_3 = \frac{1}{|B|}(-B_r\left(\frac{r}{a}\right)(3\cos^2\theta^\star - 1) + 1.5B_\theta\left(\frac{r}{a}\right)\sin\theta^\star\cos\theta^\star). \tag{4.19}$$

These elements are dependent on the geomagnetic colatitude, $\theta^\star$, the height and the components of the main field which is presented by the CO2 model.

All k data points along one orbital arc between 40° and 140° colatitude get their own Equation (4.16). This system of equations can be written as:

$$\underline{\underline{C}} \cdot \mathbf{gq} = \mathbf{\Delta RC}, \tag{4.20}$$

where $\mathbf{\Delta\ RC}$ is the k-dimensional vector of the measurements, $\mathbf{gq}$ is the 3-dimensional vector of the results with the components $\tilde{g}_1^0$, $\tilde{q}_1^0$, $\tilde{q}_2^0$ and $\underline{\underline{C}}$ is the k-by-3 matrix containing all c_n (c_1, c_2 and c_3) for each data point. This matrix combines the unknown $\tilde{g}$'s and $\tilde{q}$'s with the measurements.

To get the unknowns, Equation (4.20) can be solved by matrix inversion:

$$\mathbf{gq} = (\underline{\underline{C^T}} \cdot \underline{\underline{C}})^{-1} \cdot \underline{\underline{C^T}} \cdot \mathbf{\Delta RC} \tag{4.21}$$

After the inversion the result is a set of coefficients ($\tilde{g}_1^0$, $\tilde{q}_1^0$ and $\tilde{q}_2^0$) for one track from 40° to 140° geomagnetic colatitude.

4.3 Results of external field modelling

To show the quality of the resulting coefficients the modelled differences of the ring current effect are compared with the ΔRC derived from the data. Figures 4.4 and

4.5 show the results of modelling external field effects for the same tracks as in Section 4.1 and their following tracks, i. e. the dusk track after the dawn track in October 2000 and the night side track following the day side track in December 2000.

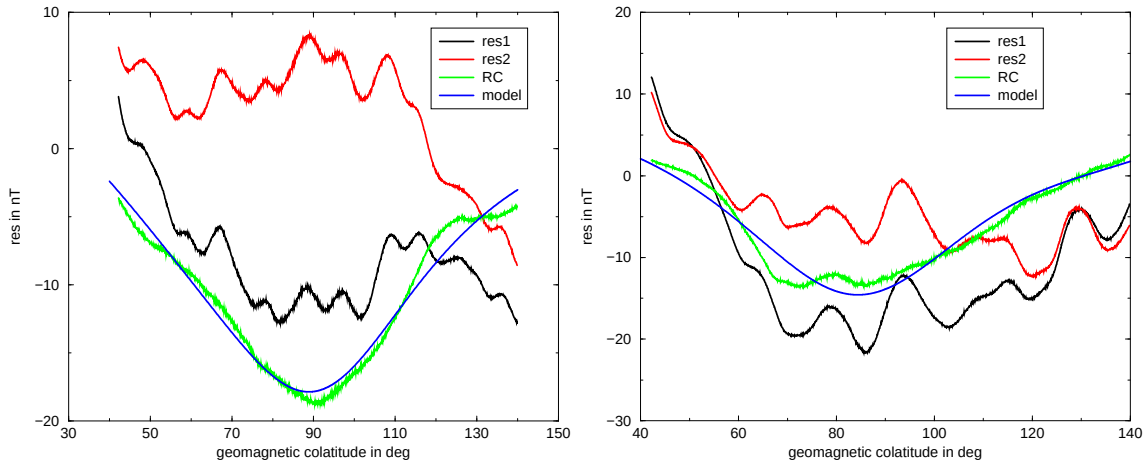

Figure 4.4: 24th and 27th of October 2000, dawn side (left panel) and dusk side (right panel). In each panel, the two residuals of the total field intensity for the first (res1, black line) and the repeat day (res2, red line) and their difference (RC, green line) are shown. The solid blue line illustrates the model result.

Figure 4.4 (left panel) is showing again the dawn side track of the residuals from the 24 and 27 October 2000. Additionally the result of the inversion (blue line) is plotted.

The readings for the dusk side track in Figure 4.4 (right panel) are from the consecutive track (1717 LT), when CHAMP was flying 'on the other side' of the Earth. Here, also small to medium-scale undulations can be found which disappear after calculating the difference of the residuals for the two repeat tracks. The model again is very promising.

One problem, as explained in Section 4.1, can be seen in the day side curve in Figure 4.5 (left panel). The external field on the day side is influenced by ionospheric currents which are not considered in the inversion. At about 90° geomagnetic colatitude the equatorial electrojet and its effect in the differences can be seen clearly.

Perhaps due to the influence of the electrojet and other ionospheric currents the modelled curve does not fit the measurements as good as in the other graphs.

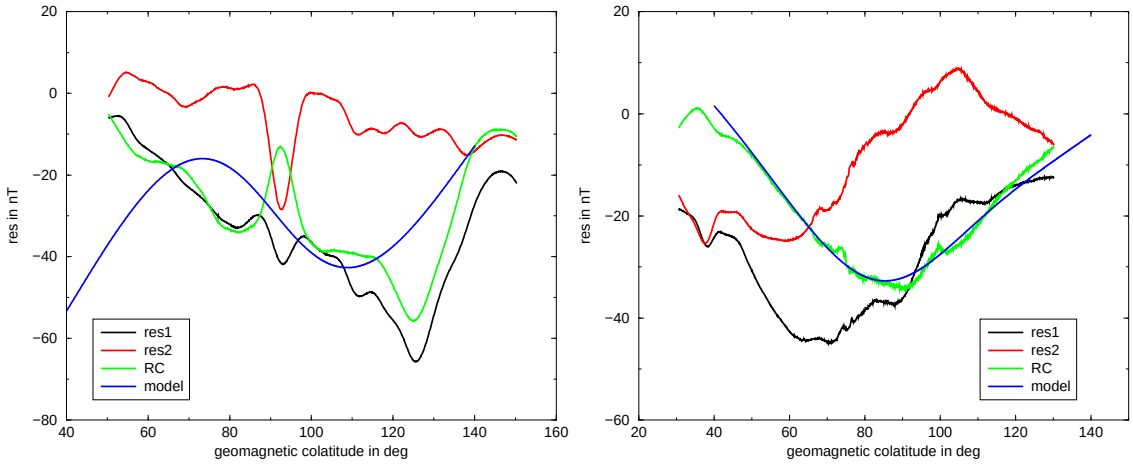

Figure 4.5: 24th and 27th of December 2000, day side (left panel) and night side (right panel). In each panel, the two residuals of the total field intensity for the first (res1, black line) and the repeat day (res2, red line) and their difference (RC, green line) are shown. The solid blue line illustrates the model result.

The last example of **'model 1'** is the consecutive night side track (Fig. 4.5, right panel) in December 2000. The satellite was crossing the equator at 2346 LT on 24 December 2000. Similar signatures of the lithosphere to the one of the dawn and dusk tracks (Fig. 4.4) can be seen. Also the ionospheric currents are again negligible and after taking the difference between the two tracks on 24 and 27 December 2000 the wiggles largely disappear. The model fit is very good.

4.4 Correlation of spherical harmonic coefficients with magnetic indices

A common index to describe the effect of the ring current at the Earth's surface is the D_{ST} index (see Chap. 2). Another index is the 'ring current' index RC*. It has been kindly provided by Olsen [2002]. It is determined from many observatories in the midnight sector.

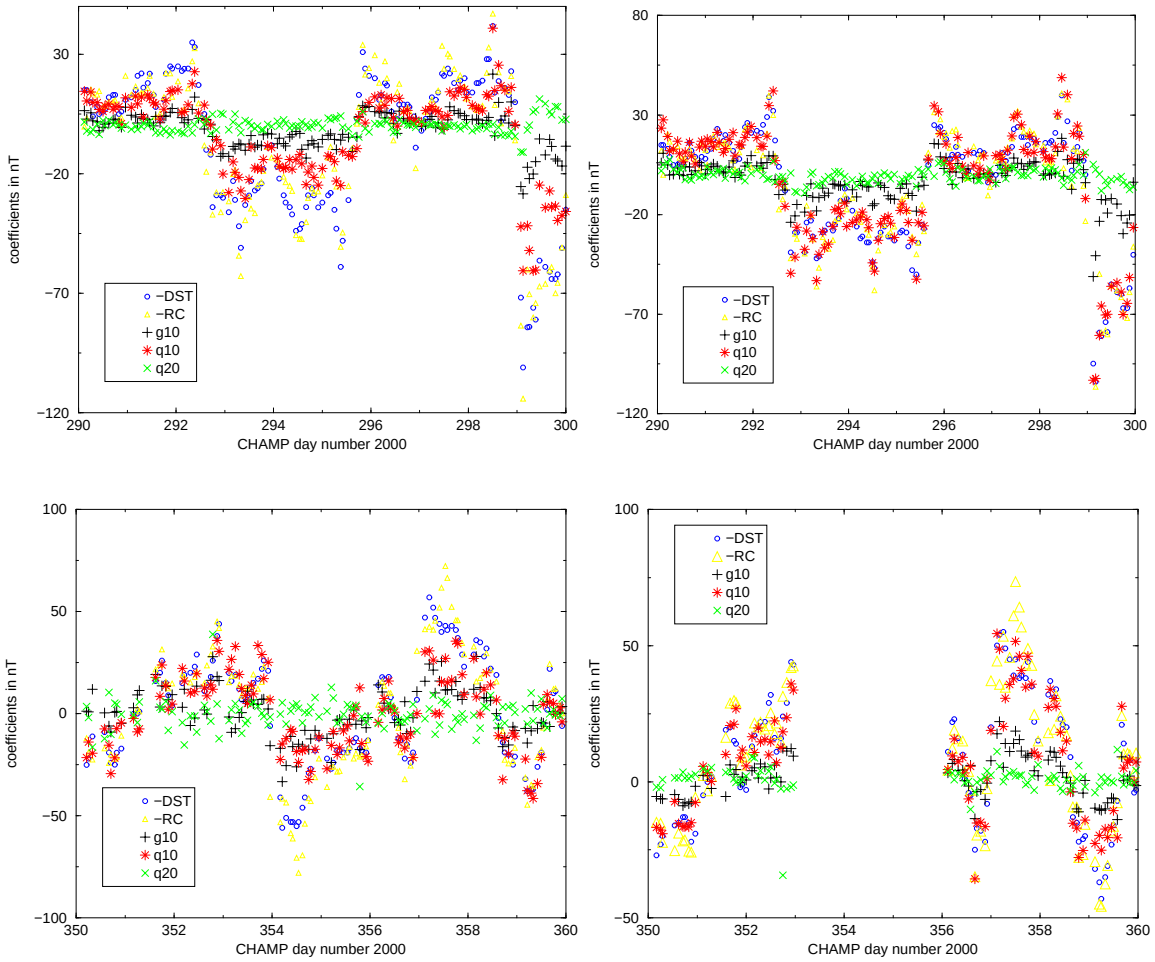

Figure 4.6: Top: Period of 10 days in October 2000, dawn side (left panel) and dusk side (right panel). Bottom: Period of 10 days in December 2000, day side (left panel) and night side (right panel, gap due to missing data). The coefficients ($\tilde{g}_1^0$ (black crosses), $\tilde{q}_1^0$ (red stars) and $\tilde{q}_2^0$ (green pluses)) are compared to the D_{ST} index (blue circles) and RC* index (yellow triangles).

Figure 4.6 shows the three SHA coefficients ($\tilde{g}_1^0$, $\tilde{q}_1^0$ and $\tilde{q}_2^0$) that are obtained from the inversion over a period of 10 days both in October and December 2000. It can be seen that the model for the dawn side track fits very well. The $\tilde{g}_1^0$ term represents the induced internal field, $\tilde{q}_1^0$ describes the symmetric part of the ring current. The $\tilde{q}_1^0$ coefficient is the one of main interest and will be compared with commonly used indices. The importance of $\tilde{q}_2^0$ is not very clear up to now. In Figure 4.6 (top) the

calculated $\tilde{q}_1^0$ for October 2000 obtained from the dawn and dusk orbits is compared with the two indices. Since the differences between repeat tracks are considered, also the differences in D_{ST} and RC* between the epochs of CHAMP equator crossings are used. The hour (in LT) of the equator crossing of the first repeat tracks gives the timing which is presented.

Figure 4.6 (bottom) shows two diagrams with the similar situation in December 2000. The satellite orbit is now in the noon-midnight-orbit near 1200 and 2400 LT.

As Figure 4.6 shows, the $\tilde{q}_1^0$ term (expected to describe the ring current) follows the D_{ST} index and the RC* index rather closely. There is, however, a clear difference in amplitude between $\tilde{q}_1^0$ and the indices. While in the dusk sector $\tilde{q}_1^0$ values are comparable with D_{ST} and RC*, their amplitude is a bit smaller on the night side, but they are significantly smaller in the dawn and noon sector. This is consistent with the fact that the RC* index has been specially developed for the night side. Also the internal term $\tilde{g}_1^0$ tracks the indices reasonably well, but at a lower level. In contrast, $\tilde{q}_2^0$ varies around zero and shows no local time dependence.

After having presented the qualitative relations between the derived SHA coefficients and the ring current indices, the correlation parameters of the quantities will be analysed. In particular the correlations of $\tilde{q}_1^0$ with the D_{ST} and RC* index, the $\tilde{g}_1^0$ and $\tilde{q}_2^0$ will be shown. The obtained coefficient $\tilde{q}_1^0$ describes the homogeneous external part of the geomagnetic field.

Figure 4.7 (left panel) shows the dependence of $\tilde{q}_1^0$ on the magnetic index D_{ST}. A good correlation for the four local times is found. The linear regression curves show different slopes for the various local times. All lines intercept close to zero (as can be seen in Table 4.2).

In Figure 4.7 (right panel) $\tilde{q}_1^0$ is also compared with the RC* index. One can see a very good correlation of $\tilde{q}_1^0$ with D_{ST} and RC*, respectively. Both indices are very similar, apparently exhibiting no significant differences. In order to proof this, the correlation between the two indices is plotted in Figure 4.8. It shows good correlation between the two indices. Since the D_{ST} index is readily available from

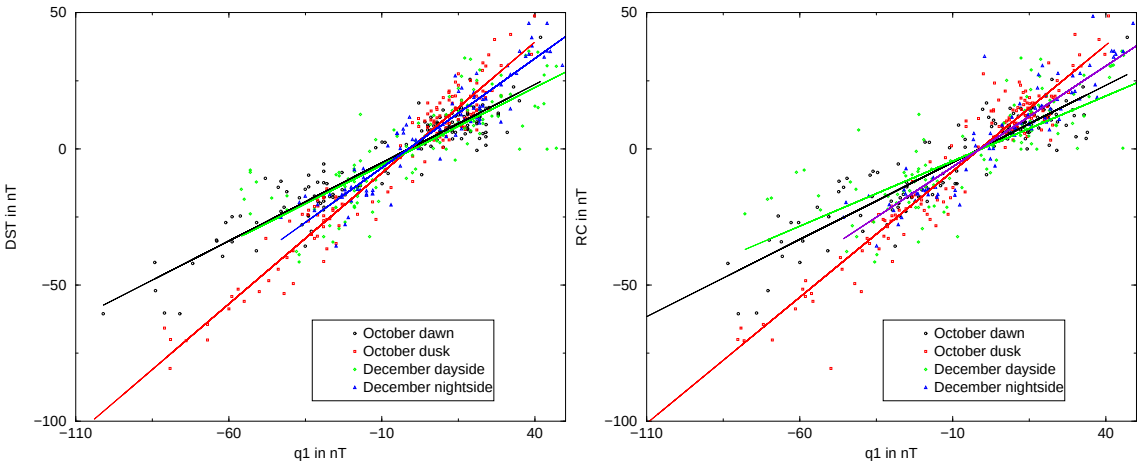

Figure 4.7: Correlation between D_{ST} and q_1^0 (left panel) and correlation between RC* and q_1^0 (right panel).

geomagnetic data centres (e. g., see [WDC-Kyoto, 2003]), it will be used further in this study.

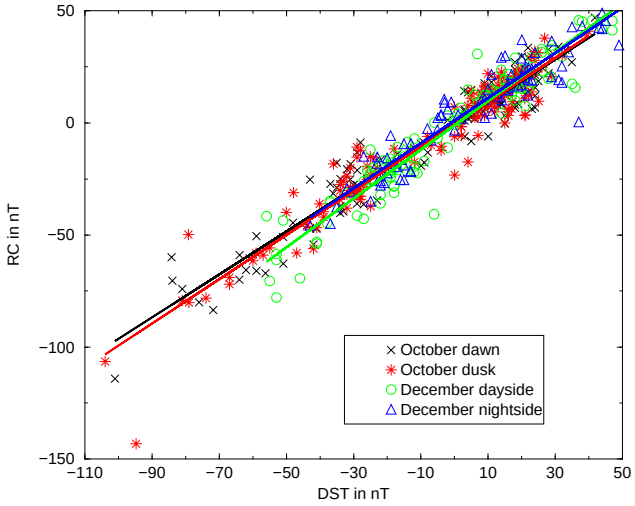

Figure 4.8: Correlation between D_{ST} and RC* index.

Figure 4.9 (left panel) depicts the correlation between $\tilde{g}_1^0$ and $\tilde{q}_1^0$ which is very good. Except for the day side, the correlations are very good, and the regression lines have similar slopes for the different local times.

Since $\tilde{g}_1^0$ is an internal coefficient, it reflects the induction caused by the ring current effect. The deviating slope at noon is another indication that the method so far pre-

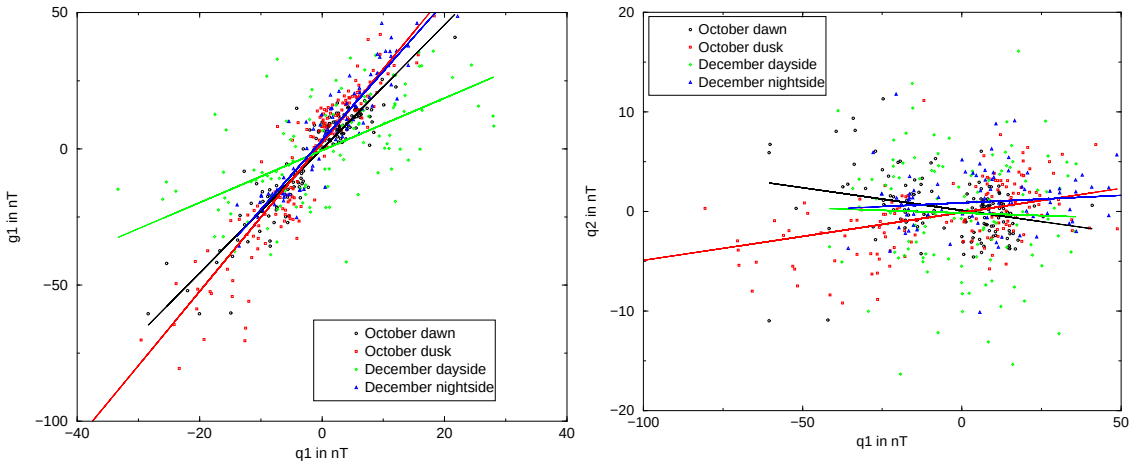

Figure 4.9: Correlation between $\tilde{g}_1^0$ and $\tilde{q}_1^0$ (left panel) and correlation between $\tilde{q}_1^0$ and $\tilde{q}_2^0$ (right panel) for the four local time periods in October and December 2000.

sented may not reveal the ring current effect reliably on the day side. For example, also the effect of the electrojet and the Sq currents are not included. There is no correlation between $\tilde{q}_1^0$ and $\tilde{q}_2^0$ (Fig. 4.9, right panel). All the correlation coefficients and the slopes are small. The coefficient $\tilde{q}_2^0$ is obviously not controlled by the ring current effect.

The numerical results of the correlation analysis are compiled in Table 4.2. It indicates the high degree of correlation obtained between the coefficient $\tilde{q}_1^0$ and the indices D_{ST} and RC*. On average D_{ST} is slightly better over all local times. The excellent correlation between $\tilde{g}_1^0$ and $\tilde{q}_1^0$ (except day side) becomes also clear (see column '$\tilde{g}_1^0$ vs $\tilde{q}_1^0$' in the top section of the table).

How do the slopes obtained here compare with results from other studies? Langel et al. [1996] recommended for the correction of the ring current effect to use on the dawn side $\tilde{q}_1^0 = 18.6 - 0.63 \cdot D_{ST}$ and $g_1^0 = -29992.3 + 0.29 \cdot \tilde{q}_1^0$ and for the dusk side $\tilde{q}_1^0 = 20.3 - 0.68 \cdot D_{ST}$ and $g_1^0 = -29987.7 + 0.24 \cdot \tilde{q}_1^0$. The results of this study imply a significantly larger difference between dawn and dusk for $\tilde{q}_1^0/D_{ST}$. The average value of this ratio is about 17 % larger. In case of the ratio between external and internal part, $\tilde{q}_1^0/\tilde{g}_1^0$ the ratio is even larger by some 50 % than those from Langel

Correlation Coefficient					
	D_{ST} vs RC*	D_{ST} vs $\tilde{q}_1^0$	RC* vs $\tilde{q}_1^0$	$\tilde{g}_1^0$ vs $\tilde{q}_1^0$	$\tilde{q}_1^0$ vs $\tilde{q}_2^0$
October, dawn	0.97	0.94	0.92	0.93	-0.27
October, dusk	0.96	0.97	0.96	0.94	0.41
December, day side	0.96	0.83	0.79	0.60	-0.03
December, night side	0.93	0.93	0.93	0.94	0.06
Slope					
	D_{ST} vs RC*	D_{ST} vs $\tilde{q}_1^0$	RC* vs $\tilde{q}_1^0$	$\tilde{g}_1^0$ vs $\tilde{q}_1^0$	$\tilde{q}_1^0$ vs $\tilde{q}_2^0$
October, dawn	0.96	0.57	0.57	2.28	-0.05
October, dusk	0.99	0.96	0.93	2.72	0.05
December, day side	1.09	0.57	0.48	0.96	-0.01
December, night side	1.01	0.80	0.74	2.53	0.01
Intercept					
	D_{ST} vs RC*	D_{ST} vs $\tilde{q}_1^0$	RC* vs $\tilde{q}_1^0$	$\tilde{g}_1^0$ vs $\tilde{q}_1^0$	$\tilde{q}_1^0$ vs $\tilde{q}_2^0$
October, dawn	-0.48	0.63	0.68	-0.07	0.12
October, dusk	-0.64	0.75	1.03	2.08	-0.09
December, day side	-1.09	-0.28	0.27	-0.58	-0.14
December, night side	0.98	1.04	0.79	3.06	0.88

Table 4.2: Correlation results of **'model 1'**.

et al. [1996]. Further studies have to be done in order to verify these differences.

In a recent paper, Olsen [2002] used Ørsted data from 1900 LT through the night side to 0700 LT for main field modelling. He finds a ratio $\tilde{q}_1^0/RC^* = 0.70$ for the ring current effect. If the average of the three slopes of $\tilde{q}_1^0/RC^*$ for dawn, dusk and night side are taken, 0.74 results which is close to the value found by Olsen. In that paper the ratio $\tilde{q}_1^0/\tilde{g}_1^0$ was not further examined.

4.5 Local time dependence

From only these four periods (0600/1800 and 0000/1200 LT) a local time dependence of the slope of the linear regression is estimated by a harmonic expansion.

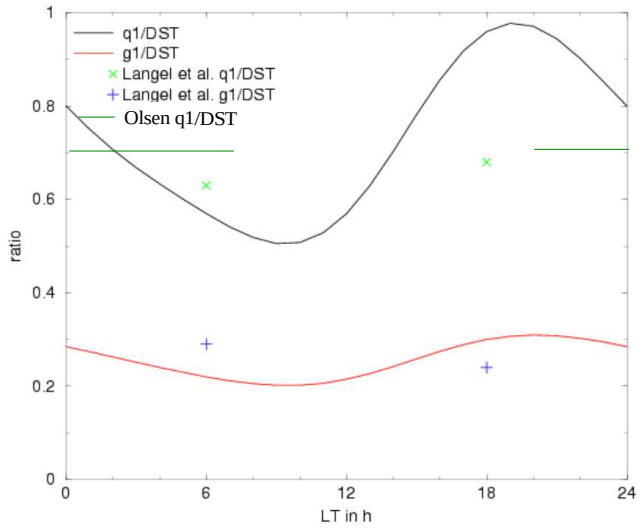

Figure 4.10: Resulting local time dependence of the four considered time periods compared with published values.

The result is shown in Figure 4.10. Only a restricted comparison to other studies is possible. Therefore the plot has to be improved. Vector data will allow a direct separation between internal and external parts.

The assumption of a totally symmetric ring around the equator is rather simple. One possible arrangement in the equatorial plane of the magnetosphere is shown in Figure 4.11. It seems, the external contribution is more influenced by the asymmetric, partial ring current (PRC), the magnetopause (MP) and tail current (TC) than expected. One has to look at it in more detail. Probably an asymmetric, ring current which is moving up and down along the rotation axis is describing the situation better.

The maximum at about 1800 LT would be caused by the ring current, the partial ring current and the tail current. An explanation for the minimum at about 1000 LT maybe the direction of the magnetopause current which is in the opposite direction then the ring current.

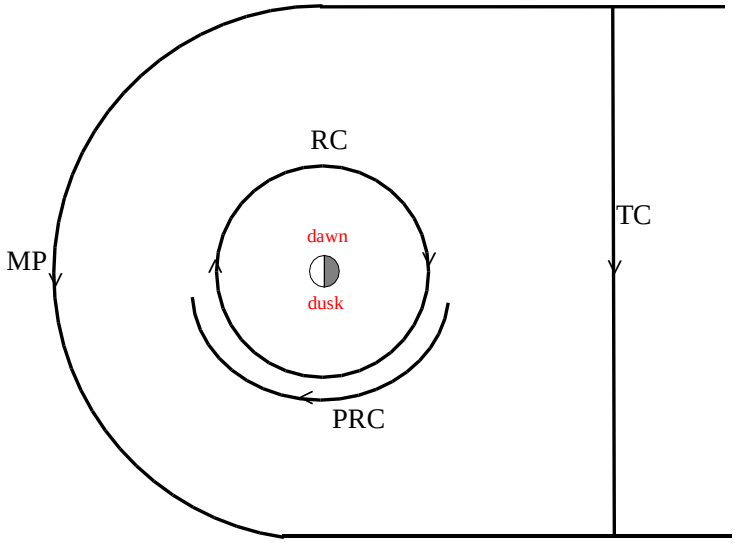

Figure 4.11: Magnetospheric currents in the equatorial plane: ring current (RC), partial ring current (PRC), magnetopause current (MP), and tail current (TC), after [Kivelson & Russell, 1995].

4.6 Conclusion for 'model 1'

The ring current effect in scalar satellite data is determined by inverting the measurements. In contrast to previous approaches only differences between ***repeat tracks*** which are separated by a couple of days are considered. This procedure removes problems caused by biases and slow trends both in satellite data, main field model and ring current indices.

The obtained correlations of the homogeneous external field with ring current indices and with the induced field are excellent for most local times. Poor results are obtained on the day side where the E region currents are significant.

It has to be noted that the ratio between the external coefficient $\tilde{q}_1^0$, and the D_{ST} index has a rather strong dependence on LT. This means, the equation for correcting the data becomes LT dependent. For an orbit in the dawn/dusk plane the correction

function is plotted in Figure 4.12 for the two successive orbit parts. It is evident that the two graphs do not match at the poles. There is a discrepancy of the order of 5 nT. This problem has not been addressed in the literature. It is well possible that all present main field models suffer from it, giving rise to errors of the order of 5 nT at the poles.

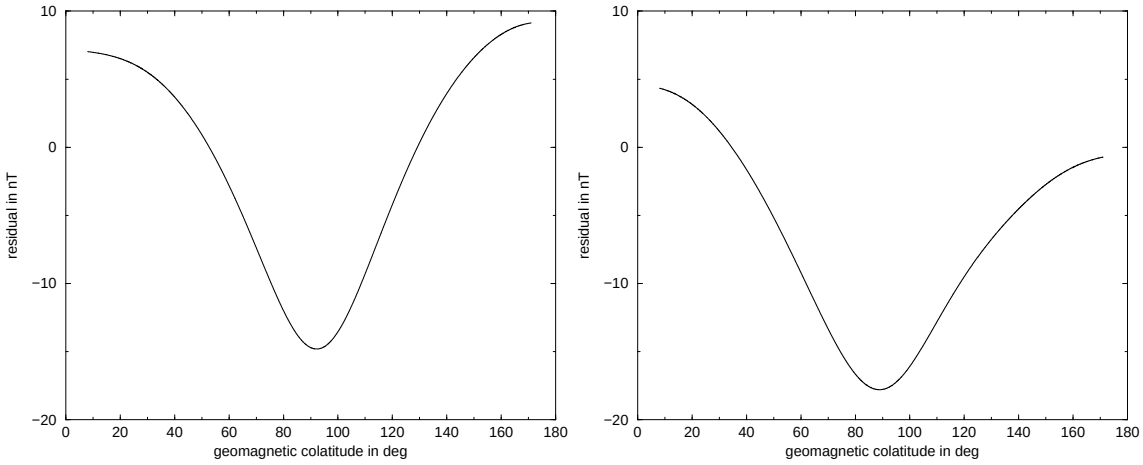

Figure 4.12: Modelled calculation to the poles of an orbit in the dawn/dusk plane. Inversion for tracks expanded from 10° to 170°, almost one whole orbit, which show the discrepancy at the connecting point.

Chapter 5

Modelling external currents from vector data

In principle vector data are always best for any kind of magnetic field modelling. The use of scalar data (previous chapter) showed that there are still problems which cannot be solved by using only the total field intensity. Vector data are used to find out more about the behaviour at the poles and the local time dependence of the ring current. It is not necessary to have a look at all three components of the vector data. The vertical and one horizontal component can be inverted directly. The computations then give the Gauss coefficients which describe the external currents.

5.1 Inversion of ring current signal

Using vector data one can do a straight forward inversion of each component. Only the vertical component and one horizontal component is necessary. The horizontal component, X, is chosen because Y is most disturbed by the influence of field aligned currents.
Here, the calculations of the vector data are done for the orbit height ($a = r$) and the longitude was set to $\Phi = 0°$ in case CHAMP was flying northward and $\Phi = 180°$ if the satellite was flying southward. $m = 0$ is no longer assumed.
In this attempt, called **'model 2'**, the two components used can be described by SHA like:

$$\begin{aligned} b_r &= \{2\tilde{g}_1^0 - \tilde{q}_1^0\}\cos\theta^\star \\ &\quad +\{2\tilde{g}_1^1 - \tilde{q}_1^1\}\sin\theta^\star\cos\phi^\star \\ &\quad +\{3\tilde{g}_2^0 - 2\tilde{q}_2^0\}\frac{1}{2}(3\cos^2\theta^\star - 1) \\ &\quad +\{3\tilde{g}_2^1 - 2\tilde{q}_2^1\}\sqrt{3}\cos\theta^\star\sin\theta^\star\cos\phi^\star \end{aligned} \tag{5.1}$$

$$\begin{aligned} b_\theta &= \{\tilde{g}_1^0 + \tilde{q}_1^0\}\sin\theta^\star \\ &\quad -\{\tilde{g}_1^1 + \tilde{q}_1^1\}\cos\theta^\star\cos\phi^\star \\ &\quad +\{\tilde{g}_2^0 + \tilde{q}_2^0\}3\sin\theta^\star\cos\theta^\star \\ &\quad -\{\tilde{g}_2^1 + \tilde{q}_2^1\}\sqrt{3}(\cos^2\theta^\star - \sin^2\theta^\star)\cos\phi^\star \end{aligned} \tag{5.2}$$

with $\cos\phi^\star = 1$ or -1, depending on the flight direction of CHAMP. Equations 5.1 and 5.2 are the description of the components at one point. The expressions in brackets are presenting the combination of Gauss coefficients, $\tilde{g}_n^m$ and $\tilde{q}_n^m$ (e. g., $c_1^0 = 2\tilde{g}_1^0 - \tilde{q}_1^0$, $d_1^0 = \tilde{g}_1^0 + \tilde{q}_1^0$) which have to be found. Everything that is depending on the position ($\theta^\star$, $\phi^\star$) in Equations 5.1 and 5.2 is combined in the k-by-4 matrices $\underline{\underline{P}}$ and $\underline{\underline{dP}}$. For each track (later on for each orbit) it can be written as:

$$\mathbf{b_r} = \underline{\underline{P}} \cdot \mathbf{C} \qquad \text{and} \qquad \mathbf{b}_\theta = \underline{\underline{dP}} \cdot \mathbf{D}. \tag{5.3}$$

One has to do two inversions to get the 'helping' coefficients c_n^m and d_n^m for each combination of order n and degree m which are combined in $\mathbf{C}$, $\mathbf{D}$ respectively, for each track.

$$\mathbf{C} = (\underline{\underline{P^T}} \cdot \underline{\underline{P}})^{-1} \cdot \underline{\underline{P^T}} \cdot \mathbf{b_r} \qquad \text{and} \qquad \mathbf{D} = (\underline{\underline{dP^T}} \cdot \underline{\underline{dP}})^{-1} \cdot \underline{\underline{dP^T}} \cdot \mathbf{b}_\theta \tag{5.4}$$

The results of these inversions give the relation between the 'helping' coefficients (c_n^m, d_n^m) and the corresponding Gauss coefficients ($\tilde{g}_n^m$, $\tilde{q}_n^m$). For each combination of degree n and order m the two 'helping' coefficients are computed:

$$c_n^m = ((n+1)\tilde{g}_n^m - n\tilde{q}_n^m) \qquad \text{and} \qquad d_n^m = (\tilde{g}_n^m + \tilde{q}_n^m). \tag{5.5}$$

From these equations the set of Gauss coefficients can be calculated (using their relation from Equations 5.1 and 5.2):

$$\tilde{g}_n^m = \frac{c_n^m + n d_n^m}{2n+1} \qquad \text{and} \qquad \tilde{q}_n^m = \frac{(n+1)d_n^m - c_n^m}{2n+1}. \tag{5.6}$$

For a robust model, first the inversion is done only for n=1 and m=0, followed by a 2σ-throwout. This procedure is repeated before a complete model is generated for all coefficients (n=1,2 and m=0,1). Since the terms of degree and order 2 are no longer linearly independent in a single orbit solution the summation is stopped at the order 1.

5.1.1 Comparison with 'model 1'

To confirm that **'model 2'** is valid, a comparison with **'model 1'** is done. For the comparison the same conditions are chosen, i.e. two weeks of data in October and December 2000 and only coefficients up to degree $n = 2$ and order $m = 0$ are used. That simplifies Equations 5.1 and 5.2 to:

$$\begin{aligned} b_r &= \{2\tilde{g}_1^0 - \tilde{q}_1^0\}\cos\theta^\star \\ &\quad + \{3\tilde{g}_2^0 - 2\tilde{q}_2^0\}\frac{1}{2}(3\cos^2\theta^\star - 1) \end{aligned} \tag{5.7}$$

$$\begin{aligned} b_\theta &= \{\tilde{g}_1^0 + \tilde{q}_1^0\}\sin\theta^\star \\ &\quad + \{\tilde{g}_2^0 + \tilde{q}_2^0\}3\sin\theta^\star\cos\theta^\star. \end{aligned} \tag{5.8}$$

Results of such two repeat tracks in December 2000 are shown in Figure 5.1. On the nightside (Fig. 5.1, right panel) the measured data are very quiet. Only at about 150° geomagnetic colatitude, there are large disturbances caused by auroral/polar currents. On the day side (Fig. 5.1, left panel) is more activity and it is more difficult to model these variations.

For a first quality check of **'model 2'**, as done for **'model 1'**, the obtained coefficients ($\tilde{g}_1^0$, $\tilde{g}_2^0$, $\tilde{q}_1^0$ and $\tilde{q}_2^0$) are compared with D_{ST} (Fig. 5.2). In the top panel the result for the two weeks period in October 2000 is shown. Terms of degree 2 ($\tilde{g}_2^0$, $\tilde{q}_2^0$) vary insignificantly around zero. The coefficients of degree 1, especially the $\tilde{q}_1^0$ term,

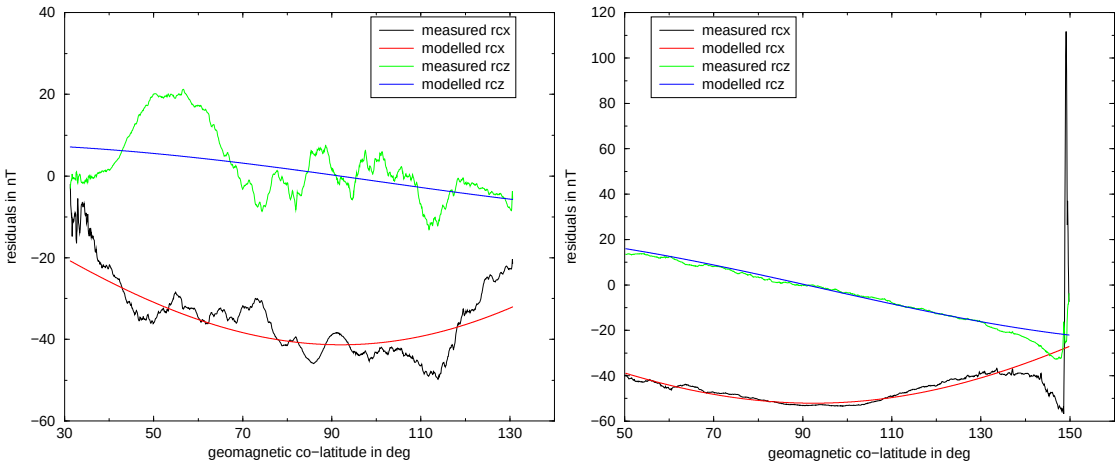

Figure 5.1: 24th and 27th of December 2000, day side (left panel) and night side (right panel), result of **'model 2'** using vector data for tracks from 40° to 140° colatitude.

correlate very well with D_{ST}. That is not surprising, because $\tilde{q}_1^0$ is supposed to describe the effect of external currents - like the D_{ST} index - and $\tilde{g}_1^0$ their induced part.

The comparison with D_{ST} is also done for a two weeks period two month later in December 2000 (Fig. 5.2, bottom). Again, it demonstrates the good agreement. The night side results are of major interest, especially for main field modelling. (Fig. 5.2, bottom, right panel). The $\tilde{q}_1^0$ follows the D_{ST} index very well and the amplitude behaviour agrees well with D_{ST}, although it is a little less on the day side (Fig. 5.2, bottom, left panel).

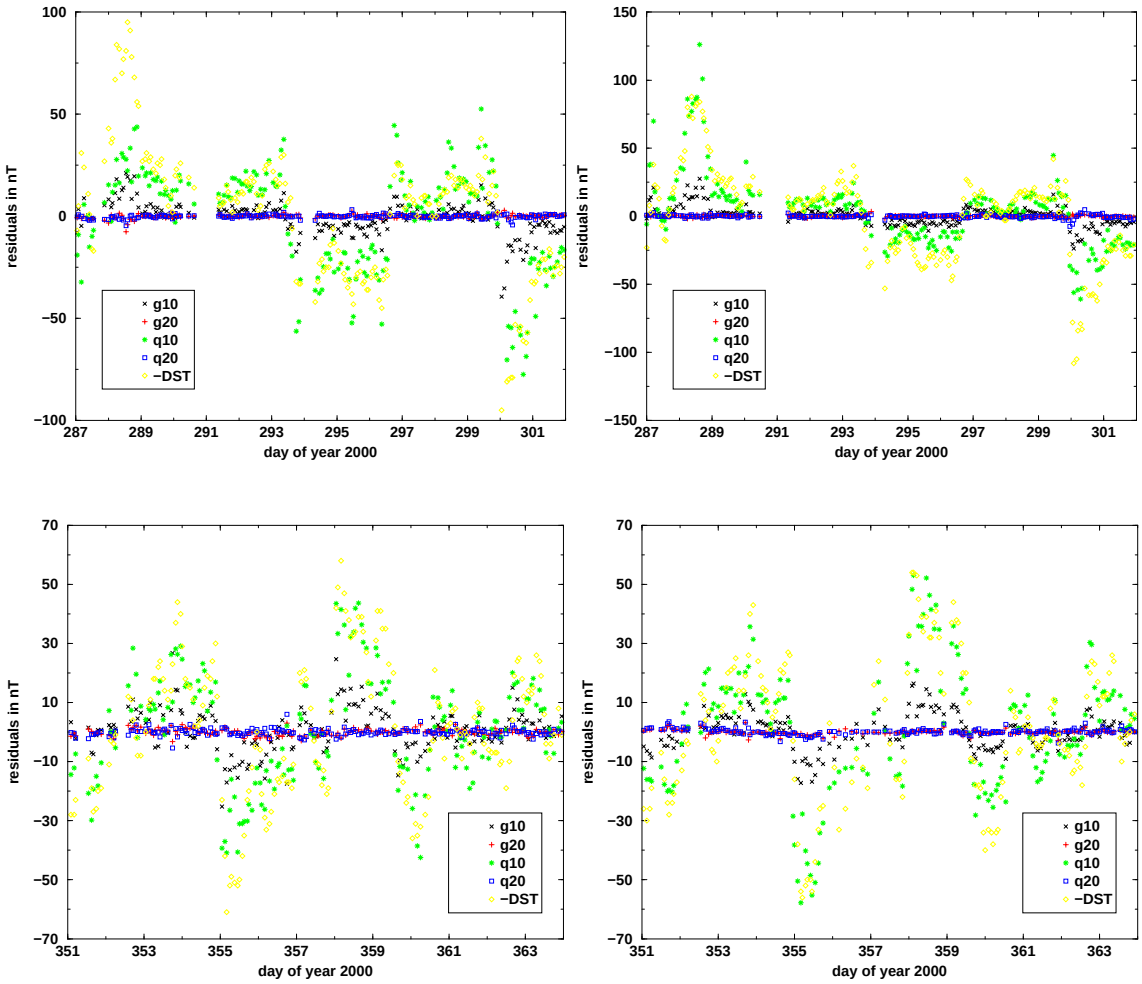

Figure 5.2: Top: Inversion result of 15 days of data in October 2000, dawn side (left panel) and dusk side (right panel); bottom: Inversion result of 13 days of data in December 2000, day side (left panel) and night side (right panel). Compared are the resulting coefficients ($\tilde{g}_1^0$ (black cross), $\tilde{g}_2^0$ (red plus), $\tilde{q}_1^0$ (green star), $\tilde{q}_2^0$ (blue square)) with D_{ST} (yellow diamond).

The following Figure 5.3 shows the correlations between each of the coefficients ($\tilde{g}_1^0$, $\tilde{g}_2^0$, $\tilde{q}_1^0$, $\tilde{q}_2^0$) and D_{ST} for the calculations computed from 13 days of data from December 2000. This example demonstrates very well the correlation of $\tilde{g}_1^0$ and $\tilde{q}_1^0$ with D_{ST}, as expected. Also the low correlations with terms of degree $n = 2$ can be seen.

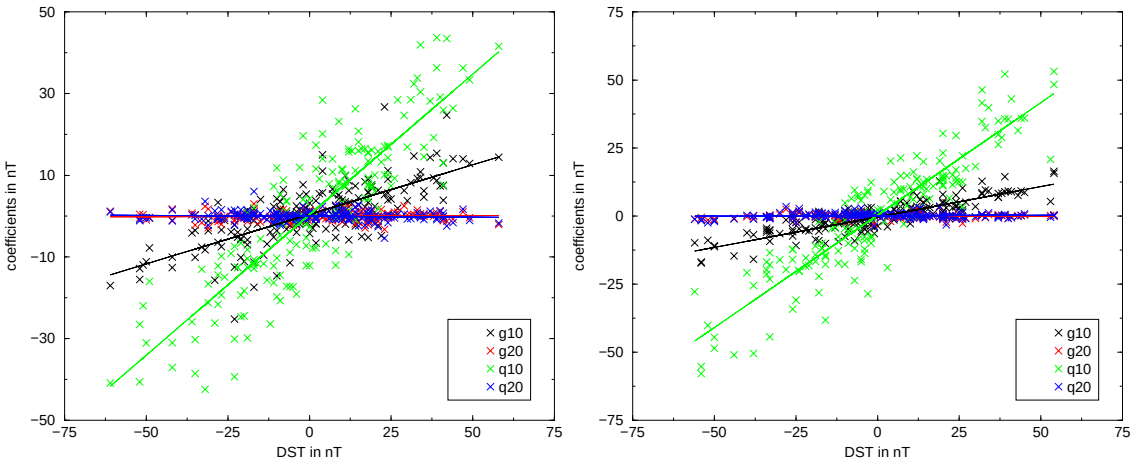

Figure 5.3: December 2000, day side (left panel) and night side (right panel): Coefficients plotted against D_{ST} ($\tilde{g}_1^0$ as black crosses with black regression line, $\tilde{g}_2^0$ as red crosses with red line, $\tilde{q}_1^0$ as green crosses with green line and $\tilde{q}_2^0$ as blue crosses with blue regression line).

Due to the higher significance of correlations of D_{ST} with $\tilde{g}_1^0$ and $\tilde{q}_1^0$, they are compared with each other for the four calculated local time zones.

For comparison, the numerical results between the different local times and the two different models - using scalar or vector data from October and December 2000 - are presented in Table 5.1. The results for both methods are quite similar.

Figure 5.4 depicts the correlations of $\tilde{g}_1^0$ and $\tilde{q}_1^0$ as a function of D_{ST} (left and right panel, respectively). In both panels the good correlations for these four local time zones can be seen.

Correlation Coefficient				
	D_{ST} vs $\tilde{q}_1^0$	D_{ST} vs $\tilde{g}_1^0$	D_{ST} vs $\tilde{q}_1^0$	D_{ST} vs $\tilde{g}_1^0$
Oct, dawn	0.88	0.92	0.94	0.89
Oct, dusk	0.95	0.89	0.97	0.89
Dec, day side	0.87	0.74	0.83	0.81
Dec, night side	0.91	0.87	0.93	0.88
Slope				
	D_{ST} vs $\tilde{q}_1^0$	D_{ST} vs $\tilde{g}_1^0$	D_{ST} vs $\tilde{q}_1^0$	D_{ST} vs $\tilde{g}_1^0$
Oct, dawn	0.46	0.18	0.57	0.22
Oct, dusk	0.96	0.24	0.96	0.30
Dec, day side	0.69	0.24	0.57	0.35
Dec, night side	0.83	0.22	0.80	0.28
Intercept				
	D_{ST} vs $\tilde{q}_1^0$	D_{ST} vs $\tilde{g}_1^0$	D_{ST} vs $\tilde{q}_1^0$	D_{ST} vs $\tilde{g}_1^0$
Oct, dawn	0.01	-0.36	0.63	0.09
Oct, dusk	-0.63	-1.69	0.75	-0.82
Dec, day side	0.36	0.44	-0.28	0.41
Dec, night side	0.39	-0.28	1.04	-0.51

Table 5.1: Statistical results of the comparison between the Gauss coefficients and D_{ST} for **'model 1'** (right columns) and **'model 2'** (left columns).

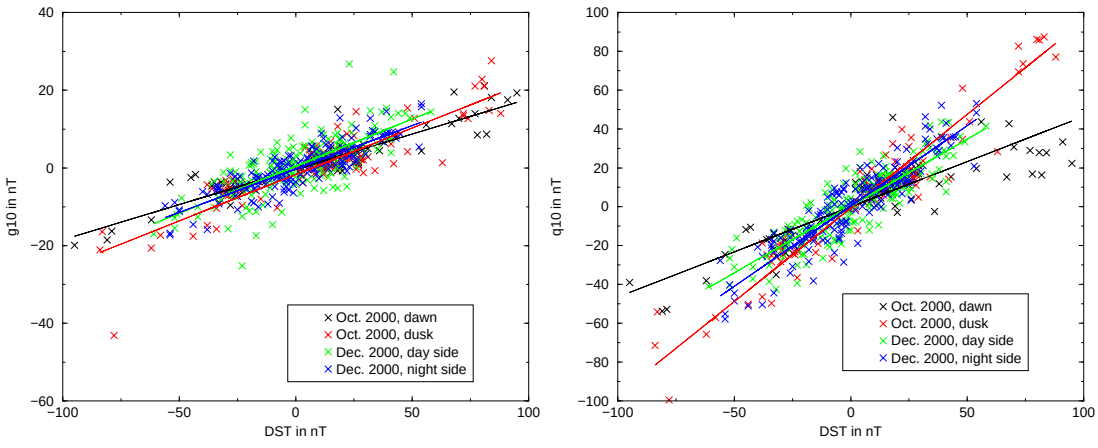

Figure 5.4: Correlation results for the two weeks periods in October/December 2000: D_{ST} against $\tilde{g}_1^0$ (left panel), D_{ST} against $\tilde{q}_1^0$ (right panel).

5.1.2 'Model 2' for all LT zones

In order to cover a wider range of local time zones, data from a period of 150 days from June to December 2002 are investigated. Due to two orbit manoeuvres (the first one on June 10 and 11, 2002 and the second one on December 9, 2002) the condition of CHAMP flying in resonance with the Earth lasted for the whole period. During this time the repeat cycle was two days long.
The same model, as explained in Section 5.1.1, using vector data for tracks from 40° to 140° geomagnetic colatitude is computed. Now, each inversion is done for a period of eleven days. Every five days a 'new' inversion is started. This gives a good LT coverage. During the 150 days a set of coefficients for all local time zones (about every 30 minutes) is calculated.

Figure 5.5 shows one example for July 2002 when CHAMP was flying in the 0800/2000 LT orbit. In both panels larger wiggles are seen which are difficult to model, although the trend is modelled quite well. More examples can be found in Appendix A.

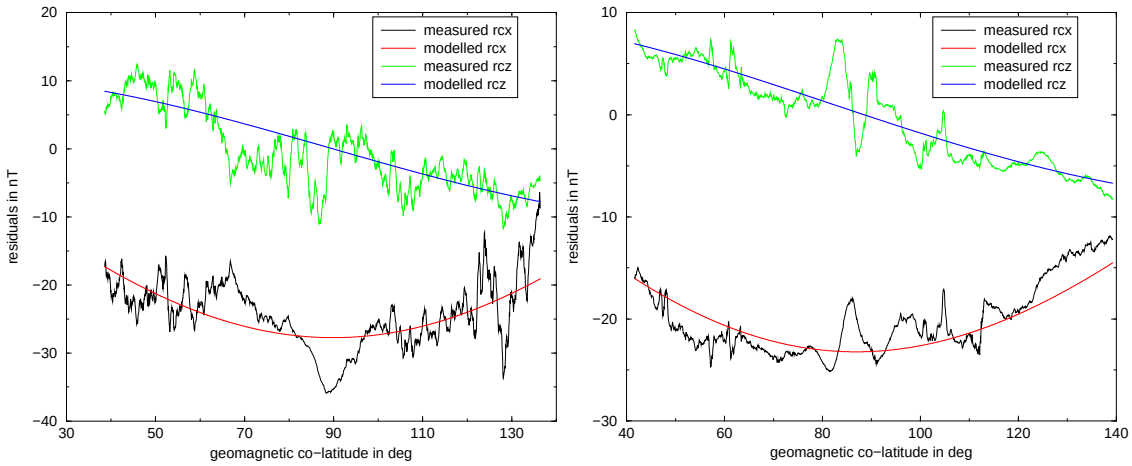

Figure 5.5: 13th and 15th of July 2002, 0759 LT (left panel) and 2000 LT (right panel).

5.1.3 Correlations with D_{ST}

Again a quality check of **'model 2'** for all LT zones is done for the calculated vector data during the 150 days period in 2002. Figure 5.6 shows the inversion results. A

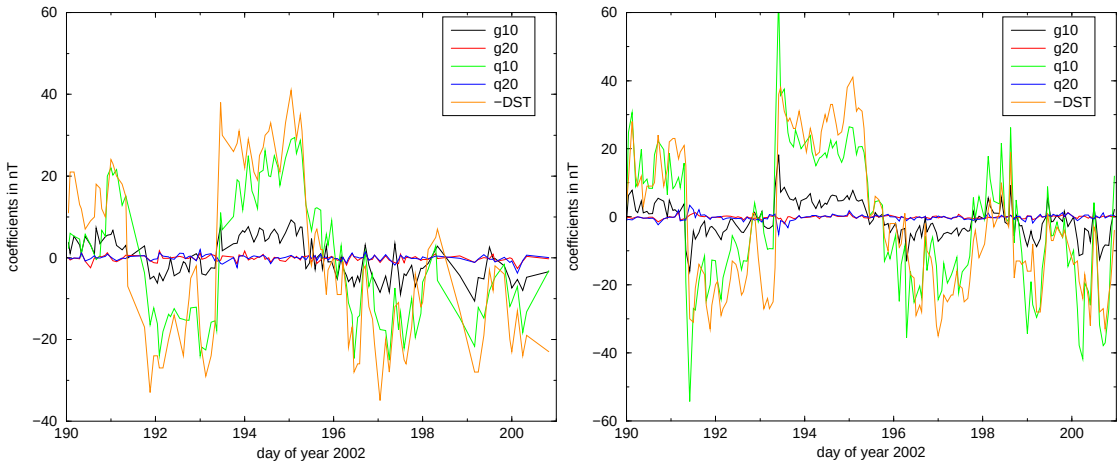

Figure 5.6: Inversion result of 11 days of data in July 2002, 0800 LT (left panel) and 2000 LT (right panel). The resulting coefficients ($\tilde{g}_1^0$ (black line), $\tilde{g}_2^0$ (red line), $\tilde{q}_1^0$ (green line), $\tilde{q}_2^0$ (blue line)) are compared with D_{ST} (orange line).

period of 11 days in July 2002 is chosen. The four coefficients ($\tilde{g}_1^0$, $\tilde{g}_2^0$, $\tilde{q}_1^0$ and $\tilde{q}_2^0$) are compared with the D_{ST}-index. Figure 5.6 demonstrates the good agreement of $\tilde{q}_1^0$ and D_{ST} for the 0800 LT track (left panel) and for the 2000 LT track (right panel). For each LT hour the linear regression between $\tilde{g}_1^0$ with D_{ST} and $\tilde{q}_1^0$ with D_{ST} is calculated. While only the $\tilde{g}_1^0$ and $\tilde{q}_1^0$ coefficients are significant Figure 5.7 shows the correlation results for all calculated local times for these coefficients.

The statistical results of each linear regression between D_{ST} and the two significant Gauss coefficients $\tilde{g}_1^0$ and $\tilde{q}_1^0$ and the linear regression between $\tilde{q}_1^0$ and $\tilde{g}_1^0$ are summarised in Tab. 5.2. Good correlation coefficients are obtained for the linear regression between D_{ST} and $\tilde{q}_1^0$ ($> 83\%$).

5.1.4 Conclusion of 'model 2' using tracks

The slope of all statistical results from **'model 1'** and from **'model 2'** are compiled in Figure 5.8. The four local time zones for the inversion of scalar data in 2000 (green squares and blue diamonds) are reproduced by the inversion using vector

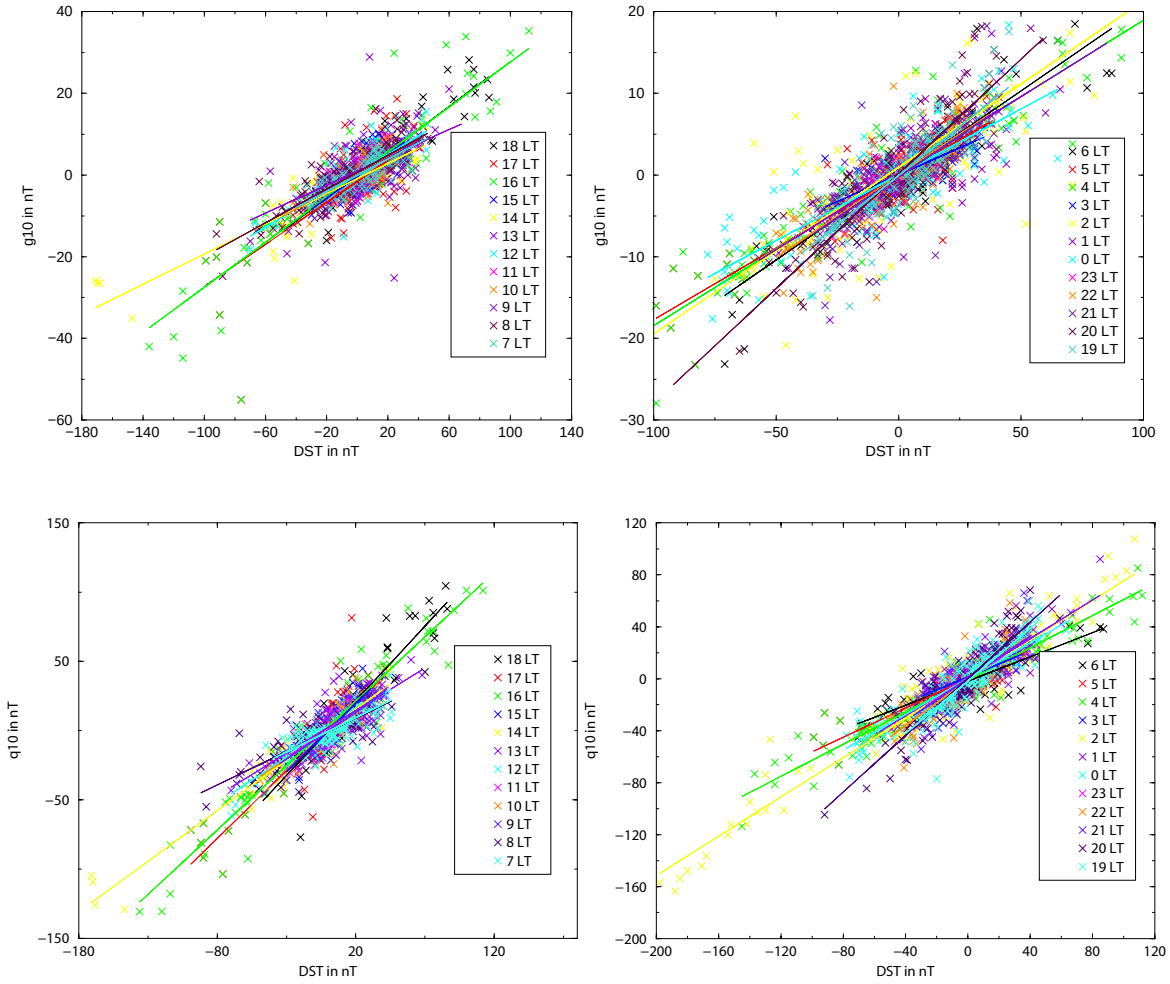

Figure 5.7: Top: Correlations between D_{ST} and $\tilde{g}_1^0$ for all local time zones for June to December 2002. Bottom: Correlations between D_{ST} and $\tilde{q}_1^0$ for all local time zones. The 'day side' from 7 LT to 18 LT is illustrated in the left panel and the 'night side' from 19 LT to 6 LT in the right panel.

Correlation Coefficient							
	D_{ST} vs $\tilde{g}_1^0$	D_{ST} vs $\tilde{q}_1^0$	$\tilde{q}_1^0$ vs $\tilde{g}_1^0$		D_{ST} vs $\tilde{g}_1^0$	D_{ST} vs $\tilde{q}_1^0$	$\tilde{q}_1^0$ vs $\tilde{g}_1^0$
19 LT	0.83	0.90	0.95	07 LT	0.86	0.83	0.86
20 LT	0.89	0.93	0.97	08 LT	0.87	0.82	0.82
21 LT	0.81	0.87	0.97	09 LT	0.88	0.90	0.82
22 LT	0.83	0.87	0.95	10 LT	0.75	0.83	0.58
23 LT	0.77	0.83	0.86	11 LT	0.63	0.77	0.49
00 LT	0.82	0.89	0.96	12 LT	0.77	0.87	0.87
01 LT	0.77	0.88	0.95	13 LT	0.55	0.82	0.81
02 LT	0.90	0.95	0.97	14 LT	0.90	0.97	0.94
03 LT	0.71	0.83	0.92	15 LT	0.70	0.86	0.79
04 LT	0.94	0.95	0.94	16 LT	0.89	0.96	0.93
05 LT	0.88	0.90	0.96	17 LT	0.74	0.89	0.73
06 LT	0.91	0.85	0.88	18 LT	0.88	0.92	0.95
Slope							
	D_{ST} vs $\tilde{g}_1^0$	D_{ST} vs $\tilde{q}_1^0$	$\tilde{q}_1^0$ vs $\tilde{g}_1^0$		D_{ST} vs $\tilde{g}_1^0$	D_{ST} vs $\tilde{q}_1^0$	$\tilde{q}_1^0$ vs $\tilde{g}_1^0$
19 LT	0.24	1.01	0.24	07 LT	0.20	0.49	0.33
20 LT	0.28	1.09	0.26	08 LT	0.21	0.48	0.33
21 LT	0.20	0.82	0.26	09 LT	0.20	0.67	0.26
22 LT	0.20	0.88	0.23	10 LT	0.21	0.66	0.21
23 LT	0.20	0.77	0.24	11 LT	0.20	0.65	0.19
00 LT	0.16	0.69	0.24	12 LT	0.22	0.65	0.34
01 LT	0.19	0.74	0.27	13 LT	0.17	0.61	0.33
02 LT	0.20	0.76	0.28	14 LT	0.18	0.73	0.25
03 LT	0.13	0.50	0.28	15 LT	0.27	0.99	0.26
04 LT	0.19	0.62	0.29	16 LT	0.28	0.93	0.30
05 LT	0.18	0.56	0.31	17 LT	0.26	0.98	0.23
06 LT	0.21	0.47	0.37	18 LT	0.28	1.08	0.26

Table 5.2: Statistical results of the comparison between the two Gauss coefficients $\tilde{g}_1^0$ and $\tilde{q}_1^0$ and D_{ST} for all local times calculated from vector data using tracks from 40° to 140° colatitude. The complete table can be found in Appendix A (Tab. A.1).

data in 2002 (black crosses and red stars).
The comparison with literature values [Langel et al., 1996], [Olsen, 2002] shows the same result as already presented in Section 4.5. The fit produced from only 4 values (Fig. 4.10) can be reproduced. The value of 0.7 used by Olsen [2002] for local times from 1900 to 0700 LT corresponds approximately to the mean value of this study.

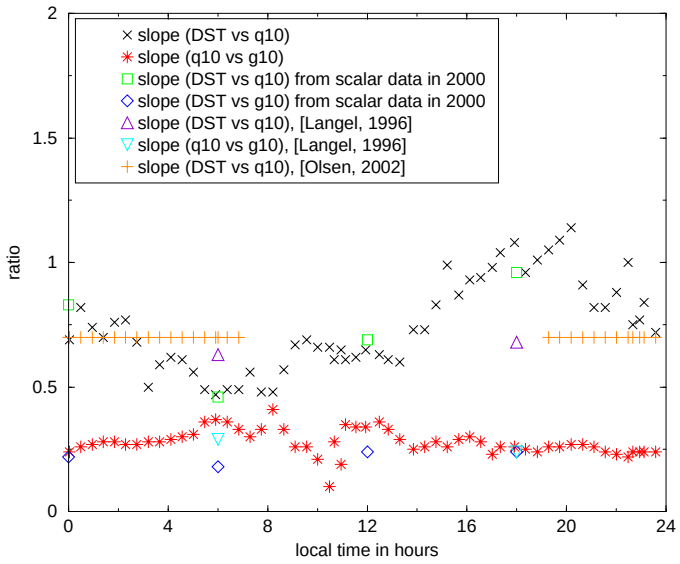

Figure 5.8: Local time dependence for each hour calculated from vector data of 150 days period in 2002.

To find a better description for the local time dependence of the ratio between D_{ST} and $\tilde{q}_1^0$ and the ratio of $\tilde{q}_1^0$ to $\tilde{g}_1^0$ a harmonic fit is done for all LT zones:

$$s = \begin{pmatrix} a_1 \\ b_1 \\ a_2 \\ b_2 \\ c \end{pmatrix} \cdot \begin{pmatrix} \cos(15° \cdot t) \\ \sin(15° \cdot t) \\ \cos(30° \cdot t) \\ \sin(30° \cdot t) \\ 1 \end{pmatrix} = \begin{pmatrix} A_1 \\ A_2 \\ c \end{pmatrix} \cdot \begin{pmatrix} \sin(15° \cdot t + \omega_1) \\ \sin(30° \cdot t + \omega_2) \\ 1 \end{pmatrix} \tag{5.9}$$

with t as hour of local time and a Amplitude $A_i = \sqrt{a_i^2 + b_i^2}$ and a phase of $\omega_i = \arctan \frac{a_i}{b_i}$ can be found. First, the fundamental mode is investigated only, then the first harmonic is included in the regression. Figure 5.9 illustrates the resulting fits. It can be seen that the fundamental mode already describes the slope quite well, but it can be improved by including the first harmonic.

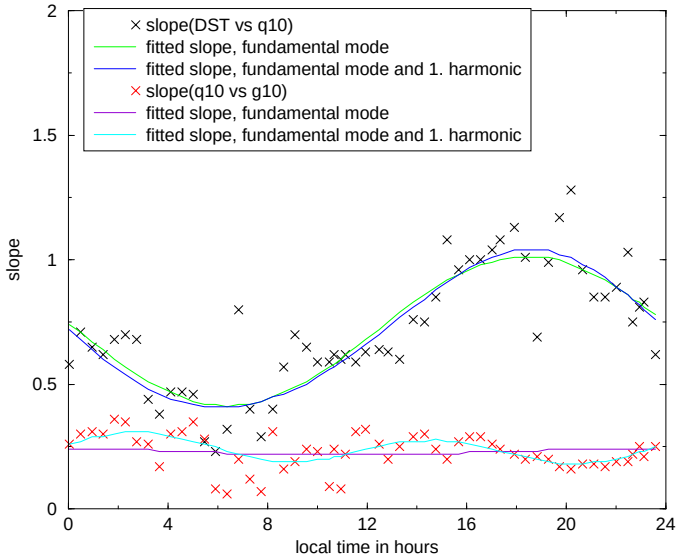

Figure 5.9: LT dependence for inverting 11 days each 5 days over a period of 150 days in June to December 2002, using tracks.

From Equation 5.9 the result of the linear regression between D_{ST} and $\tilde{q}_1^0$ can be expressed as

$$\begin{aligned} s(\tilde{q}_1^0/D_{ST}) = 0.7079 \quad &- \quad 0.3148\sin(15^\circ \cdot t) + 0.0298\cos(15^\circ \cdot t) \\ &- \quad 0.013\sin(30^\circ \cdot t) - 0.0159\cos(30^\circ \cdot t) \end{aligned} \tag{5.10}$$

In a more obvious way, this equation can be rewritten as

$$\begin{aligned} s(\tilde{q}_1^0/D_{ST}) = 0.71 \quad &+ \quad 0.32\sin(15^\circ \cdot t + 15^\circ \cdot 11.6) \\ &+ \quad 0.02\sin(30^\circ \cdot t - 30^\circ \cdot 4.3). \end{aligned} \tag{5.11}$$

From these equations it can be seen that the function which describe the ratio between $\tilde{q}_1^0$ and D_{ST} has a phase shift of about 12 hours (compare Fig. 5.9).

The ratio between $\tilde{g}_1^0$ and $\tilde{q}_1^0$ has the following form:

$$\begin{aligned} s(\tilde{g}_1^0/\tilde{q}_1^0) &= 0.2386 + 0.0135\sin(15^\circ \cdot t) + 0.01\cos(15^\circ \cdot t) \\ &\quad +0.0522\sin(30^\circ \cdot t) + 0.0097\cos(30^\circ \cdot t) \\ &= 0.24 + 0.02\sin(15^\circ \cdot t + 15^\circ \cdot 2.4) \\ &\quad +0.05\sin(30^\circ \cdot t + 30^\circ \cdot 0.35). \end{aligned} \tag{5.12}$$

5.2 Modelling orbits

To further improve **'model 2'** the inversion is expanded to whole orbits. This has not been done before. Especially in main field modelling, vector data are only used for latitudes of ±50° around the equator and scalar data for poleward regions (e. g., in CO2 main field model [Holme et al., 2003]). Another attempt is the reduction of the misfit at the poles (Fig. 4.12). Therefore full orbits are going to be modelled after a pole correction at ±20° around the poles is applied. Another extension is the order 1 term in Equation 5.1 and 5.2. Now the full set of coefficients up to degree 2 and order 1 is used.

5.2.1 Transformation

One problem of using vector data in polar regions is caused by the transformation from geocentric to geomagnetic coordinates and components when employing the fairly simple approach given in Kertz ([Kertz, 1989], Eq.(8.10)). The transformation of scalar or vector data for tracks from 40° to 140° colatitude works well, while the Equations 4.8 to 4.10 are not unique around the poles. An alternative transformation between geocentric and geomagnetic systems based on Cartesian coordinates is introduced. The transformations of the coordinates and the field components can both be performed by a rotation about the z-axis.
First, the spherical coordinates have to be expressed in Cartesian coordinates. At one point on a unit sphere, which has its origin in the origin of the geocentric coordinate system (compare Fig. 2.7), their relation is as follows, e. g., from [Bronstein & Semendjajew, 1989]:

$$\begin{pmatrix} z \\ x \\ y \end{pmatrix} = \begin{pmatrix} \cos\theta \\ \sin\theta\cos\phi \\ \sin\theta\sin\phi \end{pmatrix}. \tag{5.13}$$

Hence, for the transformation between the two coordinate systems (geocentric coordinates, x, y and z, and geomagnetic coordinates, x^*, y^* and z^*), the position of the geomagnetic North pole has to be known. It can be found with the help of a reference model like the IGRF2000 (as already done in Section 4.2).
The transformation matrix

$$\underline{\underline{A}} = \begin{pmatrix} \cos\theta_b \cos\phi_b & \cos\theta_b \sin\phi_b & -\sin\theta_b \\ -\sin\phi_b & \cos\phi_b & 0 \\ \sin\theta_b \cos\phi_b & \sin\theta_b \sin\phi_b & \cos\theta_b \end{pmatrix} \tag{5.14}$$

allows to compute the geomagnetic colatitude, θ^* and longitude, ϕ^* for each position. Then, the matrix, $\underline{\underline{A}}$ is used to calculated the 'geomagnetic, Cartesian' coordinates

$$\begin{pmatrix} x^* \\ y^* \\ z^* \end{pmatrix} = \underline{\underline{A}} \cdot \begin{pmatrix} x \\ y \\ z \end{pmatrix} \tag{5.15}$$

from which the geomagnetic colatitude θ^* and longitude ϕ^* then can be evaluated:

$$\theta^* = \arctan \frac{\sqrt{(x^*)^2 + (y^*)^2}}{z^*} \tag{5.16}$$

$$\phi^* = \arctan \frac{y^*}{x^*}. \tag{5.17}$$

The same transformation matrix can be used to rotate the field values from the geocentric into the geomagnetic system. First, the Cartesian field components (B_x, B_y, B_z) have to be computed from the spherical field components (B_r, B_θ, B_ϕ):

$$B_x = B_\theta \cos\theta \cos\phi - B_\phi \sin\phi \tag{5.18}$$

$$B_y = B_\theta \cos\theta \sin\phi + B_\phi \cos\phi \tag{5.19}$$

$$B_z = -B_\theta \sin\theta. \tag{5.20}$$

Then, with the help of the transformation matrix $\underline{\underline{A}}$ the field components can be computed in the geomagnetic system:

$$\begin{pmatrix} B_x^* \\ B_y^* \\ B_z^* \end{pmatrix} = \underline{\underline{A}} \cdot \begin{pmatrix} B_x \\ B_y \\ B_z \end{pmatrix} \tag{5.21}$$

From the resulting field components (B_x^*, B_y^*, B_z^*) the spherical components (B_r^*, B_θ^*, B_ϕ^*) are obtained:

$$B_r^* = (B_x^* \cos\phi^* + B_y^* \sin\phi^*) \sin\theta^* + B_z^* \cos\theta^* \tag{5.22}$$

$$B^*_\theta = (B^*_x \cos\phi^* + B^*_y \sin\phi^*) \cos\theta^* - B^*_z \sin\theta^* \tag{5.23}$$

$$B^*_\phi = B^*_y \cos\phi^* - B^*_x \sin\phi^*. \tag{5.24}$$

These spherical, geomagnetic field components (B^*_r, B^*_θ, B^*_ϕ) and the geomagnetic coordinates (θ^*, ϕ^*) are used in the following calculations.

5.2.2 Pole correction

Before the inversion of the signal for whole orbits can start a correction is applied for non-scalar potential fields caused by several currents at the poles, like field aligned currents or Pedersen currents, which are disturbing the measurements. The cross-polar cap ionospheric currents connecting the dawn and dusk or the day side and night side Region 1 FACs. Around the North and South pole a correction using Ampere's law is applied, as suggested by Stauning & Primdahl [2000].

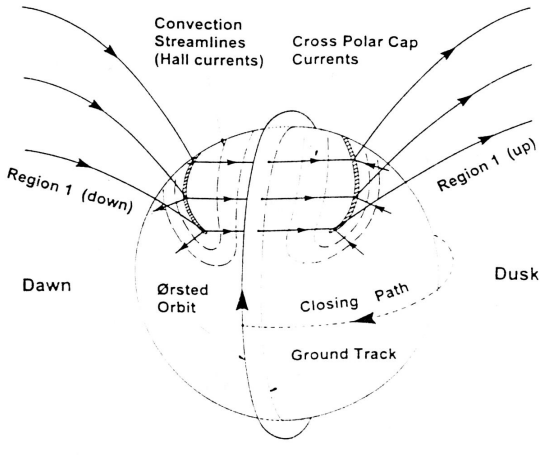

Figure 5.10: Illustrated is the situation of a satellite flying in the noon/midnight orbit, crossing polar currents, from [Stauning & Primdahl, 2000].

Therefore stationary conditions are assumed (e. g., the orbit is exactly closed). Then the total current I_S which is flowing through the surface spanned by the closed contour L (= satellite orbit, with differential element **dl**) can be expressed as:

$$I_S = \mu_0^{-1} \int_L \mathbf{B} \cdot \mathbf{dl}. \tag{5.25}$$

where **B** is the measured magnetic field vector. The correction is applied at latitudes of ±20° around the poles. Each orbit starts at the equator when CHAMP is flying northward. $\mathbf{B} \cdot \mathbf{dl}$ is the dot product of the magnetic perturbation vector and the velocity vector multiplied by the sample interval. Its unit is nT · km and the value of the along-track component (B_1) at the first point and the sum along the orbit (B_2) at the last point is necessary for the correction factor (K_{corr} in nT):

$$K_{corr} = \frac{B_2 - B_1}{2\pi(r + \frac{alt_1 + alt_2}{2})}, \tag{5.26}$$

with the Earth's radius r and $alt_{1/2}$ as altitude at the first (alt_1) and last point (alt_2). Then, the differences of the residuals of the North component, X, in the spacecraft (SC) coordinate system (SC = FGM1 in Fig. 2.6, see Eq. 5.28 and following) is corrected in the latitude range from 70° to 90°, respectively from −70° to −90°:

$$rcx' = rcx - K_{corr}. \tag{5.27}$$

The transformation from the NEC coordinate system into the spacecraft (SC) system is a rotation about the z-axis. The transformation matrix is:

$$R_z(\gamma) = \begin{pmatrix} 1 & 0 & 0 \\ 0 & \cos\gamma & \sin\gamma \\ 0 & -\sin\gamma & \cos\gamma \end{pmatrix} \tag{5.28}$$

where γ is the rotation angle which depends on the flight direction and the position of the satellite. If CHAMP is flying northward, the rotation angle can be calculated (with inclination $\omega = 87.3°$ and colatitude θ) as:

$$\gamma = \arcsin\left(\frac{\cos\omega}{\cos(90° - \theta)}\right) \tag{5.29}$$

or, if CHAMP is flying southward, as:

$$\gamma = 180° - \arcsin\left(\frac{\cos\omega}{\cos(90° - \theta)}\right). \tag{5.30}$$

The (back) transformation between the NEC system and the SC system then can be done as follows:

$$NEC = R_z(-\gamma) \cdot SC \qquad \text{and} \qquad SC = R_z(\gamma) \cdot NEC. \tag{5.31}$$

5.2.3 'Model 2' results for orbits

The following Figure (Fig. 5.11) shows the results which are obtained from **'model 2'** using CHAMP vector data for whole orbits. In principle the procedure is the same as **'model 2'** using tracks (Sec. 5.1). First, the inversion is (twice) done for n=1 and m=0, followed by a 2σ-throwout. Afterwards the complete inversion is done. Additionally, the results are achieved after the transformation into magnetic coordinates (explained in Sec. 5.2.1) and the current correction for $\pm 20°$ around the poles (explained in Sec. 5.2.2) is applied. For the inversion each orbit starts at the North pole.

In Figure 5.11 (top panel) one whole orbit is plotted over time. The satellite starts at a colatitude of 2.75° flying southward, reaching the South pole after about 2700 seconds, flying up to the North pole again. The satellite crosses the geomagnetic equator on the night side (Fig. 5.11, bottom, left panel) at 0320 LT at a longitude of 96.58° and on the day side (Fig. 5.11, bottom, right panel) at 1520 LT and a longitude of $-95.08°$. The night side half-orbit is less influenced by local currents but it is still very much influenced by currents at high latitudes. The day side path is more disturbed in general. E. g., at the geomagnetic equator the equatorial electrojet can be seen in the X-component.

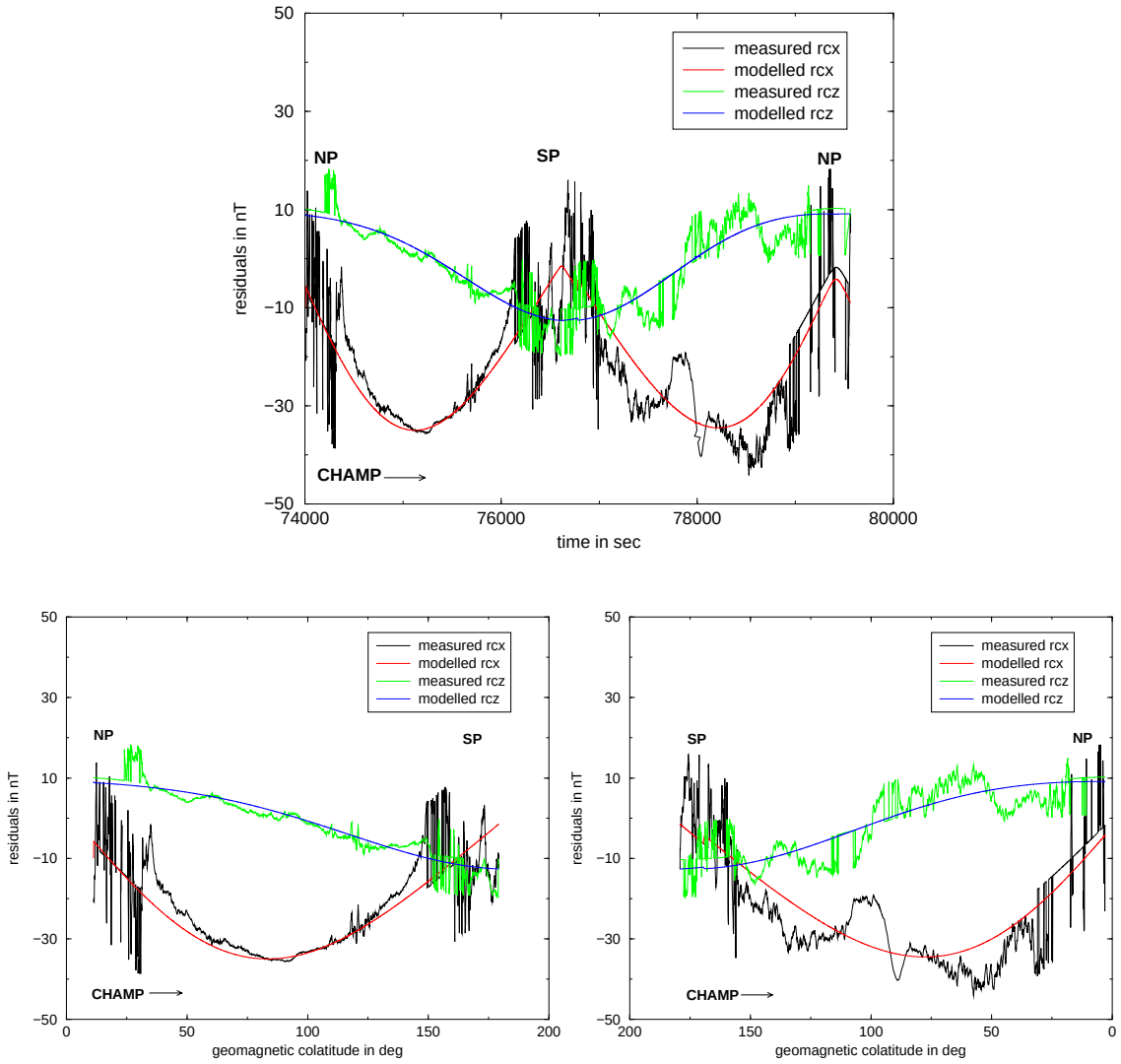

Figure 5.11: 4/6 September 2002: Modelling full orbits using vector data after applying Ampere's law. The satellite is flying in a 0300/1500 LT orbit. The orbit is starting at the North pole. Bottom: The two half-orbits are shown separately. The left panel shows the half-orbit which is crossing the equator at 0322 LT. The second half-orbit covers the day side with the equator crossing at 1522 LT (right panel).

5.2.4 Correlations with D_{ST}

Again, the obtained Gauss coefficients ($\tilde{g}_1^0$, $\tilde{g}_1^1$, $\tilde{g}_2^0$, $\tilde{g}_2^1$, $\tilde{q}_1^0$, $\tilde{q}_1^1$, $\tilde{q}_2^0$ and $\tilde{q}_2^1$) are compared with the D_{ST}-index. Figure 5.12 shows a very good correlation between $\tilde{q}_1^0$ and D_{ST}. The $\tilde{g}_1^0$ coefficient shows some similarity but with a lower amplitude. For all other coefficients no significant dependence can be seen.

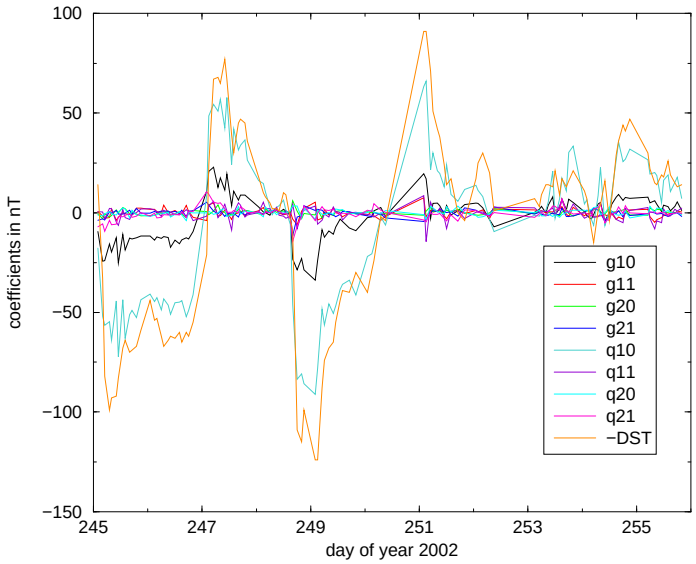

Figure 5.12: Comparison of Gauss coefficients with D_{ST} using vector data and modelling full orbits: All calculated coefficients are shown, $\tilde{g}_1^0$ (black line), $\tilde{g}_1^1$ (red line), $\tilde{g}_2^0$ (green line), $\tilde{g}_2^1$ (blue line), $\tilde{q}_1^0$ (yellow line), $\tilde{q}_1^1$ (violet line), $\tilde{q}_2^0$ (cyan line) and $\tilde{q}_2^1$ (magenta line) compared to D_{ST} (orange line).

Looking at the linear regression between the obtained Gauss coefficients and D_{ST} and between $\tilde{g}_1^0$ and $\tilde{q}_1^0$ in more detail reveals that only the degree 1, order 0 terms ($\tilde{g}_1^0$ and $\tilde{q}_1^0$) with each other and with D_{ST} correlate well. There is no correlation visible for the other coefficients with D_{ST}. Their correlation coefficients are below ± 0.5.

Some very interesting aspects can be found on a closer look at the slope of the correlation results (Fig. 5.14). Most slopes are not significant. The correlation coefficients already showed that only the correlation for D_{ST} with $\tilde{q}_1^0$ and $\tilde{q}_1^0$ with $\tilde{g}_1^0$ are reasonably high.

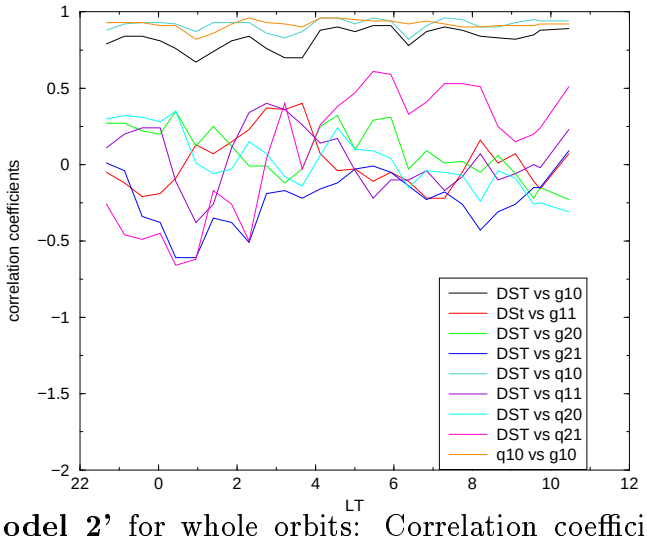

Figure 5.13: 'Model 2' for whole orbits: Correlation coefficients for 150 days period from June to December 2002.

The statistical results are summarised in Table A.3. It shows the correlation coefficients, the slopes and the intercepts for all calculated LT zones modelling whole orbits. Because of good correlations (seen in Fig. 5.13), the results for D_{ST} versus $\tilde{g}_1^0$, $\tilde{q}_1^0$ and $\tilde{q}_1^0$ versus $\tilde{g}_1^0$ are listed in Table A.3. Motivated by induction studies it is also looked into the result of the linear regression of D_{ST} versus $\tilde{q}_2^1$.

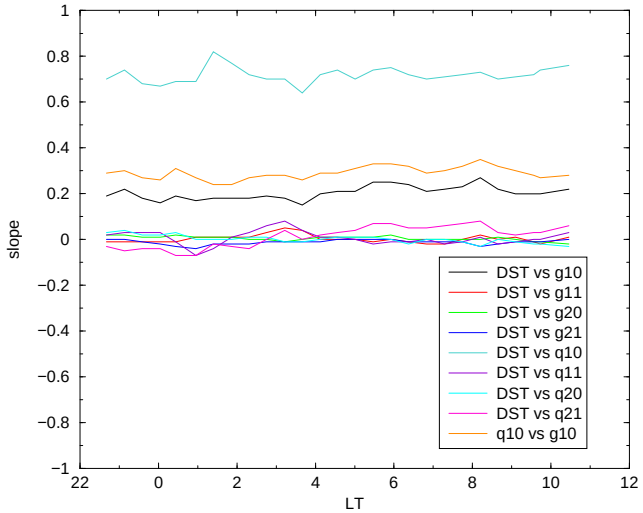

Figure 5.14: 'Model 2' for whole orbits: Slope of regression for all coefficients compared to DST for a 150 days period from June to December 2002.

5.3 Interpretation

The choice using repeat tracks in the beginning removes a lot of problems and greatly simplifies the calculations. But for the interpretation several points have to be explained and have to be taken into account. A closer look is taken on the $\tilde{q}_1^0$, the $\tilde{g}_1^0$ and the $\tilde{q}_2^1$ coefficients. As already said, for $\tilde{g}_1^0$ and $\tilde{q}_1^0$ this is motivated by the good correlations with each other and with D_{ST}.

Figures 5.15 and 5.16 show the slopes of these two coefficients. As expected, no LT dependence can be seen. The LT dependence found in **'model 2'** using tracks from 40° to 140° colatitude is cancelled by averaging over the 'day side' and 'night side' when full orbits are used. The slope of the linear regression between D_{ST} and $\tilde{q}_1^0$ (Fig. 5.15) can be fitted by the constant mean value of 0.72 for all local times.

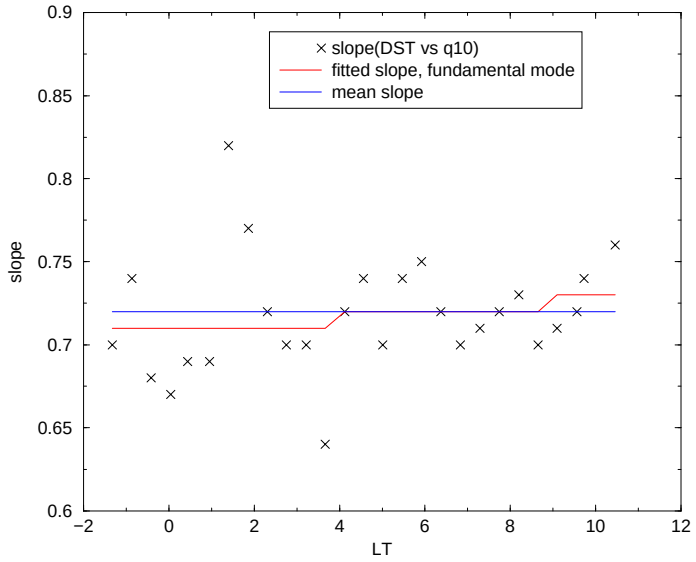

Figure 5.15: Slope of the linear regression of D_{ST} against $\tilde{q}_1^0$ plotted over local time. The fit of the dominant mode (red line) is quite close to the mean value (blue line) of the slope.

Figure 5.16 shows the relation between $\tilde{q}_1^0$ and $\tilde{g}_1^0$. In principle the same can be found. There is no clear LT dependence. The $\tilde{g}_1^0$ coefficient can be described as $0.29 \cdot \tilde{q}_1^0$. The amplitude of a possible dominant mode

$$s(\tilde{g}_1^0/\tilde{q}_1^0) = 0.28 + 0.02sin(15° \cdot t - 15° \cdot 2.4) \tag{5.32}$$

with t as the hour in local time, is small.

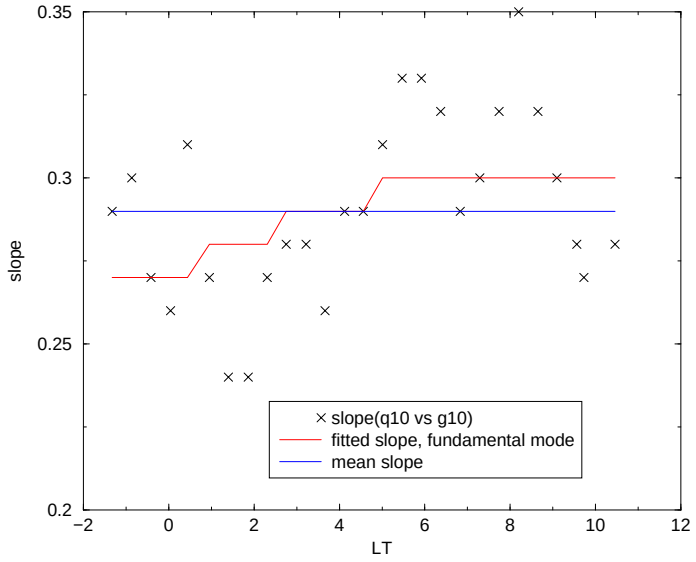

Figure 5.16: Slope of the linear regression of $\tilde{q}_1^0$ against $\tilde{g}_1^0$ plotted over local time.

There is no justification from the correlations for an detailed look into the $\tilde{q}_2^1$ coefficient. And no LT dependence in the $\tilde{q}_1^0$ term can be seen, but possibly the difference in the results of **'model 2'** using tracks and using orbits can be explained by the quadrupole term ($\tilde{q}_2^1$).

Figure 5.17 illustrates the slope of the linear regression between D_{ST} and $\tilde{q}_2^1$. On an enlarged scale the slope shows some systematic LT dependence.
The fit which describes the relation between the $\tilde{q}_2^1$ coefficient and the D_{ST}-index can be expressed in geomagnetic coordinates as:

$$s(\tilde{q}_2^1/D_{ST}) = 0.059 \sin(15^\circ \cdot t - 15^\circ \cdot 2.8) \tag{5.33}$$

where t is the hour in local time.

Up to now, the azimuthal angle, ϕ, was always chosen to have its origin in the orbital plane. For a better interpretation of the results the dependence on the longitude has to be implemented. Therefore the result is transformed into a geomagnetic, local time frame. In this frame λ is the longitude and 0000 LT is defined as its origin.

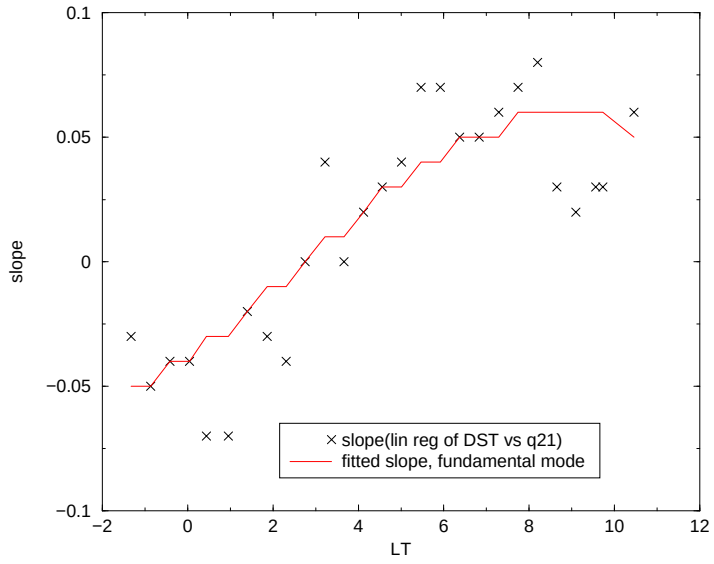

Figure 5.17: Slope of the linear regression between D_{ST} and $\tilde{q}_2^1$ plotted over local time. The red line represents a dominant mode fit.

The variable part of the ring current magnetic field may thus be described in this system by the coefficients:

$$\hat{q}_1^0 = -0.72 \cdot D_{ST}, \qquad \hat{q}_2^1 = -0.04 \cdot D_{ST} \qquad \text{and} \qquad \hat{s}_2^1 = 0.044 \cdot D_{ST}. \quad (5.34)$$

For a complete description the constant part of the magnetic field caused by external currents has to be determined, too. Therefore the same calculations (**'model 2'** using orbits) are done for the residuals, obtained as the measured data minus the CO2 main field model. The difference between the ***repeat track*** is no longer calculated. This is done for the 0200/1400 LT orbit and the perpendicular orbit at 0800/2000 LT over a period of 11 quiet days.

Table 5.3 lists the obtained results of the linear regression of **'model 2'** from residuals (but no differences between ***repeat tracks***) using whole orbits for 0232 LT and 0914 LT. Again, good correlations can be seen for $\tilde{g}_1^0$ and $\tilde{q}_1^0$ with each other and with D_{ST}.

Correlation Coefficient				
	D_{ST} vs $\tilde{g}_1^0$	D_{ST} vs $\tilde{q}_1^0$	$\tilde{q}_1^0$ vs $\tilde{g}_1^0$	D_{ST} vs $\tilde{q}_2^1$
0232 LT	0.64	0.82	0.80	0.12
0914 LT	0.81	0.89	0.83	0.19
Slope				
	D_{ST} vs $\tilde{g}_1^0$	D_{ST} vs $\tilde{q}_1^0$	$\tilde{q}_1^0$ vs $\tilde{g}_1^0$	D_{ST} vs $\tilde{q}_2^1$
0232 LT	0.19	0.65	0.30	0.01
0914 LT	0.23	0.65	0.32	0.03
Intercept				
	D_{ST} vs $\tilde{g}_1^0$	D_{ST} vs $\tilde{q}_1^0$	$\tilde{q}_1^0$ vs $\tilde{g}_1^0$	D_{ST} vs $\tilde{q}_2^1$
0232 LT	-1.41	22.04	-8.06	-0.25
0914 LT	-0.33	18.78	-6.36	1.83

Table 5.3: Statistical results of the comparison between the three Gauss coefficients $\tilde{g}_1^0$, $\tilde{q}_1^0$, $\tilde{q}_2^1$ and D_{ST} for the two local times calculated from vector data residuals (no difference between repeat tracks) using whole orbits.

In this case the correlation with the D_{ST}-index is not so important. Intervals with little variation were selected, in July and September 2002, to obtain a stable bias value. The mean values resulting from the calculations for these two LT-intervals give an indication for the constant part of the ring current. They are combined in the following Table 5.4:

	0232 LT	**0914 LT**	**mean**
$\overline{D}_{ST}$	12.49 nT	-1.55 nT	5.47 nT
$\overline{\tilde{q}_1^0}$	17.76 nT	30.16 nT	
$\overline{\tilde{q}_1^0} + 0.72 \cdot \overline{D}_{ST}$	26.75 nT	29.04 nT	**27.90 nT**
$\overline{\tilde{q}_2^1}$	-0.13 nT	1.79 nT	

Table 5.4: Resulting mean values of the constant part obtained for the two calculated local time periods.

From these results the $\tilde{q}_1^0$ coefficient in the geomagnetic, local time frame can be written as:

$$\hat{q}_1^0 = 27.9 - 0.72 D_{ST}. \tag{5.35}$$

As expected, the $\tilde{q}_2^1$ coefficient is close to zero around 0200 LT and significantly larger at around 0900 LT. The correction has to be expanded to the n=2, m=1 terms. However, the correlation of $\tilde{q}_2^1$ with D_{ST} is not significant, the constant part of $\hat{q}_2^1$ and $\hat{s}_2^1$ will therefore be deduced from the already obtained results of the ***repeat tracks*** (Eq. 5.33). The ratio between the amplitude $\tilde{q}_2^1 = 0.059$ and the variable part of the ring current $\tilde{q}_1^0 / D_{ST} = 0.72$ has the value of 0.082. This ratio gives a mean amplitude of $\tilde{q}_2^1$ of 2.29 nT. Altogether, the constant part of the external currents can thus be described by the following coefficients:

$$\hat{q}_1^0 = 27.9nT, \qquad \hat{q}_2^1 = 1.55nT \qquad \text{and} \qquad \hat{s}_2^1 = -1.69nT. \tag{5.36}$$

Chapter 6

Improved model of the 'ring current'

To find the best possible model of the 'ring current' the different data sets used for **'model 2'** are compared with each other. An overview over the obtained outcome from **'model 2'** using tracks and orbits will be given. Moreover, a test calculation is performed to check the compatibility of the two models. Thereafter, it will be described, before a comparison with other field models is done.

6.1 Comparison of 'model 2' using tracks or whole orbits

First, the main differences for **'model 2'** using tracks from 40° to 140° colatitude and **'model 2'** using full orbits are compared. They are obtained from the statistics of the linear regression between the Gauss coefficients and the D_{ST}-index.

Tracks:

- Significant correlations can be found between the symmetric part of the ring current, $\tilde{q}_1^0$ and the D_{ST}-index and between the induced internal part, $\tilde{g}_1^0$ and $\tilde{q}_1^0$.
- The two coefficients $\tilde{q}_1^0$ and $\tilde{g}_1^0$ (compare Figure 5.9) show a clear local time dependence.
- Minimum and maximum amplitudes can be found for $\tilde{q}_1^0$ and $\tilde{g}_1^0$:

- $\tilde{q}_1^0$: A minimum of the slope of about 0.5 at about 0700 LT and a maximum of about 1 at about 1800 LT can be seen.
- $\tilde{g}_1^0/q_1^0$ varies between about 0.2 and 0.3.

Orbits:

- The local time dependence of $\tilde{q}_1^0$ cannot be seen anymore. $\tilde{q}_1^0$ depends linearly on D_{ST} with a factor of 0.72.
- The slope of the linear regression between $\tilde{g}_1^0$ and $\tilde{q}_1^0$ shows only a small local time dependence. A reasonable fit can also be done by the mean value of 0.29.
- On an enlarged scale the $\tilde{q}_2^1$ shows a local time dependence. This quadrupole term has to be added to get a better correction for external currents.

The slope of the linear regression between each component and the D_{ST}-index can be described in general as:

$$s = \begin{pmatrix} a_1 \\ b_1 \\ a_2 \\ b_2 \\ c \end{pmatrix} \cdot \begin{pmatrix} \cos(15° \cdot t) \\ \sin(15° \cdot t) \\ \cos(30° \cdot t) \\ \sin(30° \cdot t) \\ 1 \end{pmatrix} = \begin{pmatrix} A_1 \\ A_2 \\ c \end{pmatrix} \cdot \begin{pmatrix} \sin(15° \cdot t + \omega_1) \\ \sin(30° \cdot t + \omega_2) \\ 1 \end{pmatrix} \tag{6.1}$$

with the amplitude $A_i = \sqrt{a_i^2 + b_i^2}$ and the phase $\omega_i = \arctan \frac{a_i}{b_i}$, if a harmonic analysis is done. In comparison, the obtained values for the different data sets (using tracks or full orbits) of **'model 2'** are summarised in Table 6.1.

The $\tilde{q}_1^0$-average of the LT dependence in the model using tracks of 0.71 is comparable to the mean value for $\tilde{q}_1^0$ of 0.72 in the model using orbits. The same is true for the ratio between $\tilde{g}_1^0$ and $\tilde{q}_1^0$. The value of 0.24 (using tracks) is close to 0.28 (using orbits). From these values a model for the external current system will be proposed in the following section.

While all these values are reasonable for the altitude of the satellite orbit, a normalisation to the reference sphere (= Earth's surface) has to be done before. During

	tracks:		**orbits:**		
	$\tilde{q}_1^0/D_{ST}$	$\tilde{g}_1^0/\tilde{q}_1^0$	$\tilde{q}_1^0/D_{ST}$	$\tilde{g}_1^0/\tilde{q}_1^0$	$\tilde{q}_2^1/D_{ST}$
c	-0.71	0.24	-0.72	0.28	0
a_1	-0.0298	0.01	-	-0.012	-0.04
b_1	0.3148	0.0135	-	0.017	0.044
a_2	0.0159	0.0097	-	-	-
b_2	0.013	0.0522	-	-	-
A_1	0.32	0.02	-	0.02	0.06
A_2	0.02	0.05	-	-	-
ω_1	-5.4°	36.5°	-	-36.3°	-42.6°
ω_2	50.7°	10.5°	-	-	-

Table 6.1: Obtained correction factors in comparison between the two model possibilities using **'model 2'**

the period in 2002 the mean altitude of CHAMP was a bit above $400km$. With $a = 6371.2km$ and $r = a + 400km$ the constant and the D_{ST} dependent part of the coefficients can be obtained, in a first approximation, by

$$q_1^0 = q_1^{0'} \cdot \frac{r}{a} \tag{6.2}$$

$$q_2^1 = q_2^{1'} \cdot \left(\frac{r}{a}\right)^2 \tag{6.3}$$

$$s_2^1 = s_2^{1'} \cdot \left(\frac{r}{a}\right)^2 \tag{6.4}$$

$$g_1^0 = g_1^{0'} \cdot \left(\frac{a}{r}\right)^3 \tag{6.5}$$

where the primed coefficients have to be determined. As result $\hat{q}_1^{0'} = 26.3nT$, $\hat{q}_2^{1'} = 1.4nT$ and $\hat{s}_2^{1'} = -1.5nT$ and for the D_{ST} dependent part $\hat{q}_1^{0'} = -0.68 \cdot D_{ST}$, $\hat{q}_2^{1'} = -0.035 \cdot D_{ST}$ and $\hat{s}_2^{1'} = 0.039 \cdot D_{ST}$ are received.

6.2 A test of model compatibility

One possibility to include the obtained results in main field modelling can be achieved from Equations 5.1 and 5.2. For the two components, X and Z, the variation of the external magnetic field can be described by:

$$\begin{aligned} rcx &= -\tilde{q}_1^0 \sin\Psi \\ &\quad +\tilde{q}_2^1\sqrt{3}(\cos^2\Psi - \sin^2\Psi)\cos\lambda \end{aligned} \tag{6.6}$$

$$\begin{aligned} rcz &= \tilde{q}_1^0 \cos\Psi \\ &\quad +2\cdot\tilde{q}_2^1\sqrt{3}\cos\Psi\sin\Psi\cos\lambda \end{aligned} \tag{6.7}$$

with Ψ ($=\Theta^*$) as the magnetic colatitude and λ the longitude in the geomagnetic-local time frame. Assuming CHAMP flying in the orbital plane of 0°/180° gives $\cos\lambda = 1$, if CHAMP is flying northward, and $\cos\lambda = -1$, if CHAMP is flying southward.

For the period from June to December 2002 the two important coefficients are set to $\tilde{q}_1^0 = 0.72$ and $\tilde{q}_2^1 = 0.059$ (more reasonable value from the model using tracks). As a test they are included in a calculation producing synthetic data for the difference of the residuals of the X- and Z-component (using Eq. 6.6 and 6.7). The synthetic values rcx and rcz are computed for a whole orbit. Thereafter, to reproduce the synthetic data, the obtained synthetic rcx and rcz are put into the usual inversion model (**'model 2'**) using tracks limited to colatitudes between 40° and 140°. Finally, the curves are extrapolated to the poles. The resulting synthetic data and the obtained model are plotted in Figure 6.1.

It can be seen that the modelled curve fits only close to the equator. The discrepancy increase to the poles. While the synthetic values are calculated for whole orbits, the modelled values were obtained from **'model 2'** using tracks and extrapolated to the poles.

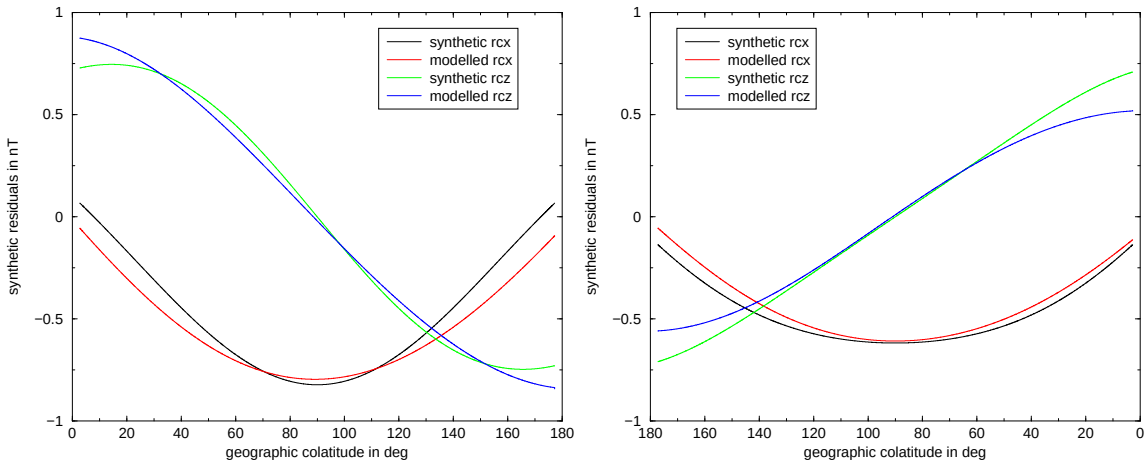

Figure 6.1: Synthetic values (calculated with $\tilde{q}_1^0 = 0.72$ and $\tilde{q}_2^1 = 0.059$) for the X- and Z-component of the external field variation in the second half of 2002 (rcx: black line, rcz: green line) on the night side (left panel) and day side (right panel).

After the inversion the values for the $\tilde{q}_1^0$ coefficient show a local time dependence with 0.84 on the night side and 0.62 on the day side, which is not fully comparable with the minimum and maximum value obtained from **'model 2'** using tracks (compare Figure 5.9).

To obtain model values for $\tilde{q}_1^0$ which are of similar amplitude to the obtained coefficient in **'model 2'** using tracks (Fig. 5.9), a synthetic model is calculated for $\tilde{q}_1^0 = 0.72$ and $\tilde{q}_2^1$ is increased to 0.15.

Figure 6.2 shows the behaviour of the synthetic and modelled data. The result of the $\tilde{q}_1^0$ coefficient is 0.98 on the night side and 0.51 on the day side. This is quite close to the minimum of about 0.5 and the maximum of about 1 in Figure 5.9.

Another look is taken into the phases compiled in Table 6.1. From Figure 5.9 a phase shift of nearly 12 hours can be seen which correlates very well with the one obtained from **'model 2'** using orbits (Tab. 6.1). The phase shift of $\omega_1 = -5.4°$ corresponds to a shift of -0.4 hours. From the $\tilde{q}_2^1$ coefficients of **'model 2'** using orbits a phase shift of $-42.6° \hat{=} -2.8$ hours is found. That means there is a difference in the phase for the local time effect of about 2.4 hours for the two methods.

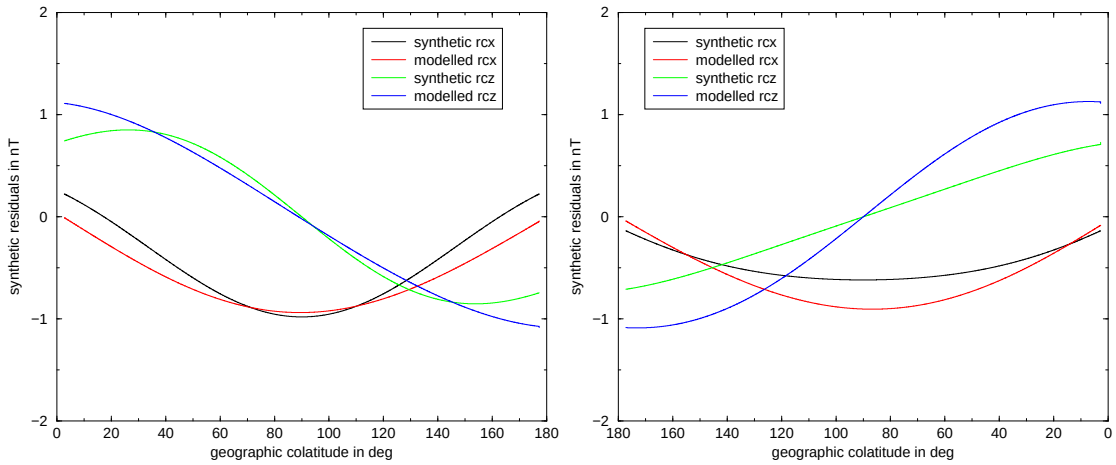

Figure 6.2: Synthetic values for the X- and Z-component of the external field variation in the second half of 2002 (rcx: black line, rcz: green line) on the night side (left panel) and day side (right panel). Calculated with $\tilde{q}_1^0 = 0.72$ and $\tilde{q}_2^1 = 0.15$.

Limiting the fit of the effect of external currents to low and mid-latitudes overestimates the local time dependence. The misfit at the poles, between the synthetic and inverted curves, of the in principal quite good fits in Figure 6.1 and 6.2, increases more and more.

6.3 How to include the correction into main field models

In conclusion, the potential of the magnetic field caused by the external current systems can be written as:

$$\begin{aligned} V &= a\left\{\hat{q}_1^0\left(\frac{r}{a}\right)P_1^0(\cos\Psi)\right. \\ &\quad +\left(\hat{q}_2^1\cos\lambda+\hat{s}_2^1\sin\lambda\right)\left(\frac{r}{a}\right)^2 P_2^1(\cos\Psi) \\ &\quad \left.+\hat{g}_1^0\left(\frac{a}{r}\right)^2 P_1^0(\cos\Psi)\right\} \end{aligned} \tag{6.8}$$

with the colatitude Ψ and longitude λ in the geomagnetic-local time frame. This

potential suggests a model for the external field which includes the variation of the ring current ($\hat{q}_1^0$), its induced part ($\hat{g}_1^0$) and the external quadrupole terms ($\hat{q}_2^1$, $\hat{s}_2^1$).

Two possible sets of coefficients are found directly from **'model 2'** using orbits and another one from the tracks, adjusted by the compatibility test. The two sets of coefficients reduced to the Earth's surface are:

result of **'model 2'** using orbits:

$$\hat{q}_1^0 = 26.3 - 0.68 \cdot D_{ST} \quad (6.9)$$

$$\hat{q}_2^1 = 1.4 - 0.035 \cdot D_{ST} \quad (6.10)$$

$$\hat{s}_2^1 = -1.5 + 0.039 \cdot D_{ST} \quad (6.11)$$

$$\hat{g}_1^0 = 0.33 \cdot 0.86 \cdot D_{ST} \quad (6.12)$$

result of tracks and compatibility test:

$$\hat{q}_1^0 = 26.3 - 0.67 \cdot D_{ST} \quad (6.13)$$

$$\hat{q}_2^1 = 0.5 - 0.013 \cdot D_{ST} \quad (6.14)$$

$$\hat{s}_2^1 = -5.0 + 0.13 \cdot D_{ST} \quad (6.15)$$

$$\hat{g}_1^0 = 0.33 \cdot 0.86 \cdot D_{ST} \quad (6.16)$$

The two sets of coefficients give the range of values for a ring current model as determined here. From this study it is recommended to use a mean value of the sets, probably with a slight preference of the second set of correction coefficients found from the test of model compatibility.

6.4 Comparison with other field models

Finally, the obtained results are compared to other main field models. The different corrections for the external field are combined in Table 6.2. The comparison is done with POMME [Maus et al., submitted 2003], a Magsat model [Langel et al., 1996] and the OIFM [Olsen et al., 2000a].

Because there is a correction for the ring current and other magnetospheric currents in POMME, the comparison is done in more detail. The unique feature of this model is the representation of the magnetospheric field in geocentric solar magnetospheric (GSM) coordinates. In an Earth fixed coordinate system (GEO) this constant mag-

	'model 2'*	**POMME***	**OIFM**	**Magsat**
q_1^0	26.3-0.68·D_{ST}	15.5**-0.76·D_{ST}	22.43-0.59·D_{ST}	18.4-0.63·D_{ST}
q_1^1	-	-	0.84+0.04·D_{ST}	-1.1-0.06·D_{ST}
s_1^1	-	-	-3.73+0.10·D_{ST}	-3.3+0.17·D_{ST}
$\hat{q}_2^1$	1.4-0.035·D_{ST}	-	-	-
$\hat{s}_2^1$	-1.5+0.039·D_{ST}	-	-	-
g_1^0	0.33·$\tilde{q}_1^{0***}$	-29593.85+0.32·$\tilde{q}_1^0$	-29617.37+0.27·$\tilde{q}_1^0$	-29991.6+0.27·$\tilde{q}_1^0$

Table 6.2: Comparison between different models of the external current system at the Earth's surface (all values are in nT). (* The values for **'model 2'** and **POMME** are in a geomagnetic - local time frame. ** POMME uses an additional constant term in GSM coordinates. *** the variable part of g_1^0.)

netospheric field appears as an annually and daily varying external field.

Commonly the factor for the D_{ST} dependent correction is found by co-estimation during the inversion. While $|D_{ST}|$ is restricted to values below $10nT$ this takes only a small range of possible D_{ST} values into account. A look into the whole range of D_{ST} showed that the usual values are too low. In POMME, a factor of 0.76 is found by the most reasonable fit for all D_{ST} values. The factor for the ratio between $\tilde{q}_1^0$ and $\tilde{g}_1^0$ is set to 0.32. These values are comparable to the obtained values found in **'model 2'** using orbits of $\tilde{q}_1^0 = 0.68 \cdot D_{ST}$ and $\tilde{g}_1^0 = 0.33 \cdot \tilde{q}_1^0$ at the Earth's surface.

A link can be found to induction studies. A possible explanation of the small LT dependence of the $\tilde{q}_2^1$ coefficient (Fig. 5.17) is probably given by suggestions from induction studies of S. Constable [Constable & Constable, submitted 2003] and G. Egbert (pers. comm.).

Magnetic satellites provide the possibility of electromagnetic induction studies with the aim to measure the Earth's conductivity. While magnetic satellites measure more than just the induced field S. Constable used the Comprehensive Model Phase 3 (CM3, [Sabak et al., 2002]) to remove the main field and its secular variation, the crustal field (caused by remanent and induced magnetisation), the field of iono-

spheric currents (like field aligned currents and the equatorial electrojet) and the coupling and induction effect of all these.

G. Egbert considered that the induced internal field can be described by the sum of the dipole surface harmonic ($\tilde{q}_1^0$) and the quadrupole surface harmonic ($\tilde{q}_2^1$). Especially, when using satellite data this quadrupole term has to be added. His result is that a $\tilde{q}_2^1$ coefficient which is about 0.25 of $\tilde{q}_1^0$ produces roughly the correct amount of variation with local time, which is caused by external currents. In comparison, here the value 0.21 is obtained at satellite altitude, if the corrections are done like suggested from the test of the model compatibility (Eq. 6.13 - 6.16).

Chapter 7

Summary and Outlook

The aim of this study was to find a model which describes the effect of the external current system. A typical description is done by spherical harmonic analysis (SHA). Each component of the Earth's magnetic field can be described by a set of coefficients. A separation between internal and external contributions is possible. Here, SHA are used to describe the external part of the Earth's magnetic field. Using vector data and ***repeat tracks*** is very helpful to model external field components. The analysis was done using the vertical component, Z, and the northward horizontal component, X. The corresponding matrices can be inverted directly. From time to time CHAMP is flying in resonance with the Earth. During such periods ***repeat tracks*** were available. For each of the two ***repeat tracks*** the residuals between the measured data and the CO2 main field model were calculated. The difference between these 'repeat track residuals' are free of inconsistencies linked to the main field model or the D_{ST}-baselines. Moreover, lithospheric signals are eliminated. The residuals were used as input for a model of the external magnetic field.

First, a model was computed using scalar data for tracks from 40° to 140° co-latitude (**'model 1'**) while vector data were not yet available. Scalar data were easier to handle, however, more assumptions had to be made. The suggested model of the external contributions to the Earth's magnetic field was a totally symmetric ring current in the equatorial plane. From these investigations it could be seen, that this model was too much simplified. The results of **'model 1'** showed that not only the symmetric part of the ring current is influencing the geomagnetic field at

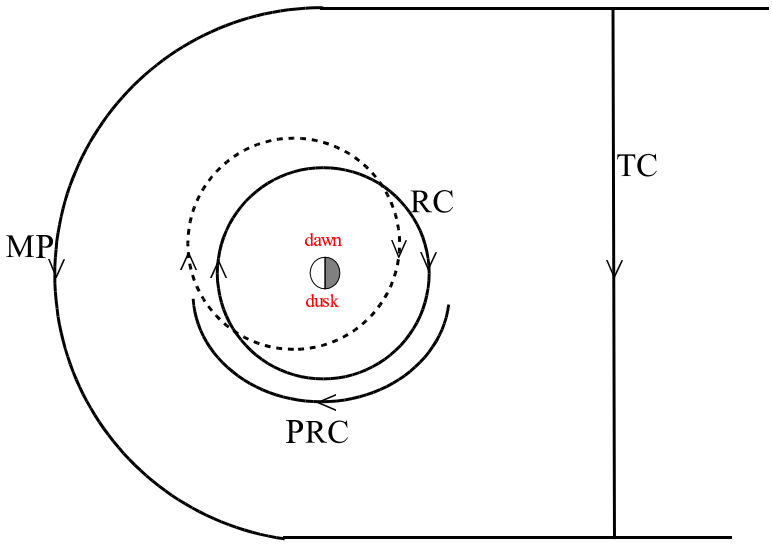

Figure 7.1: Magnetospheric currents in the equatorial plane: ring current (RC), partial ring current (PRC), magnetopause current (MP), and tail current (TC). The dashed line illustrates the put off ring current.

the Earth's surface. The asymmetric part of the ring current and currents in much higher orbits, like the magnetopause current and the tail current, have to be taken into account. In spite of these problems a local time dependence was found. To improve **'model 1'** the use of vector data was considered (**'model 2'**). To produce vector data is more difficult (e. g., the exact position and attitude has to be known), but after May 2001 the three components of the magnetic field from the CHAMP vector magnetometer were available.

Results of **'model 1'** (Chap. 4) and **'model 2'** (Sec. 5.1) using tracks from 40° to 140° colatitude, showed that the influence of currents at high latitudes has to be corrected before modelling the effect of large-scale magnetospheric currents. For further improvements the use of whole orbits was suggested. With the approach of using vector data for whole orbits and applying a correction around the poles, a more precise model of the Earth's magnetic field of external origin was obtained.

Figure 7.1 shows the resulting effective 'ring current'. This is meant to be the effect of the combination of all external currents. The effect of all external currents (ring

current, partial ring current, magnetopause current and tail current) are summed up and can be compared to a 'ring current' with an offset in the direction between noon and dawn, as it is shown. It would produce a minimum in the morning hours at around 0900 LT and a maximum in the evening at around 2100 LT as obtained in Chapter 5 (compare Fig. 5.9).
From these results it is clear, that it is better to describe the external magnetic field in geomagnetic coordinates and in a local time frame.

These promising results will allow to include the obtained parametrisation of external fields in main field modelling, in order to correct the effect of large-scale magnetospheric current systems. A first main field model including results of **'model 2'** using tracks from 40° to 140° colatitude was done during a visit at the Institute de Physique du Globe de Paris (IPGP), France.

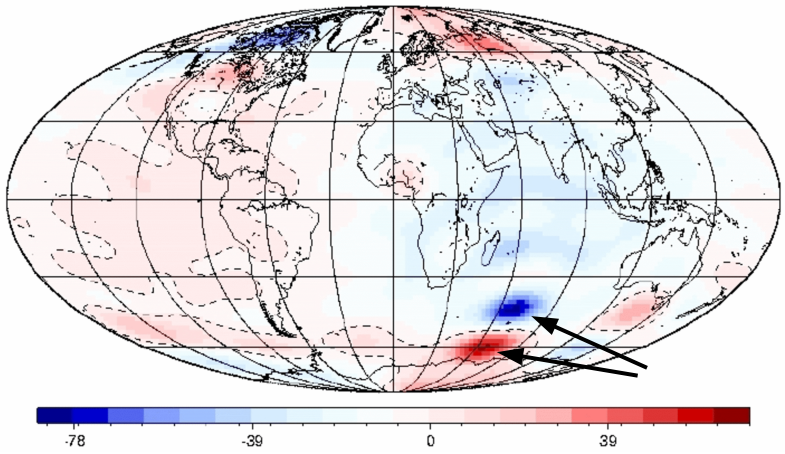

Figure 7.2: Difference of the X-component of an 'uncorrected model' and the X-component of a 'corrected model'. The differences range from -85 nT to 70 nT (from A. Chambodut, pers. comm.).

Figure 7.2 shows a comparison for the X-component between an 'uncorrected' and a 'corrected' model. The aim of this test was to estimate the differences between main field models computed with and without our ring current model. The residuals between the CO2 model and a model which is uncorrected for external currents ('uncorrected model') and the residuals between the CO2 model and a model which is corrected for external currents ('corrected model') were calculated. Afterwards

these residuals were subtracted from each other and the difference between these two new residuals is plotted in Figure 7.2. Deviations of the order of some tens of nT can be observed. The result of this first model shows the problem of using vector data only from 40° to 140° in main field modelling. It can be seen, that some edge effect may occur just near the limit of the considered latitude interval, indeed around 140° colatitude (arrows). Also the behaviour of the power spectra (Fig. 7.3) was analysed, which indicates some differences, especially at higher latitudes.

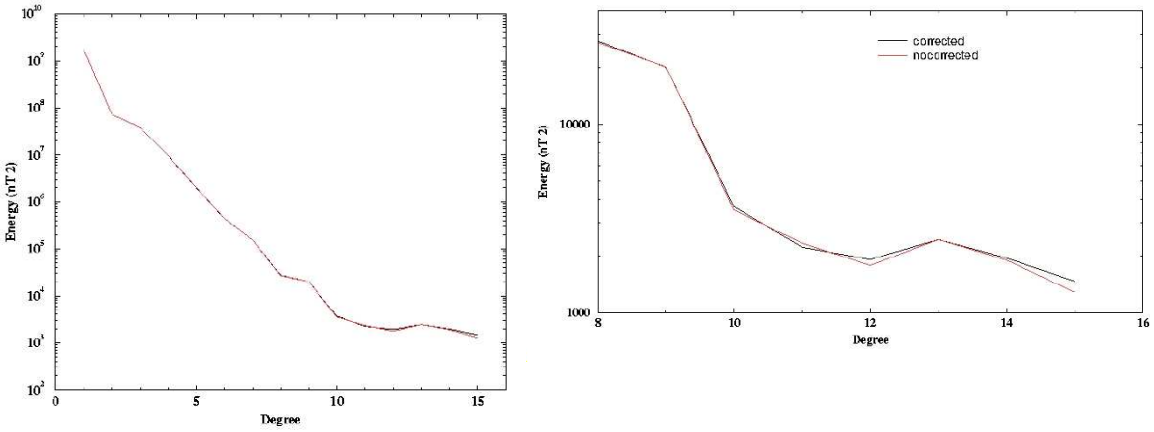

Figure 7.3: Power spectra of usually corrected and 'rccorrected' models. Detailed view in right panel (from A. Chambodut, pers. comm.).

It is emphasised how important it is to include a parametrisation of the external current systems in main field modelling. Applying the obtained correction in the geomagnetic-local time frame will help to improve the results in main field modelling.

The model presented here could be used for a continuous monitoring of the ring current from low Earth orbiting satellites. Considering the three presently active magnetic field satellites, SAC-C in its 1030/2230 LT orbit could be used for a routinely determination of a space-based equivalent to the D_{ST} index. This new index would then be used for parametrising the magnetospheric currents in studies of data from the other satellites. This kind of external field correction is not only needed for main field modelling, but also required for all kinds of ionospheric current studies.

Bibliography

Akasofu, S. I., Chapman, S., & Meng, C. I., 1965. The polar electrojet, *Journal of Atmospheric and Terrestrial Physics*, **27**, 1275–1300.

Berthelier, A. & Menvielle, M., 1991. *IAGA Bulletin No. 40*, IAGA (http://swdcwww.kugi.kyoto-u.ac.jp/dst2/onDstindex.html).

Bloxham, J. & Gubbins, D., 1985. The secular variation of Earth's magnetic field, *Nature*, **317**, 777–781.

Bronstein, I. N. & Semendjajew, K. A., 1989. *Taschenbuch der Mathematik*, Gemeinschaftsausgabe Verlag Nauka, Moskau und BSB B. G. Teubner Verlagsgesellschaft, Leipzig.

Cain, J. C., Mozzoni, D. T., Ferguson, B. B., & Ajayi, O., 2003. Geomagnetic secular variation 1995 - 2000, *J. Geophysic. Res.*, **108**(B3).

Campbell, W. H., 1997. *Introduction to Geomagnetic Fields*, Cambridge University Press.

Chambodut, A., Schwarte, J., Langlais, B., Lühr, H., & Mandea, M., 2003. The selection of data in field modeling, in *Proceedings of the 4th Ørsted International Science Team conference*, Narayana Press, Copenhagen.

CHAMP, 2003. http://www.gfz-potsdam.de/champ.

Chapman, S. & Ferraro, V. C. A., 1930. A new theory of magnetic storms, *Nature*, **126**.

Constable, S. & Constable, C., submitted 2003. Observing geomagnetic induction in magnetic satellite measurements and associated implications

for mantle conductivity, G^3, *An electronic journal of the Earth sciences, (http://www.agu.org/journals/gc/).*

Daglis, I. A., Thorne, R. M., Baumjohann, W., & Orsini, S., 1999. The terrestrial ring current: Origin, formation, and decay, *Rev. Geophys.*, **37**, 407–438.

EUROCONTROL, 1997. Surveying of navigation facilities, *EUROCONTROL Standard document, Reference 007-97.*

Gauss, C. F., 1839. *Allgemeine Theorie des Erdmagnetismus*, Leipzig.

Hemant, K., 2003. *Modelling and interpretation of global lithospheric magnetic anomalies*, Ph.D. thesis, Freie Universität Berlin (http://www.diss.fu-berlin.de/2003/270).

Holme, R. T., Olsen, N., Rother, M., & Lühr, H., 2003. CO2 - A CHAMP magnetic field model, in *First CHAMP Mission Results for Gravity, Magnetic and Atmospheric Studies*, Springer Verlag, Berlin.

Holschneider, M., Chambudut, A., & Mandea, M., 2003. From global to regional analysis of the magnetic field on the sphere using wavelet frames, *Phys. Earth Planet. Int.*, **135**, 107–124.

Ivers, D., Stening, R., Turner, J., & Winch, D., 2003. Equatorial electrojet from ørsted scalar magnetic field observations, *J. Geophys. Res.*, **108**(A2).

Jacobs, J. A., ed., 1987. *Geomagnetism*, vol. 1, chap. 4, The Main Field by R. A. Langel, Academic Press.

Jacobs, J. A., ed., 1989. *Geomagnetism*, vol. 3, chap. 5, Indices of Geomagnetic Activity by G. K. Rangarajan, Academic Press.

Jonkers, A. R. T., Jackson, A., & Murray, A., 2003. Four centuries of geomagnetic data from historical records, *Rev. Geophys.*.

Kertz, W., 1989. *Einführung in die Geophysik I + II*, BI Hochschultaschenbücher, Band 275 + 535.

Kivelson, M. G. & Russell, C. T., eds., 1995. *Introduction to Space Physics*, Cambridge University Press.

Langel, R. A. & Estes, R. H., 1985. Large-scale, near-earth magnetic fields from external sources and the corresponding induced internal field, *J. Geophys. Res.*, **90**, 2487–2494.

Langel, R. A., Sabaka, T. J., Baldwin, R. T., & Conrad, J. A., 1996. The near-earth magnetic field from magnetospheric and quiet-day ionospheric sources and how it is modeled, *Phys. Earth Planet. Int.*, **98**, 235–267.

MAGSAT, 2003. http://nssdc.gsfc.nasa.gov/space/space_phys/nmagsat.html.

Mandea, M., 2003. Main field modelling, in *Encyclopedia*.

Mandea, M. & Dormy, E., 2003. Asymmetric behavior of magnetic dip poles, *Earth Planets Space*, **55**, 153–157.

Maus, S., Rother, M., Holme, R., Lühr, H., Olsen, N., & Haak, V., 2002. First scalar magnetic anomaly map from CHAMP satellite data indicates weak lithospheric field, *Geophys. Res. Lett.*, **29**(14).

Maus, S., Balasis, G., Lühr, H., Rother, M., & Mandea, M., submitted 2003. Introducing POMME - Potsdam Magnetic Model of the Earth, in *Proceedings of the 2nd CHAMP science meeting*.

Mayer, C. & Maier, T., 2003. Multiscale Determination of Radial Current Distribution from CHAMP FGM-Data, in *Fist CHAMP Mission Results for Gravity, Magnetic and Atmospheric Studies*, Springer Verlag, Berlin.

Merrill, R. T., McElhinny, M. W., & McFadden, P. L., 1998. *The magnetic field of the Earth - Paleomagnetism, the Core, and the Deep Mantle*, Academic Press, International Geophysics Series, Vol. 63.

Olsen, N., 2002. A model of the geomagnetic field and its secular variation for epoch 2000 estimated from Ørsted data, *Geophys. J. Int.*, **149**, 454–462.

Olsen, N., Holme, R., Hulot, G., Sabaka, T., Neubert, T., Tøffner-Clausen, L., Primdahl, F., Jørgensen, J., Léger, J.-M., Barraclough, D., Bloxham, J., Cain, J., Constable, C., Golovkov, V., Jackson, A., Kotze, P., Langlais, B., Macmillan, S., Mandea, M., Merayo, J., Newitt, L., Purucker, M., Risbo, T., Stampe, M., Thomson, A., & Voorhies, C., 2000. Ørsted initial field model, *Geophys. Res. Lett.*, **27**, 3607–3610.

Olsen, N., Sabaka, T. J., & Tøffner-Clausen, L., 2000. Determination of the IGRF2000 model, *Earth Planets Space*, **52**, 1175–1182.

Ørsted, 2003. http://web.dmi.dk/projects/oersted.

Parker, T. L. & Shure, L., 1982. Efficient modelling of the Earth's magnetic field with harmonic splines, *Geophys. Res. Lett.*, **9**, 812–815.

Pervot, M., 1985. How the geomagnetic field vector reverses polarity, *Nature*, **316**(230).

Russell, C., 1971. Geophysical coordinate transformations, *Cosmic Electrodynamics*, **2**, 184–196.

Sabak, T. J., Olsen, N., & Langel, R. A., 2002. A comprehensive model of the quiet-time, near-Earth magnetic field: phase 3, *Geophys. J. Int.*, **151**, 32–68.

SAC-C, 2003. http://www.gsfc.nasa.gov/gsfc/service/gallery/fact_sheets/spacesci/sac-c.htm.

Shure, L., Parker, T. L., & Backus, G. E., 1982. Harmonic splines for geomagnetic modelling, *Phys. Earth Planet. Int.*, **28**, 215–229.

Stauning, P. & Primdahl, F., 2000. First detection of global dawn-dusk ionospheric current intensities using Ampere's intergral law on Ørsted orbits, *Geophys. Res. Let.*, **27**, 3273–3276.

Stern, D. P., 1996. A brief history of magnetospheric physics during the space age, *Rev. Geophys.*, **34**.

Stern, D. P., 2002. A millenium of geomagnetism, *Rev. Geophys.*, **40**.

WDC-Kyoto, 2003. http://swdcdb.kugi.kyoto-u.ac.jp/.

Appendix A

More model results

Model results from 'model 2' using tracks

Correlation Coefficient							
	D_{ST} vs g_1^0	D_{ST} vs q_1^0	q_1^0 vs g_1^0		D_{ST} vs g_1^0	D_{ST} vs q_1^0	q_1^0 vs g_1^0
19 LT	0.83	0.90	0.95	07 LT	0.86	0.83	0.86
20 LT	0.89	0.93	0.97	08 LT	0.87	0.82	0.82
21 LT	0.81	0.87	0.97	09 LT	0.88	0.90	0.82
22 LT	0.83	0.87	0.95	10 LT	0.75	0.83	0.58
23 LT	0.77	0.83	0.86	11 LT	0.63	0.77	0.49
00 LT	0.82	0.89	0.96	12 LT	0.77	0.87	0.87
01 LT	0.77	0.88	0.95	13 LT	0.55	0.82	0.81
02 LT	0.90	0.95	0.97	14 LT	0.90	0.97	0.94
03 LT	0.71	0.83	0.92	15 LT	0.70	0.86	0.79
04 LT	0.94	0.95	0.94	16 LT	0.89	0.96	0.93
05 LT	0.88	0.90	0.96	17 LT	0.74	0.89	0.73
06 LT	0.91	0.85	0.88	18 LT	0.88	0.92	0.95

Slope							
	D_{ST} vs g_1^0	D_{ST} vs q_1^0	q_1^0 vs g_1^0		D_{ST} vs g_1^0	D_{ST} vs q_1^0	q_1^0 vs g_1^0
19 LT	0.24	1.01	0.24	07 LT	0.20	0.49	0.33
20 LT	0.28	1.09	0.26	08 LT	0.21	0.48	0.33
21 LT	0.20	0.82	0.26	09 LT	0.20	0.67	0.26
22 LT	0.20	0.88	0.23	10 LT	0.21	0.66	0.21
23 LT	0.20	0.77	0.24	11 LT	0.20	0.65	0.19
00 LT	0.16	0.69	0.24	12 LT	0.22	0.65	0.34
01 LT	0.19	0.74	0.27	13 LT	0.17	0.61	0.33
02 LT	0.20	0.76	0.28	14 LT	0.18	0.73	0.25
03 LT	0.13	0.50	0.28	15 LT	0.27	0.99	0.26
04 LT	0.19	0.62	0.29	16 LT	0.28	0.93	0.30
05 LT	0.18	0.56	0.31	17 LT	0.26	0.98	0.23
06 LT	0.21	0.47	0.37	18 LT	0.28	1.08	0.26
Intercept							
	D_{ST} vs g_1^0	D_{ST} vs q_1^0	q_1^0 vs g_1^0		D_{ST} vs g_1^0	D_{ST} vs q_1^0	q_1^0 vs g_1^0
19 LT	-0.06	-1.80	0.37	07 LT	-0.06	-0.55	0.17
20 LT	0.14	-0.03	0.15	08 LT	0.68	-0.59	0.53
21 LT	-0.21	0.15	-0.22	09 LT	0.06	-0.22	0.11
22 LT	-0.02	-0.91	0.19	10 LT	0.30	-0.44	0.52
23 LT	-0.21	-0.06	-0.17	11 LT	0.06	0.17	0.16
00 LT	0.03	0.12	0.01	12 LT	0.64	0.30	0.54
01 LT	0.22	1.21	-0.25	13 LT	0.91	2.16	-0.05
02 LT	0.93	-0.27	1.08	14 LT	-0.88	0.85	-1.07
03 LT	0.05	1.43	-0.44	15 LT	-0.28	-0.09	-0.19
04 LT	0.25	-0.90	0.46	16 LT	0.10	2.66	-0.68
05 LT	-0.10	0.12	-0.14	17 LT	-1.53	0.40	-1.67
06 LT	-0.05	-1.77	0.51	18 LT	-0.01	-0.01	0.03

Table A.1: Statistical results of the comparison between the two Gauss coefficients g_1^0 and q_1^0 and D_{ST} for all local times calculated from vector data using tracks from 40° to 140° colatitude.

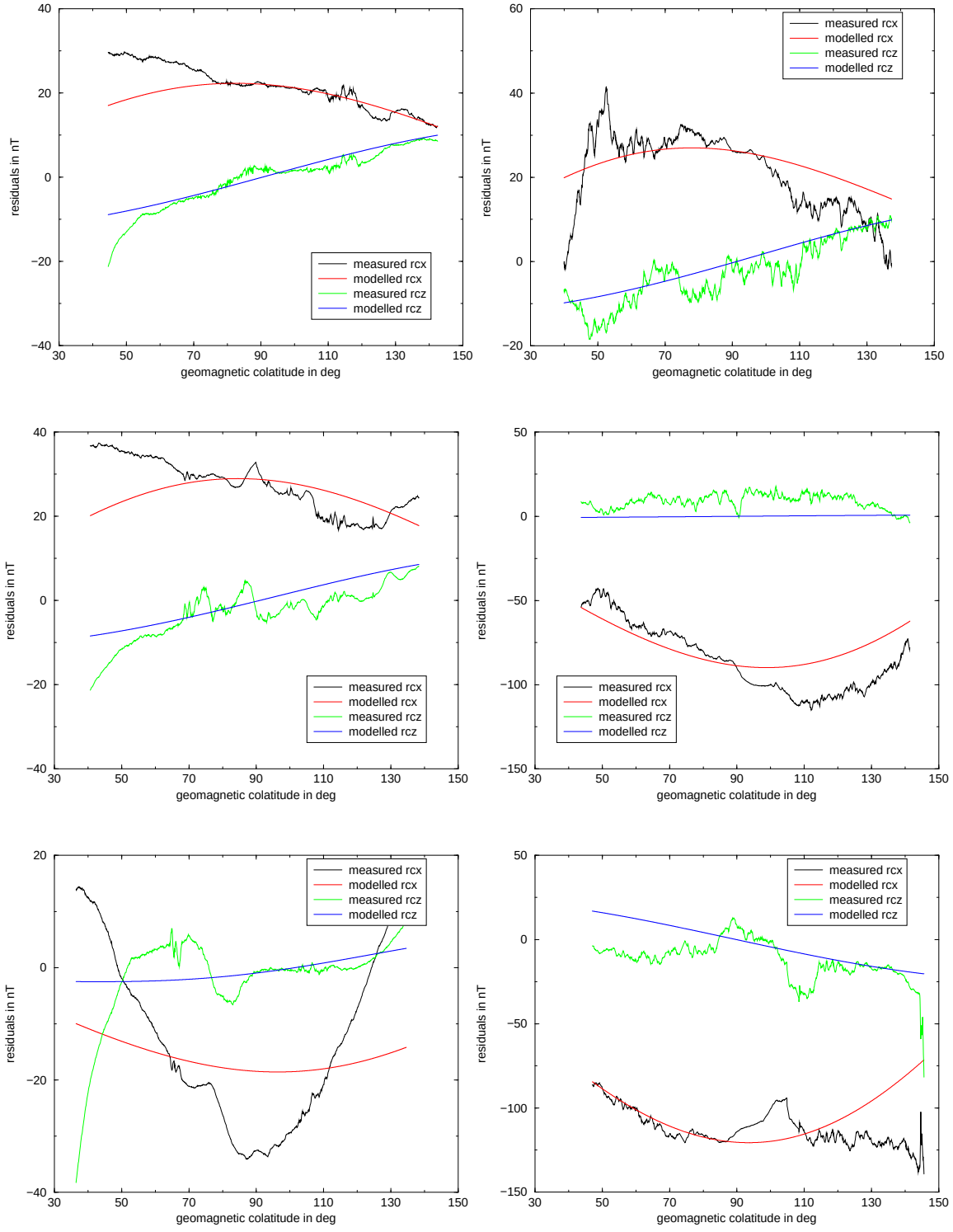

Figure A.1: One day of modelled tracks from **'model 2'** using tracks from 40° to 140° colatitude. Plotted are the 1st to 6th tracks on the chosen day September, 4, 2002.

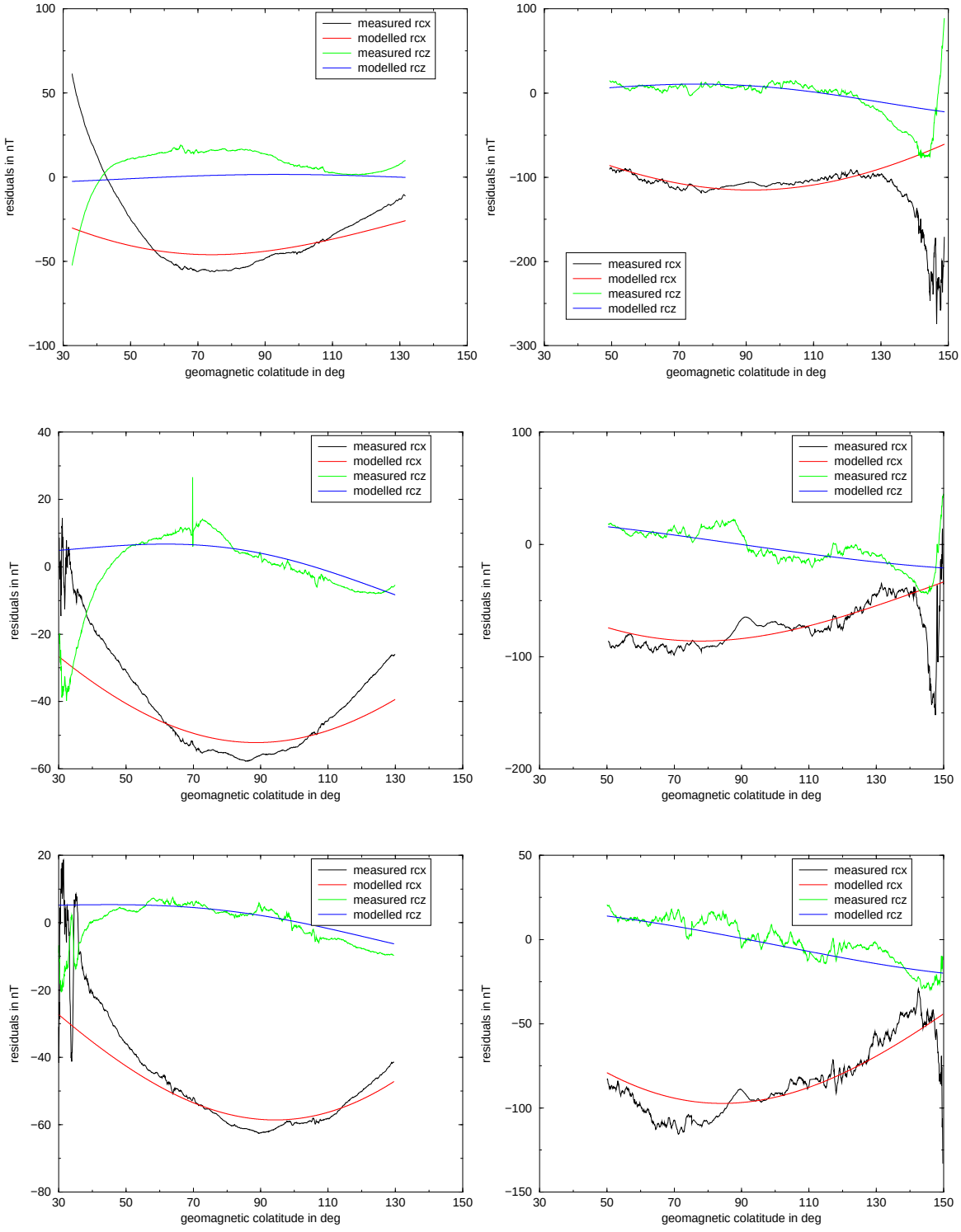

Figure A.2: One day of modelled tracks from **'model 2'** using tracks from 40° to 140° colatitude. Plotted are the 7th to 12th tracks on the chosen day September, 4, 2002.

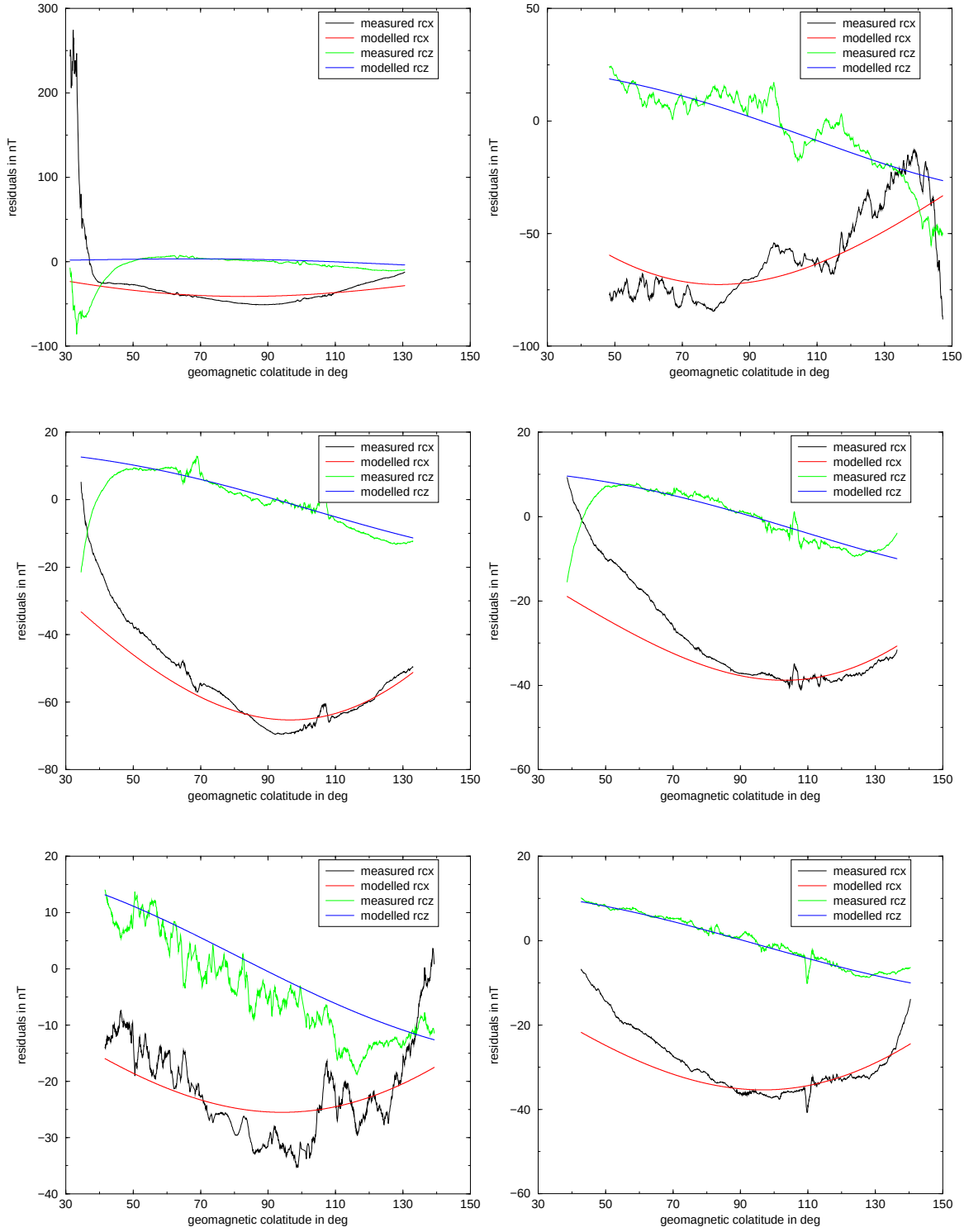

Figure A.3: One day of modelled tracks from **'model 2'** using tracks from 40° to 140° colatitude. Plotted are the 13th to 19th (the 17th track is missing due to a gap in the data) tracks on the chosen day September, 4, 2002.

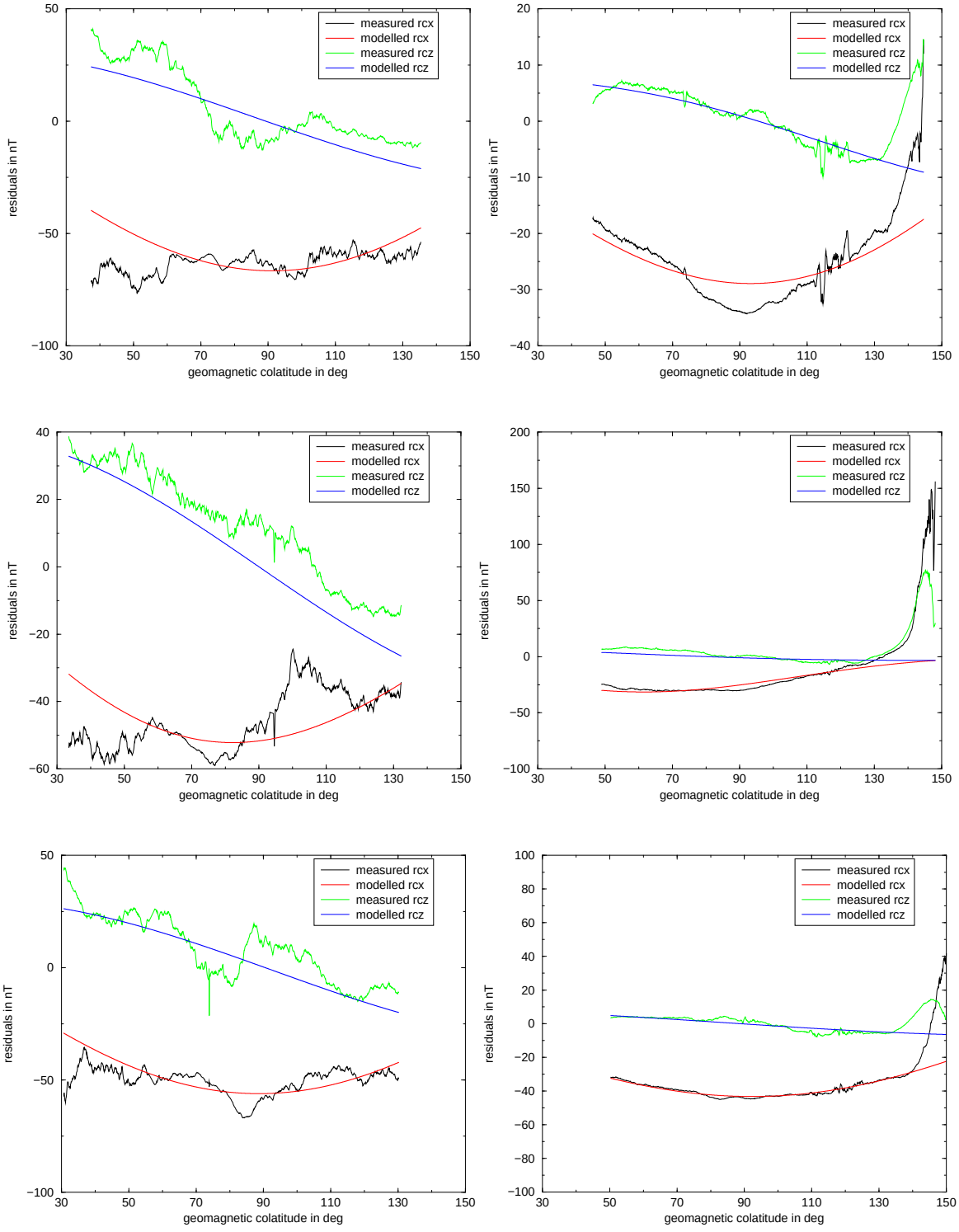

Figure A.4: One day of modelled tracks from **'model 2'** using tracks from 40° to 140° colatitude. Plotted are the 20th to 26 tracks on the chosen day September, 4, 2002.

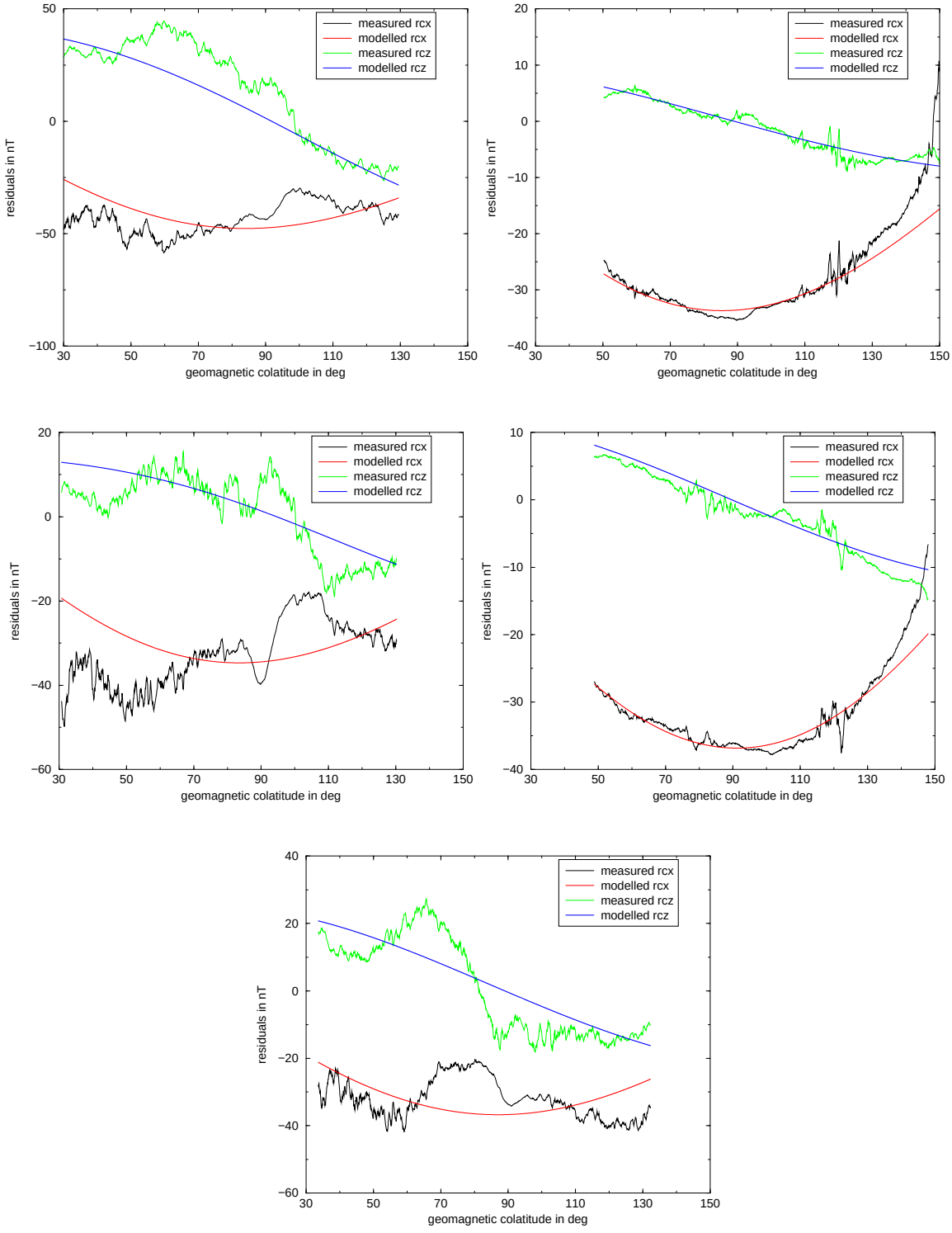

Figure A.5: One day of modelled tracks from **'model 2'** using tracks from 40° to 140° colatitude. Plotted are the 27th to 31st tracks on the chosen day September, 4, 2002.

The following Table A.2 contains the longitude and local time of the equator crossing of the shown tracks in Figures A.1 to A.5.

Plot	**Longitude**	**Local time**
Fig. A.1, top, left	38.8°	3:26
Fig. A.1, top, right	-152.9°	15:26
Fig. A.1, middle, left	15.5°	3:26
Fig. A.1, middle, right	-176.2°	15:25
Fig. A.1, bottom, left	-7.8°	3:26
Fig. A.1, bottom, right	160.6°	15:25
Fig. A.2, top, left	-31.0°	3:25
Fig. A.2, top, right	137.3°	15:25
Fig. A.2, middle, left	-54.3°	3:25
Fig. A.2, middle, right	114.1°	15:24
Fig. A.2, bottom, left	-77.5°	3:25
Fig. A.2, bottom, right	90.8°	15:24
Fig. A.3, top, left	-100.8°	3:24
Fig. A.3, top, right	67.6°	15:24
Fig. A.3, middle, left	-124.1°	3:24
Fig. A.3, middle, right	-147.3°	3:24
Fig. A.3, bottom, left	21.0°	15:23
Fig. A.3, bottom, right	-170.6°	3:23
Fig. A.4, top, left	-2.2°	15:23
Fig. A.4, top, right	166.2°	3:23
Fig. A.4, middle, left	-25.5°	15:22
Fig. A.4, middle, right	142.9°	3:23
Fig. A.4, bottom, left	-48.7°	15:22
Fig. A.4, bottom, right	119.7°	3:23

Fig. A.5, top, left	-72.0°	15:22
Fig. A.5, top, right	96.4°	3:22
Fig. A.5, middle, left	-95.3°	15.21
Fig. A.5, middle, right	73.1°	3:22
Fig. A.5, bottom	-118.5°	15:21

Table A.2: September, 4, 2002: Longitude and local time of the equator crossing for each track corresponding to Figures A.1- A.5.

Model results from 'model 2' using orbits

Correlation Coefficient				
	D_{ST} vs g_1^0	D_{ST} vs q_1^0	q_1^0 vs g_1^0	D_{ST} vs q_2^1
2240 LT	0.79	0.88	0.93	-0.26
2308 LT	0.84	0.92	0.93	-0.46
2335 LT	0.84	0.93	0.93	-0.49
0003 LT	0.81	0.93	0.91	-0.45
0026 LT	0.76	0.92	0.91	-0.66
0057 LT	0.67	0.87	0.82	-0.62
0124 LT	0.74	0.93	0.86	-0.17
0152 LT	0.81	0.93	0.92	-0.26
0219 LT	0.84	0.93	0.96	-0.50
0245 LT	0.76	0.86	0.93	0.04
0313 LT	0.70	0.83	0.92	0.40
0340 LT	0.70	0.87	0.90	-0.03
0407 LT	0.88	0.96	0.96	0.26
0434 LT	0.90	0.96	0.96	0.38
0501 LT	0.87	0.92	0.95	0.47
0528 LT	0.91	0.96	0.94	0.61
0555 LT	0.91	0.94	0.94	0.59
0622 LT	0.78	0.82	0.92	0.33

0650 LT	0.87	0.91	0.94	0.41
0717 LT	0.90	0.96	0.92	0.53
0744 LT	0.88	0.95	0.90	0.53
0812 LT	0.84	0.90	0.90	0.51
0839 LT	0.83	0.90	0.91	0.25
0906 LT	0.82	0.93	0.91	0.15
0934 LT	0.85	0.95	0.91	0.20
0944 LT	0.88	0.94	0.92	0.24
1028 LT	0.89	0.94	0.92	0.51

Slope				
	D_{ST} vs g_1^0	D_{ST} vs q_1^0	q_1^0 vs g_1^0	D_{ST} vs q_2^1
2240 LT	0.19	0.70	0.29	-0.03
2308 LT	0.22	0.74	0.30	-0.05
2335 LT	0.18	0.68	0.27	-0.04
0003 LT	0.16	0.67	0.26	-0.04
0026 LT	0.19	0.69	0.26	-0.07
0057 LT	0.17	0.69	0.27	-0.07
0124 LT	0.18	0.71	0.24	-0.02
0152 LT	0.18	0.77	0.24	-0.03
0219 LT	0.18	0.72	0.27	-0.04
0245 LT	0.19	0.70	0.28	0.0
0313 LT	0.18	0.70	0.28	0.04
0340 LT	0.15	0.72	0.26	0.0
0407 LT	0.20	0.72	0.29	0.02
0434 LT	0.21	0.74	0.29	0.03
0501 LT	0.21	0.70	0.31	0.04
0528 LT	0.25	0.74	0.33	0.07
0555 LT	0.25	0.75	0.33	0.07
0622 LT	0.24	0.72	0.32	0.05
0650 LT	0.21	0.70	0.29	0.05
0717 LT	0.22	0.71	0.30	0.06

0744 LT	0.23	0.72	0.32	0.07
0812 LT	0.27	0.73	0.31	0.08
0839 LT	0.22	0.70	0.32	0.03
0906 LT	0.20	0.71	0.30	0.02
0934 LT	0.20	0.72	0.28	0.03
0944 LT	0.20	0.74	0.27	0.03
1028 LT	0.22	0.76	0.28	0.0

Intercept				
	D_{ST} vs g_1^0	D_{ST} vs q_1^0	q_1^0 vs g_1^0	D_{ST} vs q_2^1
2240 LT	-0.55	-2.51	0.15	-0.05
2308 LT	0.36	0.82	0.11	-0.02
2335 LT	0.06	-0.27	0.17	0.08
0003 LT	0.16	0.03	0.16	0.01
0026 LT	0.38	0.44	0.29	-0.01
0057 LT	0.93	3.95	-0.19	-0.53
0124 LT	-0.12	4.53	-1.27	0.17
0152 LT	-0.70	0.77	-0.94	0.24
0219 LT	-0.51	-0.51	-0.39	0.11
0245 LT	0.07	0.94	-0.27	0.15
0313 LT	-0.04	0.75	-0.36	-0.24
0340 LT	0.22	0.87	-0.17	0.01
0407 LT	-0.49	-0.62	-0.25	-0.16
0434 LT	-0.02	0.58	-0.12	0.18
0501 LT	-0.40	0.61	-0.58	-0.10
0528 LT	0.09	0.02	0.08	-0.01
0555 LT	0.39	-0.08	0.43	0.08
0622 LT	0.10	-1.07	0.39	0.19
0650 LT	-0.63	-1.14	-0.29	-0.19
0717 LT	-0.06	-0.56	0.10	-0.09
0744 LT	0.27	-0.37	0.37	0.02
0812 LT	-0.09	-0.67	0.17	-0.17

0839 LT	0.04	-0.62	0.23	-0.16
0906 LT	-0.24	-0.12	-0.19	0.10
0934 LT	0.00	0.14	-0.04	0.19
0944 LT	0.09	-0.21	0.15	0.03
1028 LT	-0.49	-0.37	-0.38	-1.00

Table A.3: Statistical results of the comparison between the three Gauss coefficients g_1^0, q_1^0, q_2^1 and D_{ST} for all local times calculated from vector data using whole orbits.

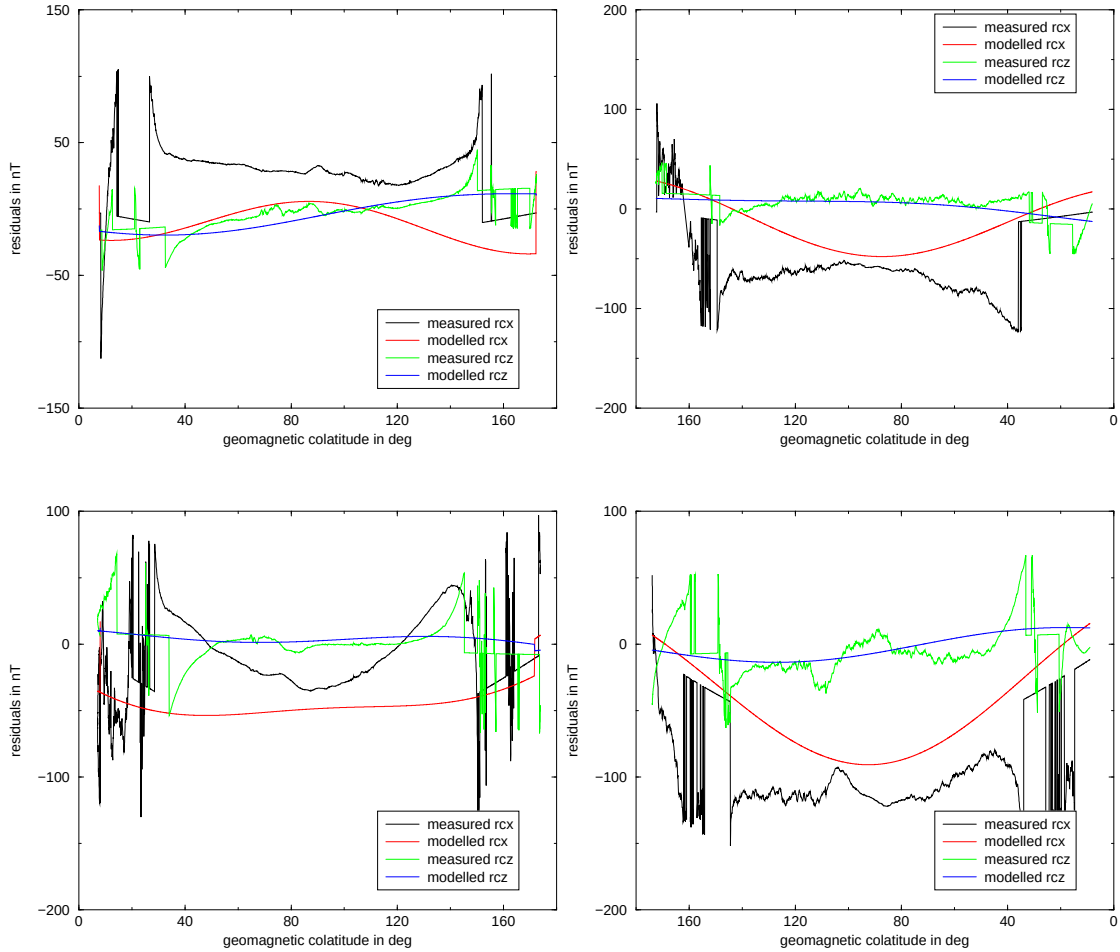

Figure A.6: One day of modelled orbits from **'model 2'** using full orbits. Plotted are the 1st to 2rd orbits (first half-orbit in the left panel, starting at the North pole and second half-orbit in the right panel) on the chosen day September, 4, 2002.

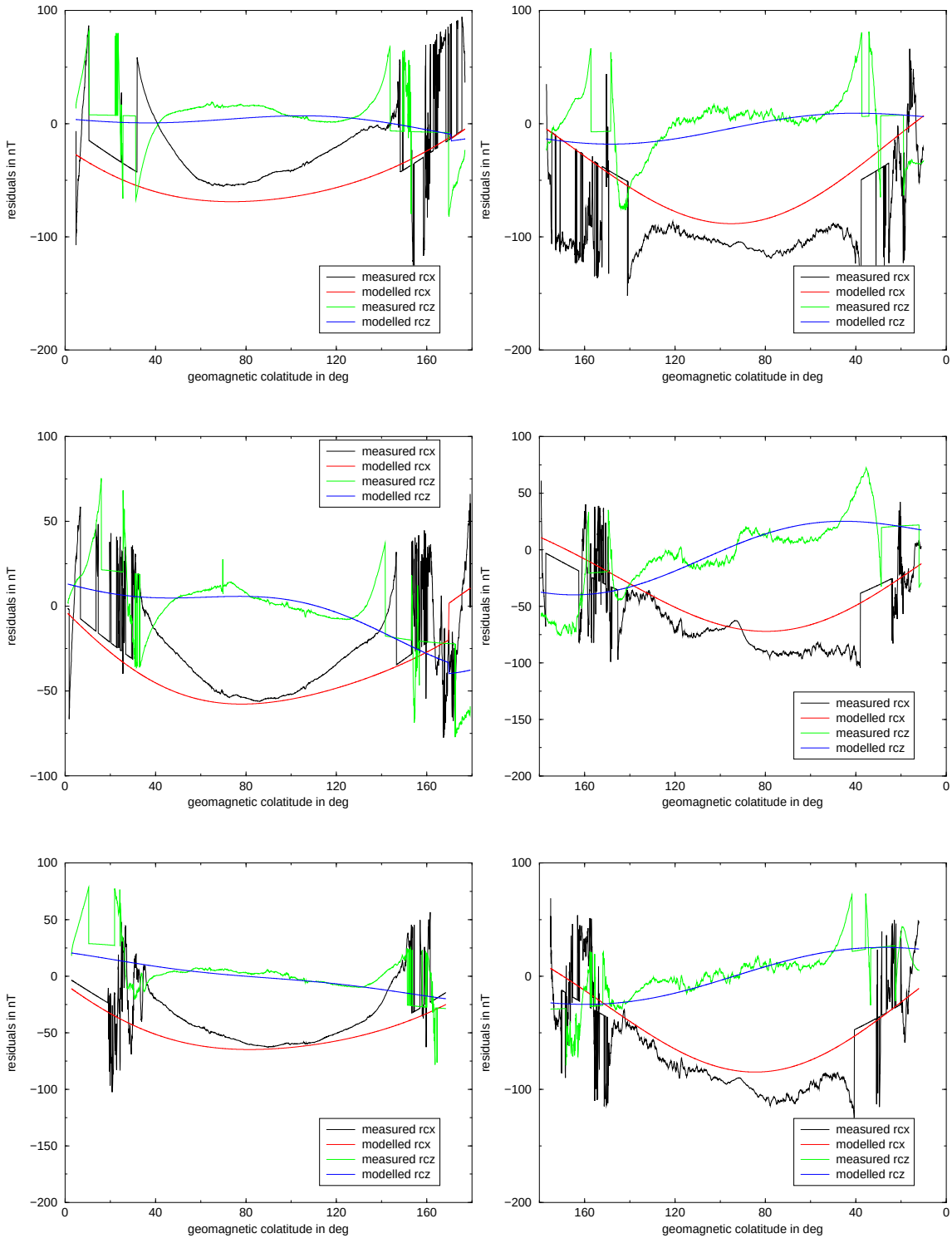

Figure A.7: One day of modelled orbits from **'model 2'** using full orbits. Plotted are the 3rd to 5th orbits (first half-orbit in the left panel, starting at the North pole and second half-orbit in the right panel) on the chosen day September, 4, 2002.

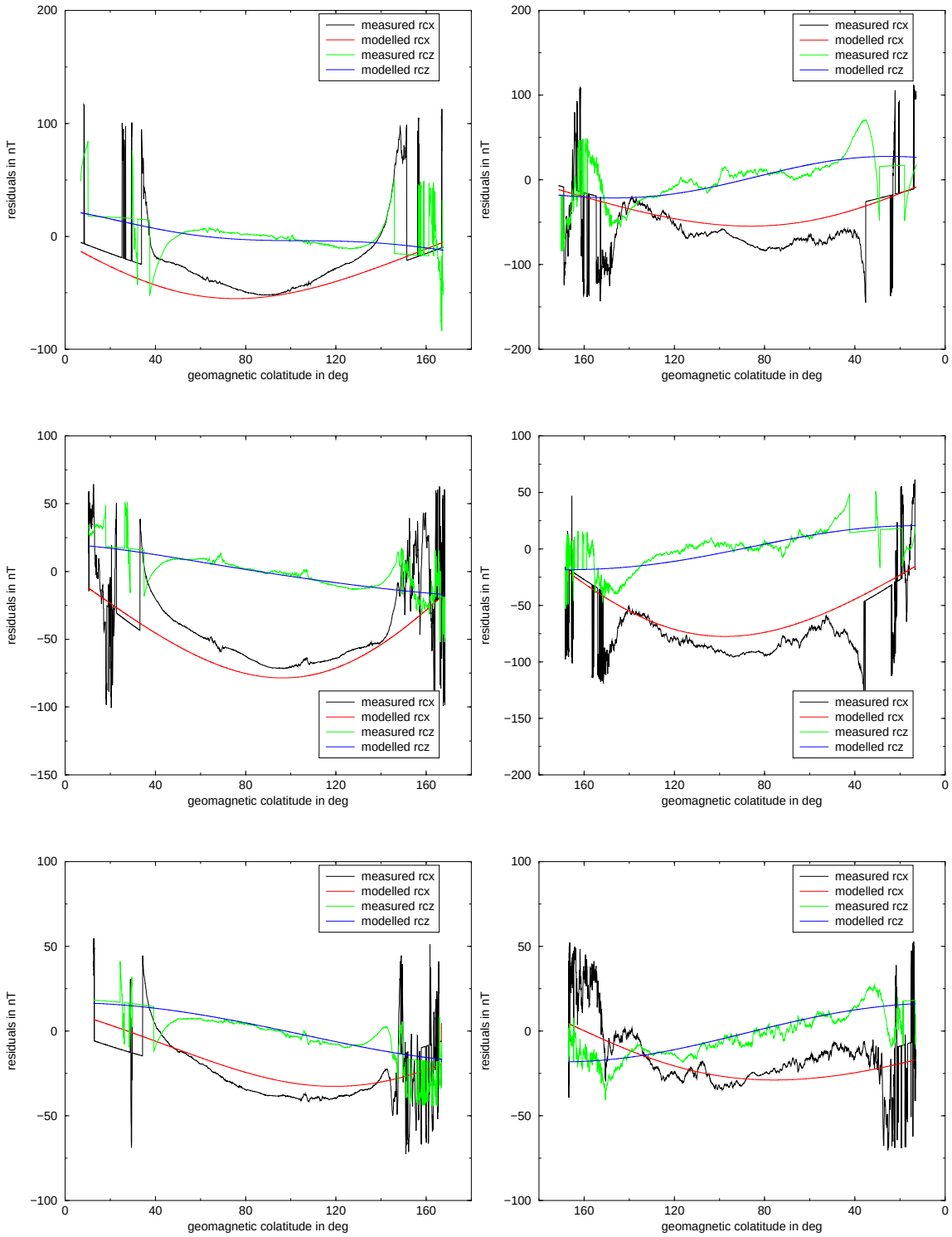

Figure A.8: One day of modelled orbits from **'model 2'** using full orbits. Plotted are the 6th to 8th orbits (first half-orbit in the left panel, starting at the North pole and second half-orbit in the right panel) on the chosen day September, 4, 2002.

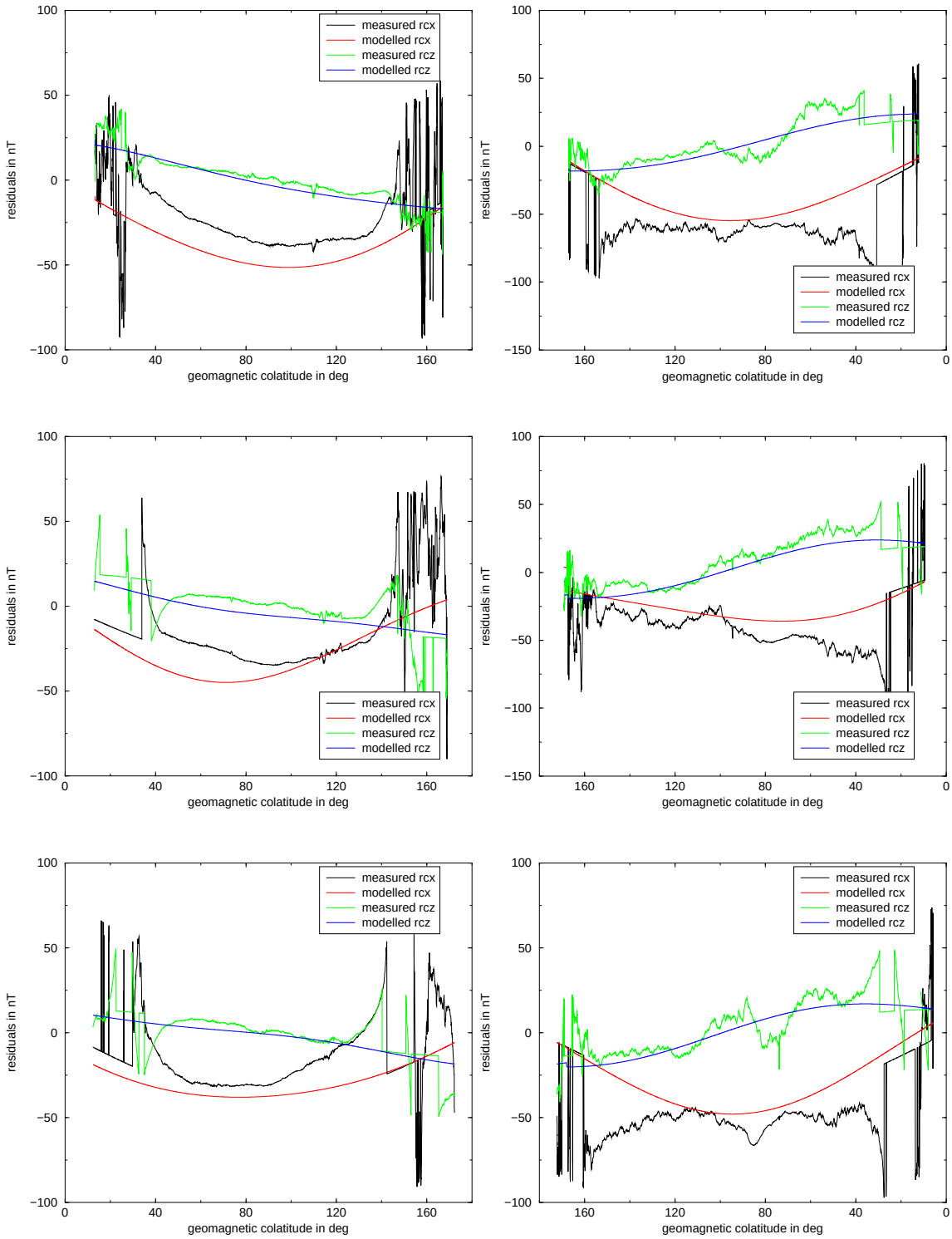

Figure A.9: One day of modelled orbits from **'model 2'** using full orbits. Plotted are the 9th to 11th orbits (first half-orbit in the left panel, starting at the North pole and second half-orbit in the right panel) on the chosen day September, 4, 2002.

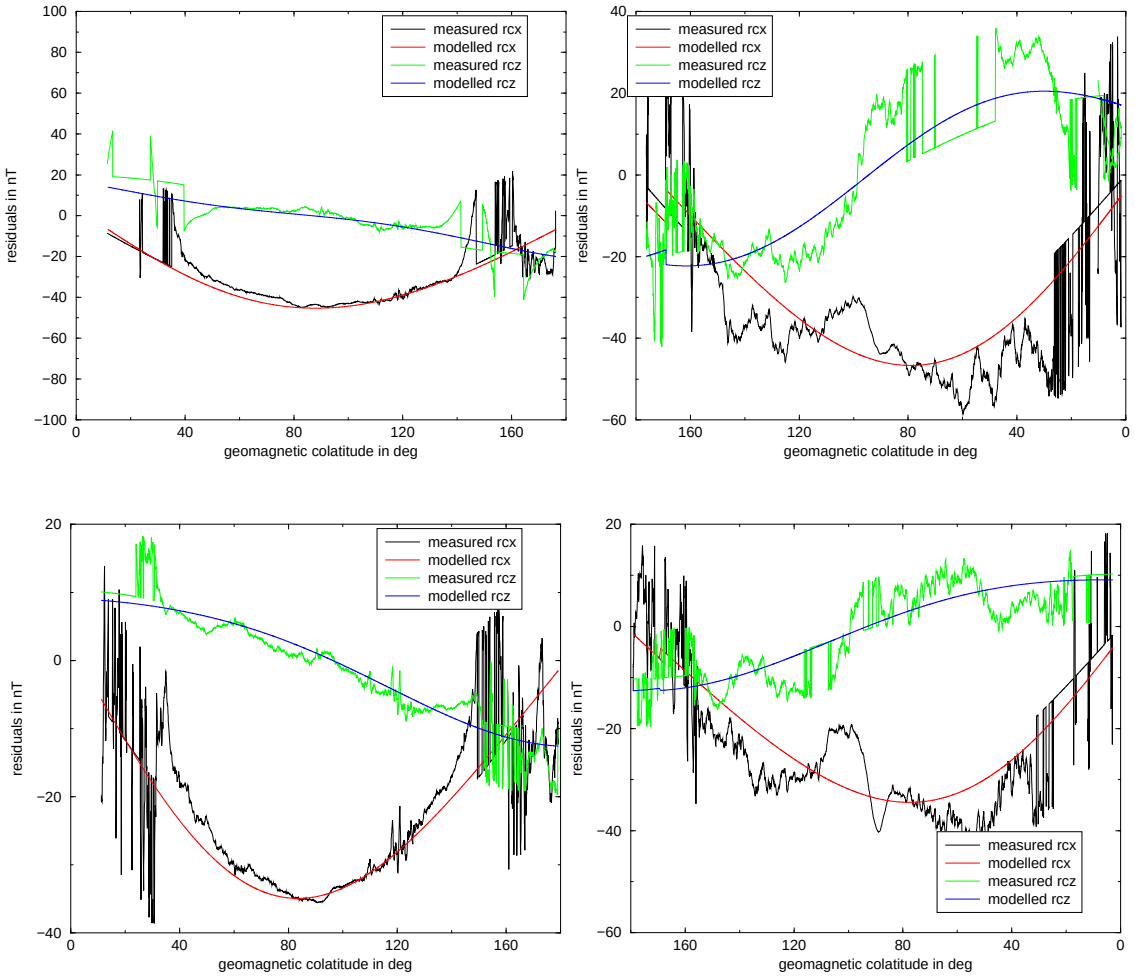

Figure A.10: One day of modelled orbits from **'model 2'** using full orbits. Plotted are the 12th to 13th orbits (first half-orbit in the left panel, starting at the North pole and second half-orbit in the right panel) on the chosen day September, 4, 2002.

Plot	**Longitude**	**Local time**
Fig. A.6, top, left	15.5°	3:26
Fig. A.6, top, right	-176.2°	15:25
Fig. A.6, bottom, left	-7.8°	3:26
Fig. A.6, bottom, right	160.6°	15:25
Fig. A.7, top, left	-31.0°	3:25
Fig. A.7, top, right	137.3°	15:25
Fig. A.7, middle, left	-54.3°	3:25
Fig. A.7, middle, right	114.1°	15:24
Fig. A.7, bottom, left	-77.5°	3:25
Fig. A.7, bottom, right	90.8°	15:24
Fig. A.8, top, left	-100.8°	3:24
Fig. A.8, top, right	67.6°	15:24
Fig. A.8, middle, left	-124.1°	3:24
Fig. A.8, middle, right	44.3°	15:23
Fig. A.8, bottom, left	-147.3°	3:24
Fig. A.8, bottom, right	21.0°	15:23
Fig. A.9, top, left	-170.6°	3:23
Fig. A.9, top, right	-2.2°	15:23
Fig. A.9, middle, left	166.2°	3:23
Fig. A.9, middle, right	-25.5°	15:22
Fig. A.9, bottom, left	142.9°	3:23
Fig. A.9, bottom, right	-48.7°	15:22
Fig. A.10, top, left	119.7°	3:23
Fig. A.10, top, right	-72.0°	15:22
Fig. A.10, bottom, left	96.4°	15:22
Fig. A.10, bottom, right	-95.3°	3:22

Table A.4: September, 4, 2002: Longitude and local time of the equator crossing for each orbit, corresponding to Figures A.6- A.10.

Appendix B

DST network

Observatory		geographic longitude (E)	geographic latitude	geomagnetic dipole latitude
Hermanus		19.22°	−34.40°	−33.3°
Kakioka		140.18°	36.23°	26.0°
Honolulu	to April 1960	201.90°	21.30°	21.0°
	after April 1960	201.98°	21.31°	21.0°
San Juan	to January 1965	293.88°	18.38°	29.9°

Table B.1: Coordinates of the four observatories, which build the network for D_{ST}.

From these observatories the D_{ST}-index is determined as defined in the IAGA Bulletin No. 40 [Berthelier & Menvielle, 1991]. The description how the D_{ST}-index is derived can be found on the webpage of the World Data Centre, Kyoto [WDC-Kyoto, 2003]. Here, only a short extract what D_{ST} is:
'The Dst index represents the axially symmetric disturbance magnetic field at the dipole equator on the Earth's surface. Major disturbances in Dst are negative, namely decreases in the geomagnetic field. These field decreases are produced mainly by the equatorial current system in the magnetosphere, usually referred to as the ring current. The neutral sheet current flowing across the magnetospheric tail makes a small contribution to the field decreases near the Earth. Positive variations in Dst are mostly caused by the compression of the magnetosphere from solar wind pressure increases. ...'

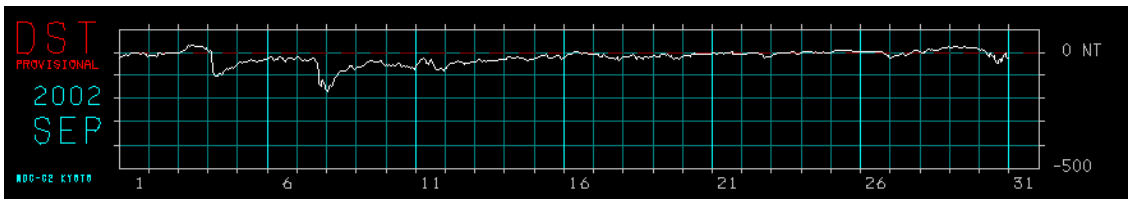

Figure B.1: Plot of D_{ST} values for September 2002, from [WDC-Kyoto, 2003].

Figure B.1 shows the plot of one month of D_{ST} values. In main field modelling mostly undisturbed data are necessary. Often only night side data are used and a data selection is done on D_{ST} (and other indices). In the CO2-main field model [Holme et al., 2003], e.g., requires D_{ST} within $\pm$10nT and $|d(D_{ST})/dt| < 3$nT/hr (and requires $K_p \leq 1+$ and $K_p \leq 2\circ$).

Appendix C

Institutes

- CNES - Centre National d'Etudes Spatiales:
  http://www.cnes.fr
- DMI - Danmarks Meteorologiske Institut:
  http://www.dmi.dk
  Ørsted: http://web.dmi.dk/projects/oersted
- DSRI - Danish Space Research Institute:
  http://www.dsri.dk
  swarm: http://www.dsri.dk/swarm
- DTU - Danmarks Tekniske Universitet:
  http://www.dtu.dk
- DLR - Deutsches Zentrum für Luft- und Raumfahrt:
  http://www.dlr.de
- GFZ - GeoForschungsZentrum Potsdam:
  http://www.gfz-potsdam.de
  CHAMP: http://www.gfz-potsdam.de/champ
  CHAMP data centre: http://isdc.gfz-potsdam.de/champ/
  Section 2.3: http://www.gfz-potsdam.de/pb2/pb23
- IAGA - International Association of Geomagnetism and Aeronomy:
  description of the International Geomagnetic Reference Field:

http://www.ngdc.noaa.gov/IAGA/wg8/igrf.html
coefficients of IGRF2000:
http://www.ngdc.noaa.gov/IAGA/wg8/table1.txt

- IPGP - Institute de Physique du Globe de Paris:
  http://www.jpgp.jussieu.fr

- LETI - Laboratoire d'Electronique de Technologie d'Information:
  http://www-leti.cea.fr

- NASA - National Aeronautics and Space Administration:
  http://www.nasa.gov
  GSFC - Goddard Space Flight Center: http://www.gsfc.nasa.gov
  SAC-C: http://www.gsfc.nasa.gov/gsfc/service/gallery/fact_sheets/spacesci/sac-c.htm
  JPL - Jet Propusion Laboratories: http://www.jpl.nasa.gov
  NSSDC - National Space Science Data Center: http://nssdc.gsfc.nasa.gov/space
  MAGSAT: http://nssdc.gsfc.nasa.gov/space/space_phys/nmagsat.html

- ONERA - Office National d'Etudes et de Recherches Aerospatials:
  http://www.onera.fr

- TU Braunschweig - Technische Universität Braunschweig:
  http://www.geophys.tu-bs.de

- The University of Liverpool:
  http.www.liv.ac.uk

- WDC Kyoto - World Data Center Kyoto:
  http://swdcdb.kugi.kyoto-u.ac.jp

THANK YOU!

I wish to thank Prof. Dr. V. Haak, the head of Section 2.3, for supporting this work. Thank you for your kind assistance.

My special thanks go to Prof. Dr. H. Lühr for initiating this thesis and providing me with an challenging research topic. Your continuous support and many fruitful discussions are highly acknowledged.

Many thanks to Dr. Richard Holme; for your inspiration, support and encouragement.

Dr. Mioara Mandea; thank you very much for the invaluable co-operation with you and your group at IPGP, and thanks for all your help. I really enjoyed the time together with you.

I also would like to thank Dr. Nils Olsen; for providing the RC* index and for the very helpful support with the coordinate transformation.

Many thanks to the whole group at GFZ for their constant help, cooperation, insightful discussions, good quality data, instrument operation, ... and superb cups of tea. They all have been a wonderful source of encouragement and the basis for this work.
Last but not least, I would like to thank Jörg, my family and a lot of friends who always kept me smiling.

This work was supported by the DFG special research program 1097.
The 5-month visit in Paris at IPGP was financed by the European Commission Research Directorates General Marie Curie Host Fellowships.